5.2 *Ageostrophic instabilities of fronts in a channel in a stratified rotating fluid*

Les résultats sur les instabilités agéostrophiques dans le modèle de Phillips et l'évolution non-linéaire de l'instabilité Rossby-Kelvin font l'objet d'un article publié dans *Journal of Fluid Mechanics* (Gula *et al.* (2009*a*)). Ainsi nous les incluons en anglais.

Ageostrophic instabilities of fronts in a channel in a stratified rotating fluid

J. Gula, R. Plougonven & V. Zeitlin [1]

(Received 4 February 2008 and in revised form 14 January 2009)

It is known that for finite Rossby numbers geostrophically balanced flows develop specific ageostrophic instabilities. We undertake a detailed study of the Rossby-Kelvin (RK) instability, previously studied by Sakai (1989) in a two-layer rotating shallow water model. First, we benchmark our method by reproducing the linear stability results obtained by Sakai (1989) and extend them to more general configurations. Second, in order to determine the relevance of RK instability in more realistic flows, simulations of the evolution of a front in a continuously stratified fluid are carried out. They confirm the presence of RK instability with characteristics comparable to those found in the 2-layer case. Finally, these simulations are used to study the nonlinear saturation of the RK modes. It is shown that saturation is achieved through the development of small-scale instabilities along the front which modify the mean flow so as to stabilise the RK mode. Remarkably, the developing instability leads to conversion of kinetic energy of the basic flow to potential energy, contrary to classical baroclinic instability.

5.2.1 Introduction

The study of instabilities of vertically sheared flows in rotating stratified fluids has provided understanding of important aspects of mid-latitude motions in the atmosphere and ocean, starting from the work of Eady (1949) on baroclinic instability. The latter has been identified as the major instability occurring for flows with small Rossby numbers. It is well described in balanced models such as the quasi-geostrophic model, and can be interpreted in terms of the resonant interaction between two Rossby waves (Hoskins *et al.* (1985); Hayashi & Young (1987)).

However, a vertically sheared flow in the stratified, rotating fluid displays other instabilities as well. These are not captured by balanced approximations and hence are *ageostrophic* instabilities. They have first been addressed for the uniform vertical shear in the stratified fluid by Stone (1966) who demonstrated appearance of symmetric instability. The Kelvin-Helmholtz instability also appears for not-uniform vertical shear profiles (Vanneste (1993), Drazin & Reid (1981)). For intermediate values of the shear, both Stone (1970) and Tokioka (1970) identified other ageostrophic instabilities, at scales shorter than those of conventional baroclinic instability. These modes however have weaker growth rates, and it was hence argued that they would not be relevant (Stone (1970)). Their structure involves inertial critical levels (Jones (1967)) in the flow, and the connection of balanced motions to inertia-gravity waves through that level (Nakamura (1988) ; Plougonven *et al.* (2005)). Corresponding growth rates are exponentially small for small Rossby numbers (Molemaker *et al.* (2005)), making them relevant only for significant vertical shears.

Baroclinic instability is traditionally explained with the help of the two-layer model (Phillips (1954)). The stability of the ageostrophic version of the Phillips' model was studied by Sakai (1989), who showed the existence of unstable modes involving the resonance between a Rossby wave in one layer and a Kelvin wave in the other. Hence the instability was called Rossby-Kelvin (RK). In contrast to the results of Stone (1970),

[1]LMD, Ecole Normale Supérieure,
24, rue Lhomond, 75231 Paris Cedex 05, France

the growth rates of this instability proved to be comparable to or even larger than those of the baroclinic instability.

Sakai carried out the linear stability analysis for the two-layer fluid in a symmetric configuration which is known to be degenerate (Pedlosky (1987), section 7.11), both layers having the same mean depth. Hence, several questions arise : *(1)* what are the manifestations of this instability in the more general case ? *(2)* Are the unstable modes and their growth rates specific to the two- layer configuration, or do they exist also in stratified fluid for sharp enough fronts ? *(3)* How do they nonlinearly saturate ?

The fundamental motivation for the present study is that RK instability provides an example of coupling between balanced and unbalanced motions. Most of the dynamics of the atmosphere and oceans in mid-latitudes has been understood using balanced models (e.g. Pedlosky (1987)). It has been thought that balanced motions could even decouple completely from unbalanced motions, leading to the notion of an exactly invariant *slow manifold* (Leith (1980); Lorenz (1980)). It is now understood that *slow manifolds* are quasi-manifolds (Ford *et al.* (2000)), e.g. quasi-geostrophy defines one, nonlinear balance(s) define a more accurate one(s). Yet the mechanisms by which balanced and unbalanced motions can couple and interact remain poorly understood. They have recently attracted renewed interest, both from theoretical (e.g. Plougonven & Zeitlin (2002); Vanneste & Yavneh (2004); Molemaker *et al.* (2005); Vanneste & Yavneh (2007)) and experimental points of view (Afanasyev (2003); Williams *et al.* (2005)), motivated by questions arising both for the atmosphere and for the ocean. In particular, in the laboratory experiments (Williams *et al.* (2005)), the stability of fronts has been studied to identify the coupling between balanced and unbalanced motions. The interpretation of such experiments would benefit from a better understanding of the stability properties of intense fronts in a stratified rotating fluid.

Regarding the atmosphere, understanding of the coupling of balanced and unbalanced motions can contribute to a better identification of sources of gravity waves and their parametrizations. Indeed, a serious weakness of parametrizations of gravity waves in General Circulation Models of the atmosphere (Fritts & Alexander (2003); Kim *et al.* (2003)) is their lack of physical description of the sources of gravity waves. A major source in midlatitudes are tropospheric jets and fronts (Fritts & Nastrom (1992); Plougonven *et al.* (2003)), which are essentially balanced. Another atmospheric application is understanding of the dynamics of secondary cyclogenesis in frontal systems. While the development and evolution of baroclinic waves on the synoptic scale is well understood in the atmosphere, the rapid growth of secondary cyclones at smaller-scales is poorly understood and difficult to forecast (Parker (1998)). Among the variety of mechanisms which contribute to small-scale cyclones, dynamic instabilities of a strong dry front are a possibility to investigate.

Regarding the ocean, an open issue is the mixing required to maintain the meridional overturning circulation. It is necessary that small-scale mixing in the interior of the oceans allows dense fluid to be raised toward the surface (Wunsch & Ferrari (2004)). At present, it remains unclear how energy may cascade in the ocean interior from the balanced meso-scale circulations to small-scale unbalanced motions that lead to the vertical mixing, e.g. Molemaker *et al.* (2005). Ageostrophic instabilities may provide a path to energy dissipation at small-scales and conversion of kinetic to potential energy.

The paper is organized as follows : in section 5.2.2 we present the linear stability analysis of the balanced front in the two-layer fluid in various configurations, in section 5.2.3 we study the stability of the sharp front in a continuously stratified fluid using the atmospheric mesoscale model WRF, and in section 5.2.4 the nonlinear evolution of the

Rossby-Kelvin mode is discussed.

5.2.2 Linear stability analysis in the two-layer fluid

We first present the model, its linearised version, and introduce the key parameters in section 5.2.2. We then display the instabilities, their growth rates and the structure of the unstable modes in section 5.2.2, and give a short summary of the results in section 5.2.2

Overview of the model and the method

We consider the two-layer rotating shallow water model on the f-plane with a vertical shear flow as shown in figure 3. The domain is a vertically bounded channel of width $2L_c$ and height $2\,H_0$. On the f-plane the momentum and continuity equations are :

$$\begin{aligned} D_j u_j - f v_j &= -\frac{1}{\rho_j}\partial_x \pi_j \ , \\ D_j v_j + f u_j &= -\frac{1}{\rho_j}\partial_y \pi_j \ , \\ D_j h_j + \nabla\cdot(h_j \mathbf{v_j}) &= 0 \ , \end{aligned} \tag{1}$$

where the index $j = 1, 2$ denotes the upper and the lower layers, respectively, (x, y) and $\mathbf{v_j} = (u_j, v_j)$ are the along-channel and cross-channel coordinates and velocity components, $h_j = H_j(y)+(-1)^j\eta(x, y, t)$ are the depths of the layers with η the interface displacement, π_j, ρ_j are the pressures and the densities of the layers, $D_j = \partial_t + u_j\partial_x + v_j\partial_y$ is the Lagrangian derivative, and f is the constant Coriolis parameter.

We linearise these equations about the steady geostrophically balanced state with the depth profiles $H_j(y)$, and corresponding velocities $U_j(y) = -(\rho_j f)^{-1}\partial_y\Pi_j$. The linearised equations, where u_j, v_j, π_j and η are the perturbations to the basic state fields, are :

$$\begin{aligned} \partial_t u_j + U_j\partial_x u_j + v_j\partial_y U_j - f v_j &= -\frac{1}{\rho_j}\partial_x\pi_j \ , \\ \partial_t v_j + U_j\partial_x v_j + f u_j &= -\frac{1}{\rho_j}\partial_y\pi_j \ , \\ \partial_t\eta + U_j\partial_x\eta &= (-1)^{j+1}(H_j\partial_x u_j + \partial_y(H_j v_j)) \ , \end{aligned} \tag{2}$$

The dynamical boundary condition at the interface between the 2 layers is :

$$\pi_2 - \pi_1 = (\rho_2 - \rho_1)g\eta \ , \tag{3}$$

where g is gravity acceleration.

In order to compare our results with those of the pioneering paper by Sakai (1989), the basic flow configuration and the non-dimensionalisation are chosen to be the same. We will consider the basic state with $U_1 = -U_2 = U_0$, and correspondingly linear $H_j(y)$. This is an ageostrophic version of the Phillips' model (Phillips (1954)) and both Rossby waves and inertia-gravity waves are present in this system.

We introduce the time scale $1/f$, the vertical scale $H_0 = H_2(0)$, the velocity scale U_0 and the pressure scale $\rho_i U_0 f R_d$. The Rossby deformation radius $R_d = (\frac{1}{2}g' H_0)^{\frac{1}{2}}/f$, with $g' = 2\Delta\rho g/(\rho_1 + \rho_2)$ the reduced gravity, will be used as the horizontal scale. We will use only non-dimensional variables from now on without changing the notation. The following non-dimensional equations are obtained in the limit of the Boussinesq approximation $((\rho_2 - \rho_1)/(\rho_2 + \rho_1) \to 0)$:

$$\begin{aligned} \partial_t u_j + F\,U_j\partial_x u_j - v_j &= -\partial_x\pi_j \ , \\ \partial_t v_j + F\,U_j\partial_x v_j + u_j &= -\partial_y\pi_j \ , \\ \partial_t\eta + F\,U_j\partial_x\eta &= (-1)^{j+1}(F(H_j\partial_x u_j + \partial_y(H_j v_j))) \ , \end{aligned} \tag{4}$$

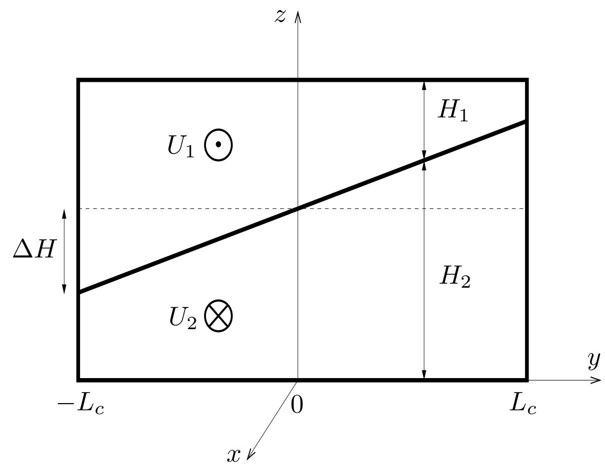

FIG. 3 – The basic balanced flow considered in the two-layer shallow water model for $\delta = H_1(0)/H_2(0) = 0.7$ and $\lambda = \Delta H/H_2(0) = 0.5$.

$$\pi_2 - \pi_1 = \frac{2}{F}\eta \,, \tag{5}$$

where $F = U_0/(fR_d)$ is the Froude number.

The boundary conditions are $v_j(\pm 1/(2\sqrt{Bu})) = 0$ at the lateral walls and the Burger number $Bu = (R_d/(2L_c))^2$ controls the width of the channel. The height field is then written $H_j = H_j(0) + (-1)^j Fy$.

Assuming a harmonic form of the solution in the x-direction,

$$(u_j(x,y), v_j(x,y), \pi_j(x,y)) = (\tilde{u}_j(y), \tilde{v}_j(y), \tilde{\pi}_j(y))\ exp\,[i(kx - \omega t)], \tag{6}$$

we obtain an eigenvalue problem of order 6 which can be solved by applying the spectral collocation method as described in Trefethen (2000) and Poulin & Flierl (2003). A complete basis of Chebyshev polynomials is used to obtain a discrete equivalent of the equations. This is achieved by evaluating (4) on a discrete set of N collocation points (typically $N = 50$ *to* 100). The eigenvalues and eigenvectors of the resulting operator are computed with Matlab routine "eig". The occurrence of spurious eigenvalues is common in such discretization procedure. We therefore checked the persistence of the obtained eigenvalues by recomputing the spectrum with increasing N.

Instabilities and growth rates

At this point we have three independent parameters which are the Froude number F, the Burger number Bu and the aspect ratio between the two layers δ. In order to explore parameter space using only one parameter for the flow, F, and the streamwise wavenumber k, Sakai (1989) restricted to a symmetric configuration, with $\delta = 1$, and chose to hold the relative elevation parameter $\lambda = F/(2\sqrt{Bu}) = 0.5$ constant, leading to $F = \sqrt{Bu}$. To facilitate the comparison with his results, we follow the same choice, but one should note the implication : as F varies, the width of the channel varies as λ/F. This unfortunately does not facilitate the comparison with laboratory experiments, such as those of Williams *et al.* (2005), where different non-dimensional parameters are chosen. Moreover, these experiments are carried out in a cylindrical annulus. To address these issues the corresponding linear stability analysis has been carried out in a companion paper (Gula *et al.* (2009*c*), submitted)

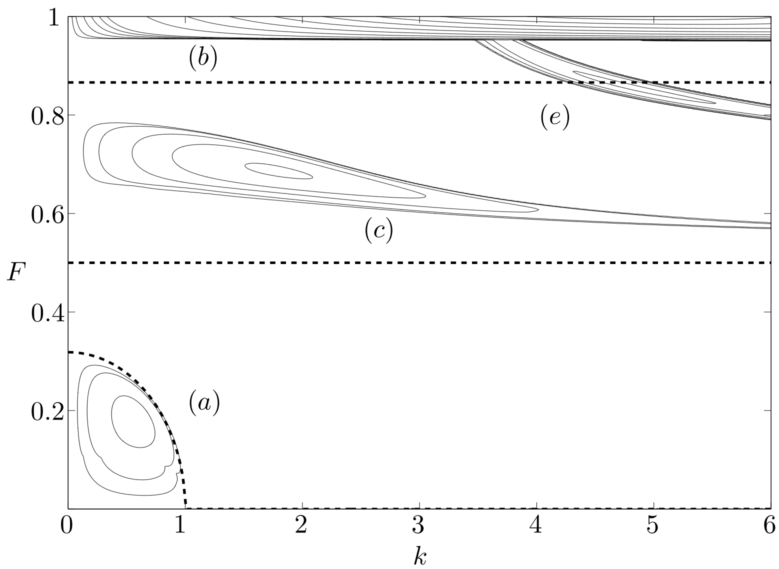

FIG. 4 – Growth rates of most unstable modes in (F, k)-space for $H_1(0) = H_2(0)$. Contours displayed are 0.01, 0.02, and further on at the interval 0.02. Dotted lines correspond to the limits of the instability zones (a) and (c) following from the frequency estimates and resonance conditions (see text).

The results of Sakai (1989) were reproduced, and the calculation in the symmetric configuration served as a benchmark of our method. The numerical results for the symmetric configuration are displayed in figure 4 and illustrate the different types of instabilities present in the symmetric configuration : (a) baroclinic instability for small F and k (the resonance between Rossby waves, see below), (b) Kelvin-Helmholtz instability for $F \approx 1$ (the resonance between Kelvin or inertia-gravity waves) and $(c), (e)$ Rossby-Kelvin instability for $F \approx 0.7$ (the resonance between a Rossby wave and a Kelvin or inertia-gravity wave, respectively).

Following Ripa (1983) and Sakai (1989) the flow with velocity U_0 is unstable if there exists a pair of waves (intrinsic frequencies $\tilde{\omega}_1$ and $\tilde{\omega}_2$) which satisfy the following conditions : the waves propagate in the opposite directions with respect to the basic flow ($\tilde{\omega}_1\tilde{\omega}_2 < 0$, meaning that they have opposite energy anomalies), have almost the same Doppler-shifted (absolute) frequencies ($\tilde{\omega}_1 + kU_0 \sim \tilde{\omega}_2 - kU_0$), and can interact with each other. The interpretation of the unstable modes as resonances between the neutral waves provides the explanation for the regions of parameter space corresponding to different instabilities. Thus, the classical baroclinic instability is interpreted as the interaction between two Rossby waves propagating in each layer, see Hoskins *et al.* (1985). The condition of matching of Doppler-shifted frequencies for two Rossby waves gives the standard condition for the baroclinic instability to occur : $k^2 + l_n^2 < 1/\sqrt{\lambda}$ (Pedlosky (1987), section 7.11) where l_n is the meridional wavenumber. Now, given the constraint linking the width of the domain and the Froude number, $F = \sqrt{Bu}$, l_n varies linearly with F and more precisely $l_0 = \pi/(2L_c) = \pi F/(2\delta)$. Hence the region of parameter space corresponding to baroclinic instability in figure 4 and 5 lies within the quadratic curve :

$$k^2 + \left(\frac{\pi F}{2\,\lambda}\right)^2 < \frac{1}{\sqrt{\delta}}. \tag{7}$$

The Rossby-Kelvin instability can also be understood in terms of Kelvin and Rossby wave resonances. It is then possible to obtain stability conditions in the approximation of large k using heuristic arguments for the resonance between the Kelvin and the Rossby wave. We estimate the absolute frequency for the Rossby wave as $\omega_R \simeq k\,F$ because the intrinsic frequency of Rossby waves is small for large k. The intrinsic frequency for the Kelvin wave in a layer of constant depth H can be written as $\tilde{\omega}_K = k\sqrt{g'H}$. Now, in our configuration the depth of each layer $H_j(y) = H_j(0) + F\,y$ is a function of y. Using the extreme values of the depth of one layer gives bounds on the possible intrinsic frequencies of Kelvin waves in this layer : $\sqrt{2}k\sqrt{\delta \pm \lambda}$. Hence, it is most likely for a Rossby wave in one layer to interact with a Kelvin wave in the other layer, if we have :

$$\sqrt{2}k\sqrt{H_j(0) - \lambda} < 2kF < \sqrt{2}k\sqrt{H_j(0) + \lambda},$$

with j the index of the layer containing the Kelvin wave. So if the Kelvin wave is in the upper layer and the Rossby wave in the lower layer we get :

$$\sqrt{\frac{\delta - \lambda}{2}} < F < \sqrt{\frac{\delta + \lambda}{2}} \tag{8}$$

and and for the Kelvin wave in the lower layer and the Rossby wave in the upper layer :

$$\sqrt{\frac{1 - \lambda}{2}} < F < \sqrt{\frac{1 + \lambda}{2}} \tag{9}$$

In the symmetric configuration of figure 4 ($\lambda = 0.5$ and $\delta = 1$) this gives $0.5 < F < 0.85$ for both (cf. figure 4). This suggests that in this configuration and at least for large k there is a range of Froude numbers ($1/\pi^2 < F < 1/2$ in figure 4) where no instability can occur. Although this condition has been obtained only for large k, it can be seen in figure 4 and it has been confirmed by numerical calculations that this stability area exists for all k. Increasing λ or changing the aspect ratio δ can modify this gap as can be seen in figure 5 for a non-symmetric configuration ($\delta = 0.7$).

The configuration with the layers of the same mean depth is degenerate (Pedlosky (1987), section 7.11). For example, the interaction between a Rossby wave in the lower layer and a Kelvin or inertia-gravity wave in the upper layer have the same characteristics (wavenumbers and growth rates) as the interaction between a Kelvin or inertia-gravity wave in the lower layer and a Rossby wave in the upper layer. Below we present an example of the results of the stability analysis for a non-symmetric configuration, for which the depths of the two layers are not equal : $\delta = 0.7$ (this is the configuration sketched in Fig. 3). Figure 5 shows the growth rates in the (F, k) plane for different types of instabilities. At the lower-left, for small F and k, one finds the baroclinic instability (a). For very strong shears, $F \approx 1$, Kelvin-Helmholtz instability occurs (b), with larger growth rates ($\omega_i \sim 1$). For intermediate values of the Rossby number, one finds two regions of instability ($F \approx 0.5$ for (c) and $F \approx 0.7$ for (d)) which correspond to Rossby-Kelvin instability. These instabilities exist due to the interaction of a Rossby wave in one layer and a Kelvin wave in the other. However, contrary to the symmetric case, cf figure 4, two different Rossby-Kelvin instabilities occur, instead of a single one.

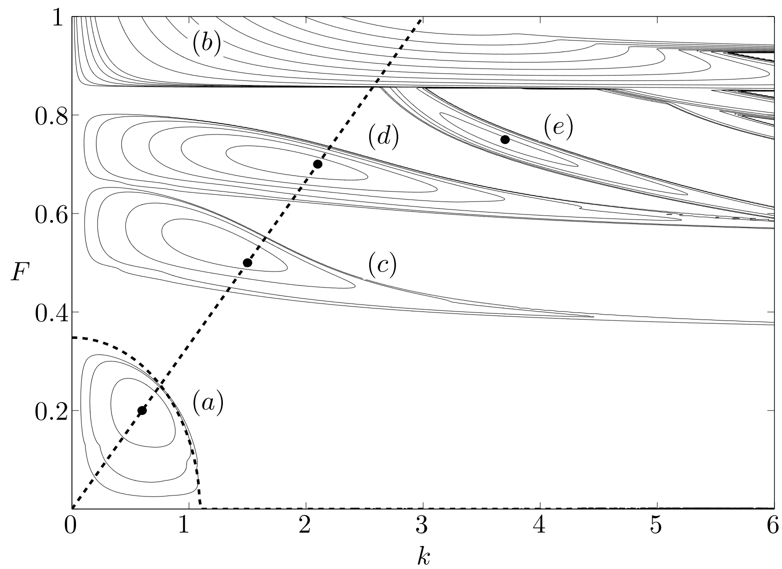

FIG. 5 – Growth rate of most unstable modes in (F, k)-space for $\delta = 0.7$. Contours displayed are 0.01, 0.02 and further interval 0.02. (a) is the baroclinic instability, (b) the Kelvin-Helmholtz instability and (c, d, e) the Rossby-Kelvin instability.

Figure 6 shows the phase velocities and the growth rates along the section $F = k/3$ following the dotted line in figure 5. Baroclinic instability (a) occurs for small k and Kelvin-Helmholtz instability (b) for k greater than 2.6. The two other peaks (c) and (d), for intermediate values of k are the two types of Rossby-Kelvin instability, with different growth rates. The dispersion diagram of figure 6 (upper panel) shows that the instability occurs once two dispersion curves intersect, according to the Doppler-shifted frequency matching described above. The dispersion curves shown in figure 6 differ from those of the symmetric case : whereas the Rossby wave phase speeds remain nearly symmetric relative to $c = 0$, the phase speeds for the Kelvin waves are displaced toward higher values. Hence, the intersection between the two modes moves toward higher k for positive phase speeds. We thus get two distinct instability areas. One corresponds to modes having a Kelvin wave in the upper layer and a Rossby wave in the lower layer. The structure of such a mode is shown in the left panel of the figure 7. The other corresponds to modes having a Kelvin wave in the lower layer and a Rossby wave in the upper layer (right panel of the figure 7). The characteristic velocities and pressure fields of the Rossby wave are easily recognizable with geostrophic wind turning around pressure extrema according to the geostrophic balance. The structure of the Kelvin waves with the wind parallel to the boundaries and pressure extrema near the lateral boundary is also clear and points out the ageostrophic character of this wave.

The instability area (e) in figure 5 is still a type of Rossby-Kelvin instability arising due to the resonance between a Rossby wave and an inertia-gravity wave (first Poincaré mode) as can be seen in figure 6. The Rossby wave propagating in the lower layer interacts with the first Poincarré mode in the upper layer as shown in figure 8. A simple criterion for this Rossby-Kelvin instability to occur as a result of resonance between a Rossby wave and a Poincarré wave can be found in Sutyrin (2007).

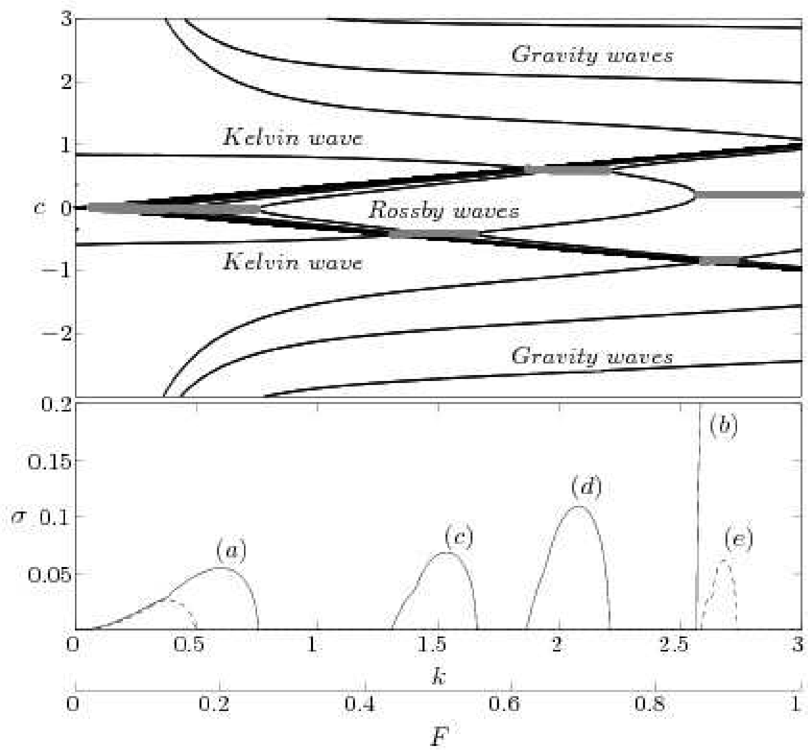

FIG. 6 – Dispersion diagram (upper panel) and growth rates (lower panel) of the eigenmodes along the section $F = k/3$ (dotted line in figure 5). Gray zones on the upper panel correspond to the instabilities : (a) the baroclinic instability, (b) the Kelvin-Helmholtz instability and (c, d, e) the Rossby-Kelvin instability

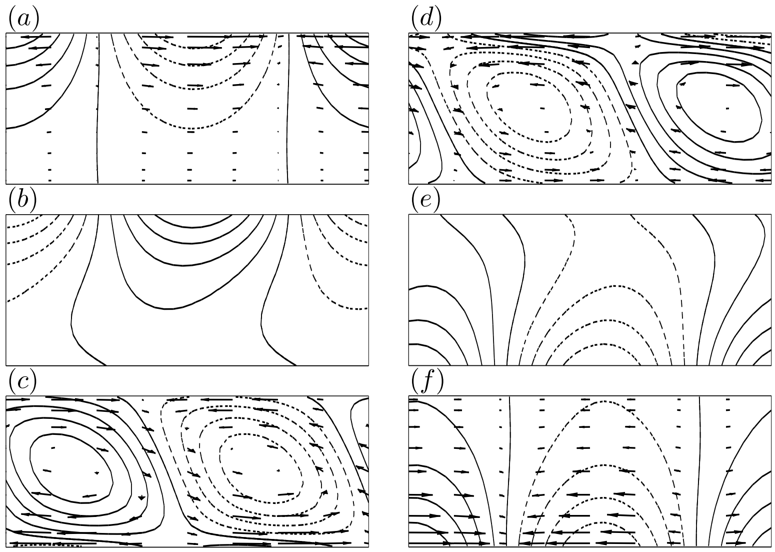

FIG. 7 – The structure of the Rossby-Kelvin mode in (x, y) at the maximum growth rate for $\delta = 0.7$. (a), (b) and (c) correspond to the second maximum of figure 6 for $F = 0.5$; (d), (e) and (f) correspond to the third maximum of figure 6 for $F = 0.7$. (a) and (d) are pressure and velocity fields of the upper layer, (c) and (f) are those of the lower layer. Interface height is shown in (b) and (e). The fields in (a) and (f) are typical of a Kelvin mode and (c) and (d) are typical of a Rossby mode. The full lines correspond to positive and the dotted lines to negative values.

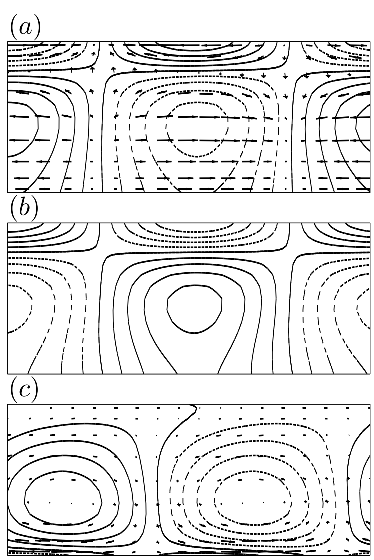

FIG. 8 – The structure of another ageostrophic mode in (x, y) due to the resonance between Rossby and inertia-gravity modes at the maximum growth rate for $F = 0.75$ and $k = 3.7$ on figure 6; (a) : pressure and velocity fields in the upper layer and (c) lower layer. (b) : Interface height.

Summary of the linear instability analysis

We thus benchmarked our method by reproducing the linear stability results obtained by Sakai (1989) and extended them to non-symmetric configurations where two different families of unstable Rossby-Kelvin (RK) modes exist : one with the Kelvin wave in the top layer, the other with the Kelvin wave in the bottom layer. When the two layers have sufficiently different depths, the two regions separate, and hence a larger region of the parameter space yields instabilities (cf. Fig. 5). We have also shown that a zone of (relatively high) Froude numbers may exist, where neither baroclinic nor Rossby-Kelvin instability is present, and hence the flow is stable. The unstable RK-modes are significant because of their large growth rates. This is in contrast with ageostrophic unstable modes found in flows with constant shear (Molemaker *et al.* (2005); Plougonven *et al.* (2005)). However, as RK modes have been exhibited only in the two-layer rotating shallow water model, it is necessary to confirm that they also exist in a continuously stratified fluid.

5.2.3 RK instability in the continuously stratified fluid

We investigate below the instability of a front in a periodic channel by direct numerical simulations using the Weather Research and Forecast Model (Skamarock *et al.* (2005)). This model has been developed to allow both operational and idealized simulations of fully compressible, nonhydrostatic atmospheric flows. The equations of motion are integrated in time using a 3rd order time-split Runge-Kutta scheme, and variables are discretized in space on a staggered Arakawa C-grid (Wicker & Skamarock (2002)).

The model was chosen for its capacity to simulate flows of increasing complexity and realism, up to real-case studies. In previous investigations of the spontaneous generation of inertia-gravity waves from idealized baroclinic life cycles (Plougonven & Snyder (2005, 2007)), the model has proved robust and able to provide a neat description of the weak emission of inertia-gravity waves by atmospheric jets and fronts.

First, we will present the model and the experimental setup of the simulations (section 5.2.3). Second, the most unstable modes for different sets of (F, k) parameters are described (section 5.2.3). Finally the robustness of the RK modes with respect to changes of the basic flow and/or model parameters is investigated (section 5.2.3). We will see that the front thickness and the background stratification has an effect on the growth rates even if the dynamics remain essentially the same.

The model and the experimental setup

The domain is a channel of size (L_x, L_y, L_z) in the f-plane, periodic in x and bounded by lateral walls in y with a free slip boundary condition. The free slip boundary condition is imposed at the flat bottom as in the 2-layer model of the previous section, and the top boundary is a free surface at constant pressure. Three main differences with the 2-layer model are (1) the background stratification (in addition to the front), (2) compressibility and its associated exponential decay of density in the vertical, and (3) the top boundary condition (free surface and not a rigid lid). These differences are not insignificant, but should not affect the physical mechanisms providing the RK instability : if the unstable modes are robust, they will manifest themselves, though with possible differences in the structure of velocity and pressure fields and in growth rates.

The basic state is defined by the strong localised gradient of potential temperature across the front :

$$\theta_{tot}(y,z) = \theta_0 + \Theta_z z + \tfrac{\theta_1}{2}\left(1 + \tanh\left(\tfrac{z - Z(y)}{D}\right)\right), \quad Z(y) = z_0 + S\,y, \tag{10}$$

where z_0 is the average height of the front, S the slope, θ_1 the potential temperature jump, D the thickness of the frontal zone, and $\Theta_z = const$ describes the basic stratification.

We obtain the balanced zonal jet configuration by assuming the thermal wind balance. As we consider a purely zonal flow, the thermal wind balance is an exact stationary solution of the full equations. Yet as described in Plougonven & Snyder (2007), the initial jet undergoes a minor adjustment when injected in WRF. Hence, to eliminate this adjustment the fields are averaged over two inertial periods, and the process is repeated twice, so that the adjustment associated to the background jet is negligible.

All variables in the WRF model are dimensional. Hence, it is necessary to choose a physical scale for the domain. We chose to work with typical tropospheric values of parameters : a domain height $L_z = 2\,H_0 = 10\,km$ with a standard stratification $\Theta_z = \Theta_0/gN^2 = 2.9\,10^{-3}\,Km^{-1}$ corresponding to a buoyancy frequency of $N^2 = 10^{-4}\,s^{-2}$, a potential temperature $\theta_0 = 280\,K$ at the ground, a $\theta_1 = 10\,K$ potential temperature jump along the front and a $D = 500\,m$ thickness for the frontal zone. At this point the horizontal scale of the domain and the slope of the front (or the wind speed) have not been set. They are determined by the choice of the two non-dimensional numbers $F = U_0/(fR_d)$ and k, respectively the Froude number and the wavenumber.

The Rossby deformation radius is given by :

$$R_d = \left(\frac{\frac{1}{2}g' H_0}{f^2}\right)^{\frac{1}{2}} = \left(\frac{g\theta_1 H_0}{2\theta_0 f^2}\right)^{\frac{1}{2}}, \tag{11}$$

and the Froude number is :

$$F = \frac{U_0}{\sqrt{g' H_0/2}}. \tag{12}$$

We then describe the flow in the (F,k)-space analogously to the previous section using the same relation between the channel width L_y and F as in Sakai (1989).

$$L_x = \frac{2\pi R_d}{k}, \; L_y = 2\Delta H \frac{R_d}{F} \tag{13}$$

From now on, the simulations are discussed only in terms of non-dimensional quantities using the scalings θ_1 for the potential temperature deviation $\theta = \theta_{tot} - \theta_{mean}$, $2\,H_0$ for z, R_d for x and y, and U_0 for all velocities. The initial state is shown in figure 9 for $F = 0.8$. Note that for simplicity we return here to a configuration with the two layers having equal mean depths, as in Sakai (1989). Yet because of compressibility and the top boundary condition, the 2 layers are no longer equivalent.

Our purpose is to determine whether Rossby-Kelvin modes are present and robust for a balanced front in the continuously stratified fluid. Hence, simulations are initialized with a slightly perturbed front and carried out for various values of F and k in order to identify the unstable modes along the line $F = k/3$. A breeding procedure is applied in order to isolate the most unstable normal mode, if any, for each set of parameters used. The most unstable mode is computed by following the evolution of a small perturbation

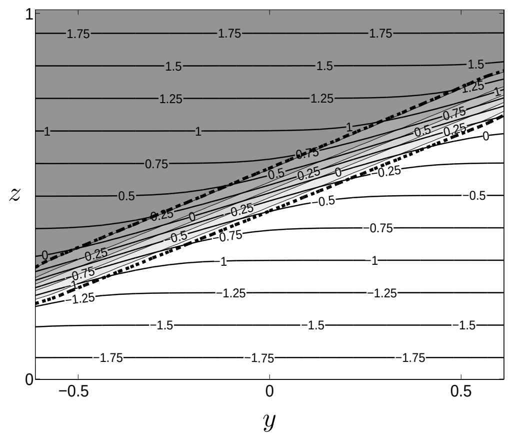

FIG. 9 – Initial distribution of potential temperature deviation θ (solid lines) and corresponding geostrophically balanced zonal wind (gray-white areas) for (z, y). The contour intervals are 0.25 for the potential temperature and 0.5 for zonal wind speed. The dashed lines indicate zonal velocities $U = 0.25$ and $U = 1.9$ i.e. localization of the front zone.

of the jet, then rescaling the perturbation to a smaller amplitude and starting the cycle again. The normal mode is then extracted, rescaled and superimposed upon the zonal jet. The simulations typically use 60 points for x and 40 for y with 80 levels in the vertical. We will then vary the number of points and keep the grid-length constant in order to sweep the (F, k) space.

Unstable modes

Baroclinic instability For large enough domains ($F < 0.3$ and $k < 1$) the classical baroclinic instability occurs. Pressure and velocity fields correspond to Rossby waves in the lower and the upper part of the front. The spatial structure of the modes is very close to those found in the 2-layer model (not shown). Growth rates are also very close to those of the 2-layer model, as can be seen in figure 12 for $F < 0.3$. It is worth reminding that, as is well known (see e.g. Holton (1992)) the classical baroclinic instability leads to a conversion of available potential energy to kinetic energy.

Rossby-Kelvin Modes The first key question is to determine whether the Rossby-Kelvin instability is also present in the continuously stratified case. The WRF simulations, as shown below, confirm the existence of these modes in the continuously stratified case, for values of F and k similar to those found in the 2-layer model.

The Rossby-Kelvin modes of instability are indeed present in the stratified fluid, and their structure is comparable to that found in the 2-layer model. Figure 10 shows the corresponding pressure and velocity fields vertically averaged below ($\theta < -0.5$) and above ($\theta > 0.5$) the frontal zone. The structure of the geostrophically balanced Rossby wave can be identified clearly below the front, and the structure of the Kelvin wave (wind parallel to the boundaries, pressure extrema at the lateral boundaries) can be identified above the front. In the horizontal plane, the signature of this mode is very

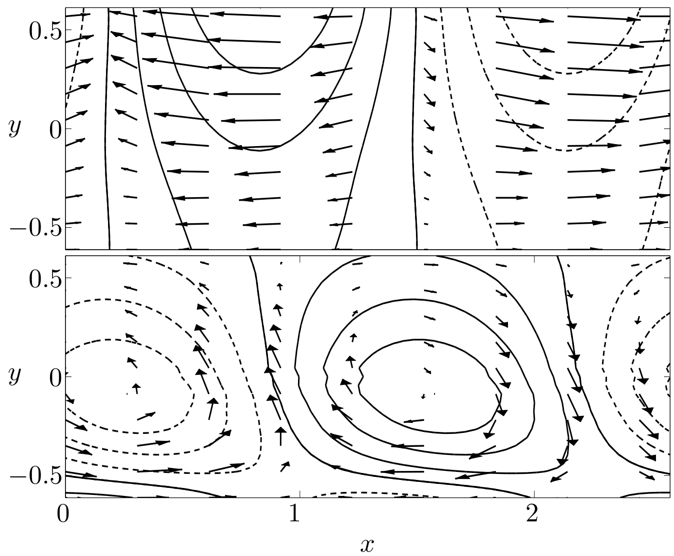

FIG. 10 – Vertically averaged pressure and velocity fields for the Rossby-Kelvin instability (a) above the front $(\theta > 0.5)$, and (b) below the front $(\theta < -0.5)$ for non-dimensional parameters $F = 0.8$ and $k = 2.4$. The full lines and the dotted lines indicate positive and negative values, respectively.

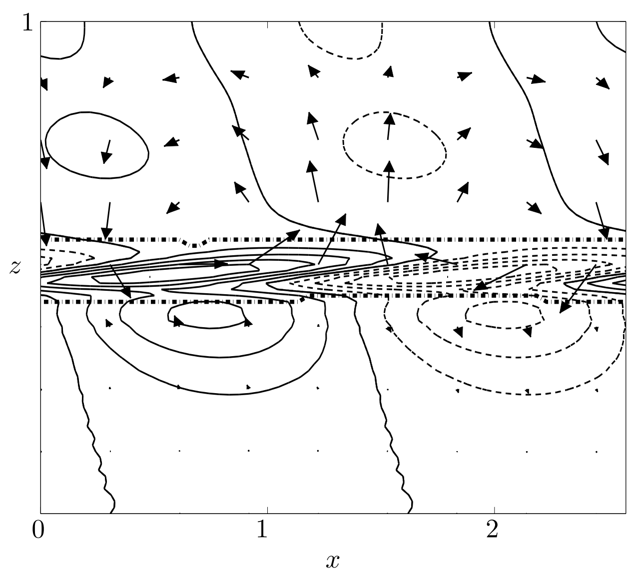

FIG. 11 – Velocity fields for the Rossby-Kelvin instability in the $y = 0$ plane for non-dimensional parameters $F = 0.8$ and $k = 2.4$. Contours correspond to the meridional velocity with contour intervals 0.009. The dash-dotted lines indicates the interval where the zonal velocity is between $U = 0.25$ and $U = 1.9$ i.e. localization of the front zone. Note the relatively strong vertical motion in the upper layer, indicating strong divergence of horizontal wind, and hence unbalanced motions.

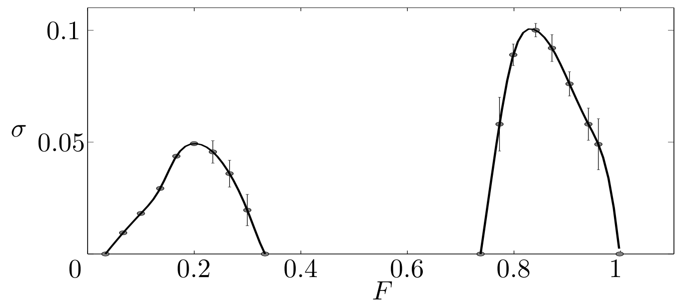

FIG. 12 – Growth rates of the instabilities of the front in the continuously stratified fluid. The peak at low k corresponds to the standard baroclinic instability. The peak for larger k corresponds to the Rossby-Kelvin instability.

close to its counterpart in the 2-layer model.

Figure 11 shows the velocity fields in the (x, z) plane at $y = 0$. Two features should be emphasized : firstly, the modes clearly couple motions of very different nature, i.e. balanced motions in the lower layer that are essentially non-divergent, and unbalanced motions in the upper layer that have significant signatures in the vertical velocity, and hence in the divergence of the horizontal wind. Secondly, the signature of the mode is concentrated near the front. In other words, although the horizontal structure of the mode when averaged over each layer (fig. 10) is very close to that found in the 2-layer model, the motions are not at all homogeneous in the vertical in each layer.

Growth Rates The growth rates are evaluated from the growth of kinetic energy of the perturbation over the whole domain. Figure 12 shows the corresponding non-dimensional growth rates comparable to those found for the 2-layer model (cf Sakai (1989), figure 7). The maximum growth rate of the instability attained for $k = 2.5$ is about $\sigma = 0.09$ scaled by f^{-1}, so $\sigma^{-1} = 1.25$ days.

Sensitivity of the results

Below we describe how the Rossby-Kelvin instability is influenced by the choice of the thickness of the frontal zone, by the value for the background stratification, and finally, by the resolution.

Stratification To see whether the RK modes and their growth rates are sensitive to the background stratification, simulations have been carried out for cases with no stratification, with half stratification and with double stratification, relative to the reference stratification described above

Changing the basic stratification Θ_z in the initial potential temperature distribution, cf. (10) from $\Theta_z = 0$ to $\Theta_z = 1.45$, $\Theta_z = 2.9$ and $\Theta_z = 5.8$ modifies the growth rates, as can be seen from the figure 13. The maximum growth rate becomes smaller as the stratification parameter becomes lower and the Rossby-Kelvin instability shifts to a smaller k. With a stratification weaker than in the reference simulation we were also able to find a Rossby-Kelvin mode consisting of a Kelvin wave below the front and a Rossby wave above for greater k. Corresponding pressure and velocity fields averaged above and below the front are shown in figure 14. However, these modes are less robust and seem to disappear as the background stratification increases.

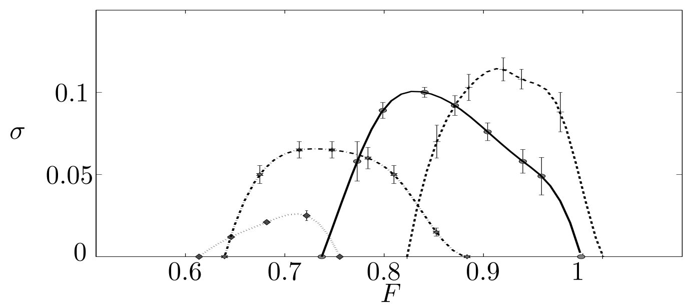

FIG. 13 – Growth rates for the RK mode of figure 10 for different basic stratifications. The dotted line corresponds to $\Theta_z = 0$, the dash-dotted line to $\Theta_z = 1.45$, the solid line to $\Theta_z = 2.9$ and the dashed line to $\Theta_z = 5.8$

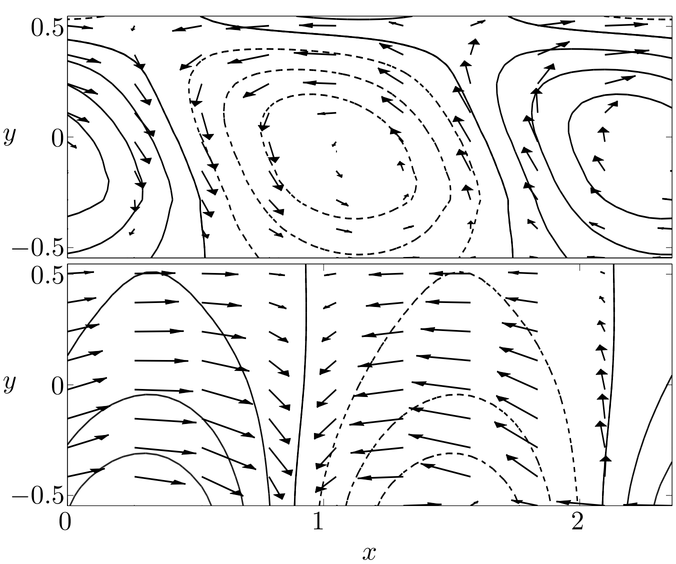

FIG. 14 – Pressure and velocity field for a Rossby-Kelvin instability vertically averaged (a) above the front ($\theta > 0.5$) and (b) below the front ($\theta < -0.5$) for a simulation with half stratification and non-dimensional parameters $F = 0.87$ and $k = 2.6$.

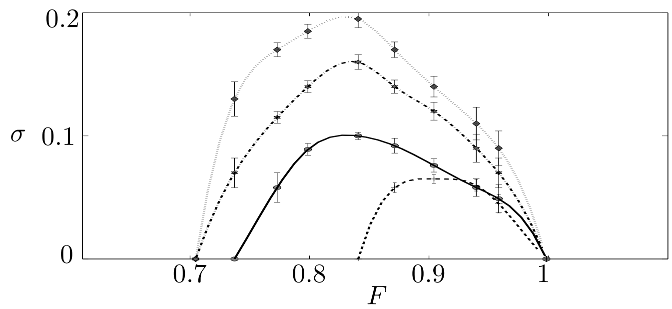

FIG. 15 – Growth rates for the RK mode of figure 10 for different thicknesses of the frontal zone. D is respectively 0.03 (dotted line), 0.04 (dash-dotted line), 0.05 (solid line) and 0.06 (dashed line) .

Front thickness In going from the 2-layer fluid to a continuously stratified fluid with two well-defined layers, the thickness of the transition between the two layers, i.e. of the front, is a free parameter. It is essential to verify the sensitivity of the Rossby-Kelvin modes to the sharpness of the front.

For the reference simulations described in section 5.2.3, a value of $D = 0.05$ was chosen for the front thickness (10). Simulations were also run for values of D ranging from 0.03 to 0.06, in the interval of F and k likely to reveal the Rossby-Kelvin instability. The simulations show that the RK modes are indeed quite sensitive to the thickness of the front, as can be seen from the growth rates plotted in figure 15. The growth rates increase significantly (up to a factor 2) as the front becomes sharper, and decrease for more diffuse fronts. Moreover, the range of wavenumbers k yielding instability is reduced for more diffuse fronts. Simulations were also carried out for front thicknesses $D \geq 0.16$, but did not exhibit robustly the presence of RK modes, or the growth of any other unstable ageostrophic modes.

Resolution As in any numerical study, the sensitivity of the results to resolution needs to be checked. By definition, the initial front has regions of sharp vertical and horizontal gradients (figure 9). Sharp gradients concentrated in the vicinity of the front are also found in the structure of the unstable modes (figure 11). Hence it is essential to verify how sensitive the above results are to the resolution.

The simulations described above typically had a resolution of 60 points in x, 30 points in y and 80 points in z. Simulations have been run with a resolution doubled relative to the reference run, and it was found that the linear stability results were unchanged : the RK modes grew having the same structure and the same growth rate. As an example, figure 16 shows the variation of kinetic energy with time for two simulations with $F = 0.8$ and $k = 2.4$, the first with a domain having 60 points in x, 30 points in y and 80 points in z, the second with twice as many points in all directions. During the linear stage, the two curves overlap, indicating that the growth rate is not sensitive to the resolution. The structure of the Rossby-Kelvin mode as described in figures 10 and 11 is also the same in both simulations. Hence, the results described above are robust and not sensitive to the resolution.

5.2.4 Non-linear evolution of the Rossby-Kevin instability

Previous studies of ageostrophic unstable modes of fronts have addressed the linear stability problem (Sakai (1989); Iga (1993)). To understand the importance that such ageostrophic modes may have in practice, it is necessary to investigate their nonlinear development and in particular to answer two questions : do they grow to significant amplitudes and how do they saturate ? The simulations carried out with WRF have the advantage of providing the answers to both questions. Below we will focus on two simulations with parameters $F = 0.8$ and $k = 2.4$: the reference run (as described in the previous section) and the corresponding run with double resolution.

First, the overall signature of the instability in the energy budget is discussed (section 5.2.4). Second, the features of the flow that appear at the saturation of the RK modes are described (section 5.2.4). These are found to be small-scale structures localized near one of the boundaries. Finally, the nonlinear effects due to the small-scale processes and their influence on the background mean flow is displayed (section 5.2.4), allowing for interpretation of the saturation of the RK modes.

Saturation and energetics

We first discuss the growth of the RK instability looking at the kinetic energy of the perturbation and then investigate the signature of the RK instability on the energetics of the total flow. We define the kinetic energy of the perturbation as :

$$K_{per} = \iiint \tfrac{1}{2}\rho(u'^2 + v'^2 + w'^2)dx\, dy\, dz\ , \tag{14}$$

where $u' = u - \langle u \rangle = u - \frac{1}{L_x}\int_0^{L_x} u dx$. Energies are calculated dimensionally then scaled by the kinetic energy of the basic flow. In both runs the instability grows exponentially up to $t \sim 40$, then saturates, as can be seen in figure 16. It can be verified that the zonal wavenumber 1 mode (figure 10) is by far the most energetic.

To discuss the energy budget of the instability we define :

$$\begin{aligned} K &= \iiint \tfrac{1}{2}\rho(u^2 + v^2 + w^2)dx\, dy\, dz\ , \\ P &= \iiint \rho(gz + c_v T)dx\, dy\, dz\ , \end{aligned} \tag{15}$$

where K is the total kinetic energy of the flow and P is the total potential energy obtained as the sum of the gravitational potential energy and the internal energy (see Holton (1992), section 8.3). The total energy conservation is then written :

$$\frac{d}{dt}[K + P] = 0 \tag{16}$$

In practice, we do not expect that the total energy will be exactly conserved in the simulations because of numerical dissipation. The deviations of potential and kinetic energies from their initial values are shown in figure 17 for RK instability (right) and, for reference, for baroclinic instability (left). While plotting the energy we used the reference simulation (figures 10 and 11), but the energetics of the double resolution simulation described in section 5.2.3 shows a very similar behaviour.

In sharp contrast with the classical baroclinic instability (see Holton (1992)), the RK modes are found to convert kinetic energy of the basic flow into potential energy. However, one must also note that the variations of energy due to the classical baroclinic

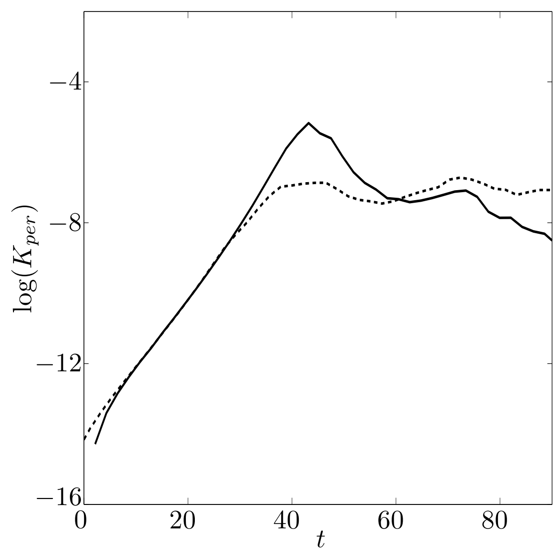

FIG. 16 – Logarithm of the kinetic energy K_{per} of the perturbation for the Rossby-Kelvin instability (normalized by initial total kinetic energy) for mode 1 in x, as a function of time. The dashed line shows the energy evolution for the simulation with double resolution as described in section 5.2.3

instability are stronger by a factor of 25. Hence RK instability has an effect on the basic flow which is opposite to that of baroclinic instability (conversion of kinetic to potential energy) but the energies exchanged are much smaller.

Finally, one can note in figure 17 that the sum of potential and kinetic energy is not exactly conserved for both simulations. For the case of baroclinic instability the energy loss because of numerical dissipation represents about 15% of the exchanged energies. For RK instability, it represents 60%. The difference is likely due to the effective generation of the small-scale motions involved in the saturation of the instability, as discussed below.

Small-scale instabilities

Inspection of the simulations shows that the saturation of Rossby-Kelvin instability involves intense small-scale motions, developing near the lateral boundary to which the Kelvin wave is attached. The highest resolution simulation as described in section 5.2.3 is used to resolve this small-scale dynamics as well as possible. Figure 18 shows the relative vorticity of the flow at the time when the amplitude of the perturbation is maximal ($t = 40$). In addition to the zonal wavenumber 1 signature of the RK mode, intense small-scale features are found near the northern boundary where the Kelvin wave propagates. The small-scale features appear to be the result of the Kelvin-Helmholtz type shear instabilities. They are particularly intense in the frontal region and generate quite intense vertical velocities above and below (not shown).

It is not surprising that the development of the RK modes leads to small-scale shear instabilities in the region of the front. Because the instability robustly appears only for sharp enough fronts (cf. section 5.2.3), the front in the basic state is already associated with low Richardson numbers, $Ri = N^2/(du/dz)^2 < 0.5$. Any motion will a priori

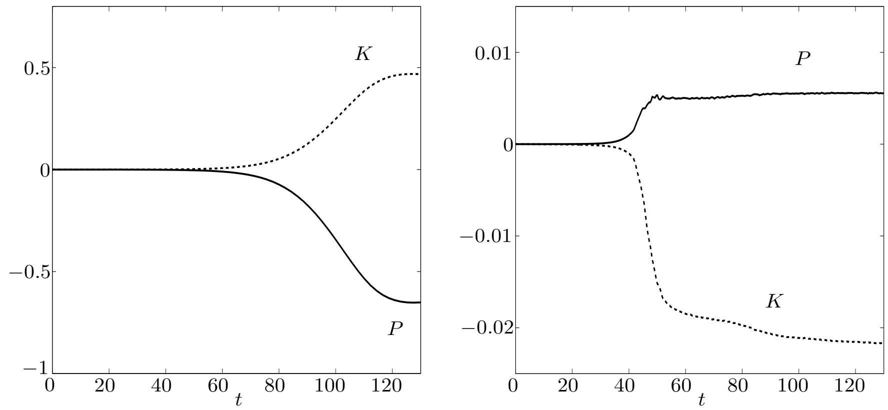

FIG. 17 – Deviations of the total potential (solid) and kinetic energy (dashed) of the flow during the growth stage of the baroclinic instability ($F = 0.2$, $k = 0.6$) (left) and of the Rossby-Kelvin instability ($F = 0.8$, $k = 2.4$) (right). Both energies are normalized by the initial total kinetic energy of the flow.

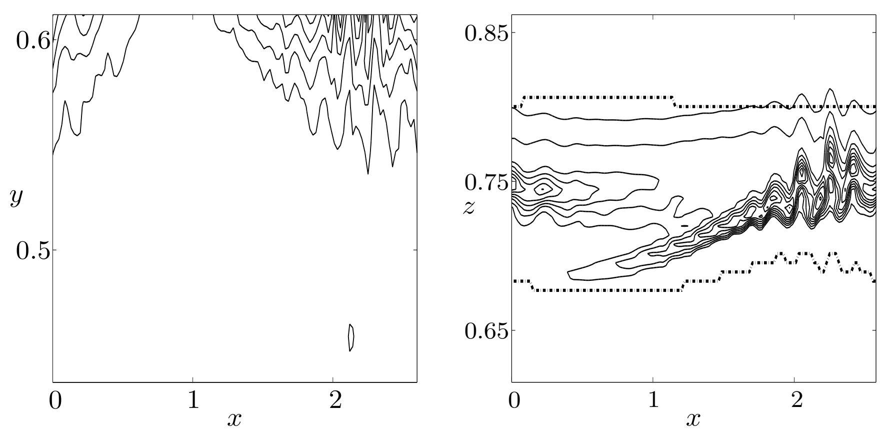

FIG. 18 – Left panel : horizontal plot of the maximum along each vertical line of the y-component of relative vorticity. Right panel : y-component of relative vorticity in the $(x - z)$ plane close to the northern boundary ($y = 0.6$) after the RK saturation ($t = 40$ on figure 16). The dash-dotted lines indicate the localization of the front as in figure 9.

modulate the front and the associated Ri. During the growth stage of the instability this will almost unavoidably lead to regions with $Ri < 0.25$, and shear instability is likely to occur. It was verified in the simulation that the small-scale instabilities develop in regions where Ri is minimal (less than 0.1), due to the compression of the front associated with the RK mode (indications of this may be seen in figure 18, right panel).

Now, the small-scale motions are only barely resolved : the horizontal resolution of the simulation is about $dx = 0.022$ while the small-scale motions have a spatial wavelength $\lambda_x = 0.125$, which means about 6 grid points per wavelength. In the reference run, similarly, their wavelength is about $\lambda_x = 0.25$, again corresponding to about 6 grid points. To check the importance of the small-scale aspects of the flow, we have investigated the sensitivity of our results to diffusion. We used the standard, second order scheme for diffusion, in the horizontal directions alone, or in the horizontal and vertical directions. However, a crucial point to note is that the front in the basic state is itself a small-scale feature and therefore is affected by the diffusion. For too large values of the diffusivity, typically values of the related Reynolds number less than $Re \sim 2000$ (calculated based on the grid-size), the diffusion of the front precedes the development of RK instability. Comparatively, the development of the classical baroclinic instability is much more robust and persists for Reynolds numbers about $Re \sim 100$ or less in our simulations. For larger values of the Reynolds number, the diffusion was not found to alter significantly the dynamics described above. Hence it appears that the dissipation introduced in the last simulations did not have any significant effects on the small-scale dynamics involved in the saturation of the RK instability.

Mean flow response

The saturation of the RK mode can be understood by describing the effect of the small-scale motions on the mean zonal flow. These motions develop where the RK mode most strongly modulates the front, i.e. on the lateral boundary to which the Kelvin wave is attached. The modifications of the zonally averaged flow due to the small-scale instabilities are shown in figure 19. The main modifications are the broadening of the frontal zone and a deceleration of the zonal flow in the upper layer and near the northern boundary, i.e. where the Kelvin wave was most intense.

As the velocities in the upper layer are reduced, conditions for the propagation of Kelvin waves are significantly changed. It appears that this mechanism is sufficient to break the conditions for the existence of the unstable mode, which essentially disappears after it has saturated (cf. figure 16). Indeed as the zonal velocity of the mean flow decreases close to the northern boundary of the upper layer, the Kelvin wave has a greater phase speed (it is propagating against the flow). The Rossby wave in the lower layer will keep the same phase speed as the mean flow speed does not change in the lower layer. Hence it will become more difficult to couple the two waves by making the Doppler-shifted phase velocities coincide. The corresponding unstable mode will have a weaker growth rate, if any.

In order to verify this point, the linear stability of the two-layer model was revisited for a flow in which the velocity of the upper layer decreases near the appropriate lateral boundary. It was found that the existence of the RK modes was indeed very sensitive to the deceleration of the flow there and that the mode disappears if the deceleration was sufficient, which supports our interpretation.

Simulations which exhibited a RK mode with the Kelvin wave in the lower layer near the southern boundary provided further support for this interpretation. In these simulations the small-scale instabilities lead to a broadening of the frontal zone and a

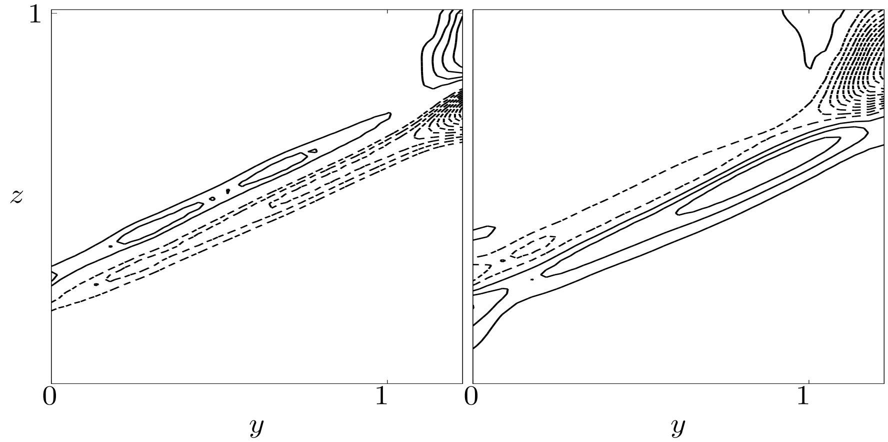

FIG. 19 – Potential temperature deviation (left) and zonal mean flow deviation (right) from the initial state (figure 9) after the Rossby-Kelvin mode saturation (cf. figure 16). The contour intervals are $0.25\,K.m^{-1}$ (left) and $2\,m.s^{-1}$ (right).

deceleration of the flow in the lower layer near the southern boundary, again changing the propagation conditions for the Kelvin wave in a way such that the RK mode disappears.

5.2.5 Summary

The linear stability of a front in a rotating, stratified fluid has been investigated with a focus on the ageostrophic modes of instability. These are by construction absent in the balanced models, such as the quasi-geostrophic approximation (e.g. Pedlosky (1987)), and hence constitute an example of coupling between balanced and unbalanced motions. Key questions regarding these modes are to determine their structure and growth rates, and to understand how they nonlinearly saturate.

Our starting point was the investigation by Sakai (1989) of the linear stability of a front in a rotating two-layer fluid, confined between vertical walls and horizontal surfaces. We have used a collocation method (Poulin & Flierl (2003)) to re-examine Sakai's configuration and extend the results to more general configurations. Configurations with layers of different depths exhibited two different families of Rossby-Kelvin (RK) modes : one with the Kelvin wave in the top layer, the other with the Kelvin wave in the bottom layer. When the two layers have sufficiently different depths, the two regions separate and hence a larger region of parameter space yields instabilities (cf. Fig. 5).

The unstable modes appear significant because of their relatively large growth rates. This is in contrast with ageostrophic unstable modes found for flows having constant shear (Molemaker *et al.* (2005); Plougonven *et al.* (2005)). However, as RK modes have been previously exhibited only in the two-layer rotating shallow water model, it was necessary to confirm that these modes also exist in a continuously stratified fluid, and to investigate their sensitivity to the sharpness of the front. To answer these questions, numerical simulations of the evolution of a sharp front in a stratified atmosphere were carried out with an idealized configuration of the Weather Research and Forecast Model (Skamarock *et al.* (2005)). The considered background state was comparable to the 2-layer model (sharp front confined by two lateral walls) but was more realistic in several aspects (background mean stratification, upper boundary condition, compressibility). Nevertheless, the RK modes were found to be present, demonstrating the robustness of the ageostrophic modes identified using the two-layer model. For sufficiently sharp fronts, the structure and growth rates of the modes were found to be comparable to the ones found in the two-layer model. However, sensitivity experiments showed that the growth rates of the modes were quite sensitive to the thickness of the front : they developed only for fronts having nondimensional thicknesses smaller than 0.15.

Once the presence of the RK modes in the continuously stratified fluid was established, their nonlinear behaviour has been investigated with the following important conclusions : *1)* the modes grow to finite amplitude, but retain energy levels that are small relative to the energy levels reached by the standard baroclinic instability. *2)* Their saturation involve small-scale instabilities, presumably Kelvin- Helmholtz type shear instabilities, in the region where the growing RK mode increases the shear of the front sufficiently. These instabilities develop near the lateral boundary where the Kelvin wave propagates. Their effect on the zonal flow is concentrated within the frontal zone in the vertical, and near the boundary where the Kelvin wave was present, in the horizontal. The deceleration of the flow there changes the conditions for wave propagation and hence breaks the conditions for the existence of the unstable mode, which essentially disappears. *3)* Although the details of the saturation may not be entirely reliable due to resolution limitations, the effect of the unstable modes on the energy budget is clear : contrary to the classical baroclinic instability, kinetic energy is converted to potential energy (in the simulations presented, about 2% of the kinetic energy is lost). The fact that RK instability leads to a conversion of kinetic to potential energy could be of particular interest in the oceanic context (cf. Wunsch & Ferrari (2004)). However, because the unstable modes are found to saturate at small amplitude, and because they are described here in a specific configuration with lateral walls, its significance in the open water is to be further investigated.

Further study of the stability of fronts is under way for related configurations : in an axisymmetric annulus, with applications to laboratory experiments in mind, and for a front that intersects either of the horizontal surfaces, with both oceanic and atmospheric situations in mind.

5.3 Conclusion

La stabilité linéaire d'un front dans un fluide stratifié tournant a été étudiée dans les cas d'un fluide à deux couches dans un canal, avec une attention particulière pour l'instabilité RK, absente par construction des modèles équilibrés, et qui constitue un exemple remarquable de couplage entre mouvements équilibrés et non-équilibrés. Nous avons d'abord validé la méthode de collocation utilisée en reproduisant les résultats du cas symétrique étudié par Sakai (1989) avec deux couches d'égales hauteur. Nous avons ensuite analysé les instabilités dans des cas plus généraux avec notamment deux couches de hauteurs différentes ou des paramètres de stratifications variables. Dans les deux cas les effets sont similaires et brise la "symétrie" entre les deux couches. On pourra se reporter à l'annexe A pour la même étude avec surface libre, qui montrent des résultats très similaires. Le point le plus important de cette analyse, comme cela avait déjà été relevé dans le chapitre précédent, est que dans cette configuration l'instabilité RK possède des taux de croissances relativement importants, contrairement aux autres exemples d'instabilités agéostrophiques mentionnés dans la partie 1.2.3 (Molemaker *et al.* (2005); Plougonven *et al.* (2005)).

Nous avons ensuite montré la pertinence de ces modes pour des écoulements continument stratifiés à l'aide de simulations idéalisées effectuées avec le modèle météorologique méso-échelle WRF (canal périodique entre deux murs latéraux). Les modes d'instabilité de Rossby-Kelvin apparaissent à nouveau, avec une structure qualitativement très comparable à celle obtenue dans le cas du fluide à deux couches. Les taux de croissance eux-mêmes sont quantitativement comparables aux taux de croissance obtenus dans le cas du fluide à deux couches, malgré des différences importantes entre les deux modèles. Toutefois les simulations ont également montré que les paramètres de stratification ou d'épaisseur du front influencent énormément les valeurs des taux de croissance. Cette étude confirme donc l'existence de ces modes d'instabilité dans des régions frontales d'un fluide continument stratifié, mais avec une sensibilité importante à l'intensité du front.

Ces simulations ont aussi permis d'étudier l'évolution non-linéaire de ces instabilités avec les conclusions suivantes : Ces modes croissent rapidement jusqu'à une amplitude finie, à des niveaux énergétiques bien inférieurs à ceux de l'instabilité barocline classique. Ensuite, la saturation de ces modes fait apparaître des instabilités de petite échelle dans les régions où la croissance du mode RK a suffisamment intensifié le cisaillement, c'est-à-dire principalement le long du bord sur lequel se propage l'onde de Kelvin. C'est aussi dans cette région que les effets de ce mode sur l'écoulement moyen se manifestent, correspondant à un ralentissement de l'écoulement zonal. Cette modification de l'écoulement modifie les conditions d'existence de cette instabilité et amène ainsi à sa disparition. Enfin les effets de ce mode instable sur le budget énergétique montrent que, contrairement à l'instabilité barocline classique, l'énergie cinétique est ici convertie en énergie potentielle. Cette dernière propriété est d'un intérêt particulier dans le contexte océanique (cf. Wunsch & Ferrari (2004)).

Nous avons vu dans cette étude l'importance des bords verticaux pour le développement de l'instabilité RK. L'analyse de stabilité linéaire comme les simulations non-linéaires montrent que le couplage entre un mode de Rossby et un mode de Poincaré est beaucoup plus faible que le couplage de l'onde de Rossby avec le mode de Kelvin, comme le laissait penser d'autres exemples de couplage entre mouvements vorticaux et ondes d'inertie-gravité (Molemaker *et al.* (2005); Plougonven *et al.* (2005)). Ce type de couplage présente donc une importance particulière pour les situations où il y a présence d'un guide d'onde, comme par exemple à l'équateur, ou dans une situation très importante dans le contexte océanique qui est le courant côtier. Nous allons donc nous intéresser dans le chapitre 6 à des instabilités similaires dans le cas de courants côtiers.

Chapitre 6

Instabilités d'un courant côtier : analyse linéaire et évolution non-linéaire

'L'océan s'offrait, déshabité, calme au large, effervescent sur les bords.'
Paul Morand.

6.1 Introduction

La compréhension des mécanismes qui gouvernent la stabilité des écoulements côtiers revêt une importance considérable en océanographie car ils conditionnent les échanges entre la côte et le large en formant des méandres et des tourbillons. Une bonne compréhension des mécanismes de formation et d'évolution de ces méandres et de ces tourbillons est donc importante vis à vis du transport de polluants ou de la fertilisation des eaux du large par apports terrigènes. Par exemple, l'eau de l'Atlantique entrant dans la mer Méditerranée forme le courant Algérien, en restant à la surface en raison de sa densité plus faible. Or le Courant Algérien va influencer la circulation générale de toute la Méditerranée Occidentale par ses mécanismes d'instabilité, qui se traduisent par une importante activité à méso-échelle, avec formation de méandres et de tourbillons. Il existe beaucoup d'autres exemples comme le courant de Leeuwin (figure 6.1), le courant Norvégien, etc.

Nous allons donc entreprendre dans la suite l'analyse linéaire des instabilités pour des courants côtiers en procédant de manière similaire aux chapitres précédents, et ensuite étudier l'évolution non-linéaire de ces instabilités, et notamment la formation de tourbillons par ces mécanismes d'instabilité, à l'aide du code numérique en volume fini décrit dans la partie 3.2. Nous nous intéresserons d'abord à un modèle à gravité réduite dans la partie 6.2 et ensuite à un modèle à deux couches dans la partie 6.4.

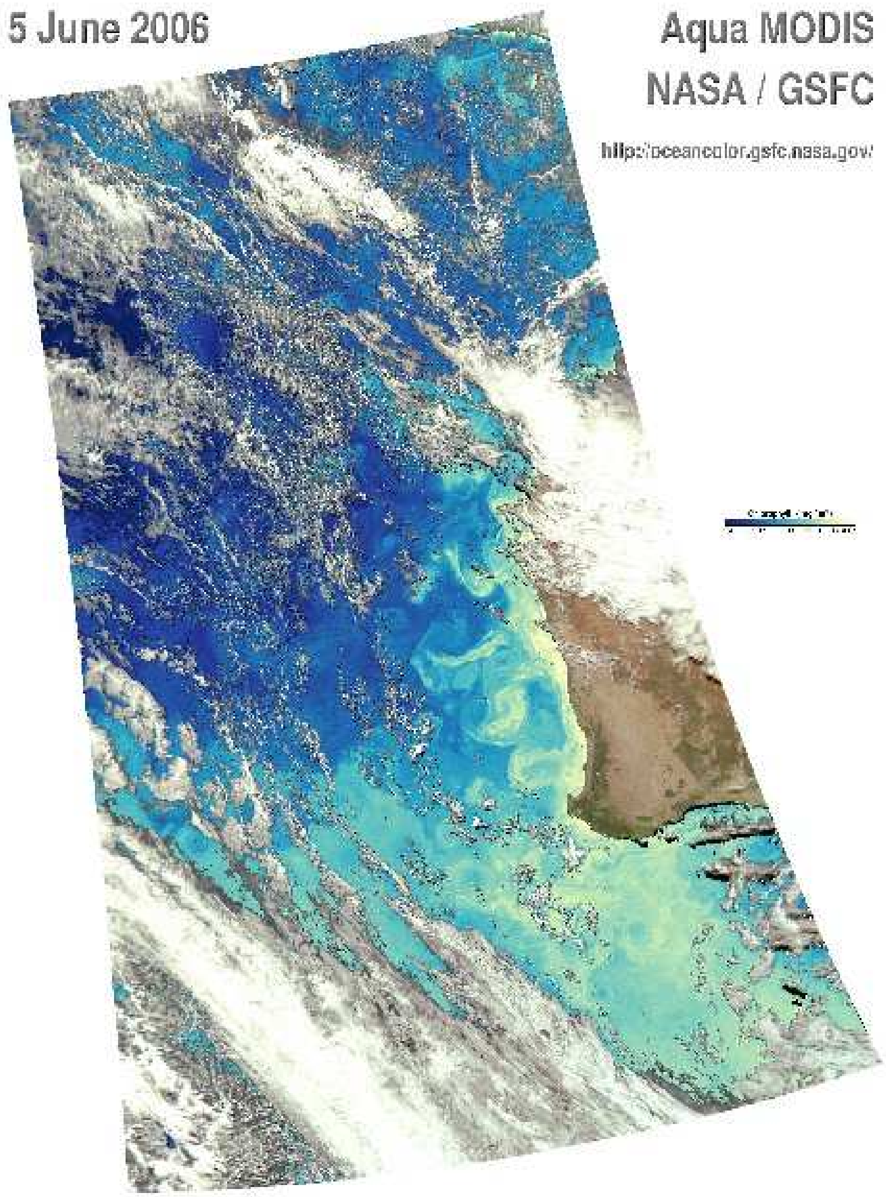

Fig. 6.1 – Concentration en chlorophylle dans le courant de Leeuwin (NASA/GSFC).

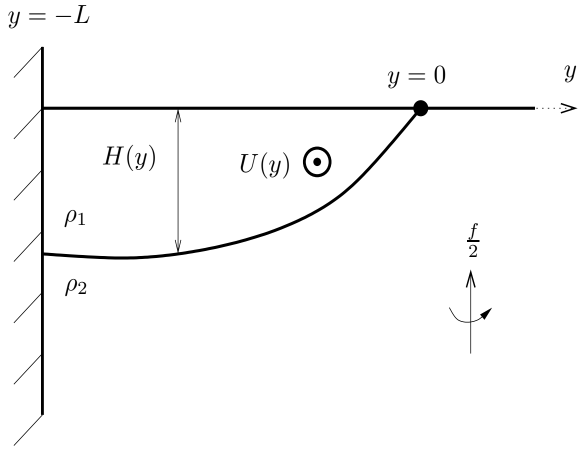

FIG. 6.2 – Schematic representation of the coastal current bounded by a density front.

6.2 *Instabilities of buoyancy driven coastal currents and their nonlinear evolution in the two-layer rotating shallow water model. Part I. Passive lower layer*

Le modèle de l'eau peu profonde en gravité réduite est un modèle très utilisé pour la représentation des courants côtiers. On considère alors une couche de fluide de densité constante avec d'un côté un bord vertical et de l'autre un front (outcropping) comme représenté sur la figure 6.2. La couche inférieure, de densité supérieure, est au repos comme expliqué précédemment (partie 2.1).

Dans ce modèle, Killworth & Stern (1982) ont montré que l'écoulement pouvait devenir instable dans deux situations, lorsque l'écoulement possédait un gradient de vorticité potentielle négatif, ou si la vorticité potentielle de l'écoulement était quasiment constante mais que la vitesse de celui-ci changeait de signe entre le front et la côte. Ensuite Paldor (1983), Kubokawa & Hanawa (1984) et Kubokawa (1986) ont montré dans le cas d'écoulements à vorticité potentielle nulle, que ceux-ci pouvaient développer une instabilité de type barotrope, issue de la résonance entre un mode frontal se propageant le long du front et d'une onde de Kelvin de propageant le long du bord. Toujours dans le cas d'écoulements à vorticité potentielle nulle Stern (1980) et Paldor (1988) ont étudié l'évolution de perturbations (à vorticité potentielle nulle aussi) et montré que celles-ci obéissaient à l'équation de Korteweg-de Vries (voir par exemple Pedlosky (1987)) et avaient donc la forme de solitons ou d'ondes cnoidales. On peut retrouver une étude similaire pour des écoulements de vorticité potentielle constante dans Dahl (2005).

Les résultats sur l'instabilité et l'évolution nonlinéaire des courants côtiers dans le modèle à gravité réduite font l'objet d'un article soumis à *Journal of Fluid Mechanics* (Gula & Zeitlin (2009)). Ainsi nous les incluons en anglais.

Instabilities of buoyancy driven coastal currents and their nonlinear evolution in the two-layer rotating shallow water model. Part I. Passive lower layer.

J. Gula & V. Zeitlin [1]

Buoyancy driven coastal currents which are bounded by a coast and a surface density front are ubiquitous, playing essential role in the mesoscale variability of the ocean. Their highly unstable nature is well known from observations, laboratory and numerical experiments. In the present paper we revisit the linear stability problem for such currents in the simplest reduced gravity model and study nonlinear evolution of the instability by direct numerical simulations. By using the collocation method, we benchmark the classical linear stability results on zero-PV fronts, and generalize them to non-zero PV fronts. In both cases, we find the instabilities due to the resonance of frontal and coastal waves trapped in the current, and identify the most unstable long-wave modes. We then study the nonlinear evolution of the unstable modes with the help of a new high-resolution well-balanced finite-volume numerical scheme for shallow-water equations. The simulations are initialized with the unstable modes obtained from the linear stability analysis. We found that the principal instability saturates in two stages. At the first stage the Kelvin component of the unstable mode breaks forming a Kelvin front and leading to the reorganization of the mean flow through dissipative and wave-meanflow interaction effects. At the second stage a new, secondary unstable mode of the Rossby type develops on the background of the reorganized mean flow, and then breaks forming coherent vortex structures. We investigate the sensibility of this scenario to the along-current boundary and initial conditions. A study of the same problem in the framework of fully baroclinic 2-layer model will be presented in the companion paper.

6.2.1 Introduction

Coastal currents in the ocean are commonly produced by joint effects of buoyancy and the Coriolis force. For example, the Atlantic water entering the Mediterranean Sea forms the Algerian current, remaining at the surface due to its low density. There exist many other examples of the same type such as the Leeuwin Current, the East Greenland Current, the Norwegian Coastal Current, etc. Such boundary currents generally become unstable, producing meanders and detachment of vortices away from the coast. Eventually these instabilities control the horizontal mixing by the current. They play therefore an important role in the distribution of the biogeochemical components and their transfer between basins.

A widely used idealized model for studying dynamics of coastal currents is the reduced gravity rotating shallow-water model in the half plane, where the effects of density stratification are modelled by a single reduced gravity parameter, and the system is represented by a single-layer finite depth constant-density fluid terminating at the free streamline (surface front). The lower layer is then assumed to be infinitely deep so the pressure there remains constant. Linear stability of density-driven coastal currents with a surface front in such configuration in the inviscid limit has been investigated by Killworth & Stern (1982), Paldor (1983), and Kubokawa (1986). Killworth & Stern (1982) showed that a coastal density current is unstable to long wave disturbances in two cases : when the mean potential vorticity (PV in what follows) increases towards

[1]LMD, Ecole Normale Supérieure,
24, rue Lhomond, 75231 Paris Cedex 05, France

the wall (coast), and the mean tangent velocity is zero at the wall, and when the mean flow is close to uniform PV, if the velocity of the current is reversed between the coast and the front. Paldor (1983) examined the linear stability of a current with zero-PV, and Kubokawa (1986) demonstrated that for a zero-PV flow there is an instability of barotropic type, produced by the resonance between a frontal trapped wave and a coastal trapped wave.

Although the reduced gravity model is a good first approximation, it obviously neglects dissipative effects, including Ekman pumping, and oversimplifies stratification. The former may be, in principle, parameterized, for the sake of applications, and the latter may be taken into account by using a full two-layer rotating shallow water model. In many situations the lower layer cannot be considered dynamically inactive, and new and important phenomena appear in the dynamics when the lower layer has a finite vertical thickness. Killworth *et al.* (1984) examined a free front far away from the wall, overlying an active lower layer with no motion in the basic state, and showed that the front is always unstable to long-wave perturbations regardless of the distribution of PV, with much larger growth rates than in the one-layer case. In such two-layer model, the mean flow in the upper layer forces the density interface to tilt and hence PV in the lower layer decreases toward the surface front. The PV gradient then allows for the existence of vortical waves in the lower layer which can couple with a frontal wave and cause the instability. The stability of a coastal upwelling front in a two-layer shallow water model was investigated by Barth (1989a,b) and a baroclinic-type instability was found. Paldor & Ghil (1991) studied a zero-PV front with an active lower layer and found vigorous short-wave instabilities whenever the slanting interface between the layers extends close to the bottom of the ocean. These short-wave instabilities are similar to the classical Kelvin-Helmoltz instability.

The instabilities of the coastal fronts were also subject to experimental investigation. Without giving an exhaustive review, let us mention the classical paper by Griffiths & Linden (1982), where adjustment and subsequent development of the instability of the fronts, with secondary vortex formation, was studied in the two-layer system in the rotating annulus for a wide range of depth ratios of the layers.

In the present (Part I) and companion (Part II) papers we present a systematic study of the instability, including its nonlinear stage, of the density driven coastal currents in the framework of one-layer (Part I) and two-layer (Part II) rotating shallow water models in the inviscid limit. In spite of its simplicity, the shallow-water model contains all essential ingredients of large-scale atmospheric and oceanic dynamics. Its physical transparency greatly helps while performing the linear stability analysis and interpreting the results. At the same time, the model, both in one- and multi-layer versions allows for efficient numerical treatment by using a new generation of high-resolution well-balanced finite-volume numerical schemes (Bouchut (2004), Bouchut (2007), Bouchut & Zeitlin (2009)). The shock-resolving property of these schemes is particularly important for the coastal configurations due to the dispersionless character of coastal Kelvin waves and their ability to break and to form Kelvin fronts (Fedorov & Melville (1995)). Also crucial in the context of the density fronts is the property of these numerical schemes to successfully treat drying (one-layer schemes) and outcropping (multi-layer schemes).

Below we will adopt a simple strategy consisting in identifying the most unstable modes of the coastal current configuration by a detailed stability analysis (we use the collocation method, Trefethen (2000)), and then using them for initialization of the DNS with finite-volume well balanced scheme in order to study nonlinear evolution and saturation of the instability. A similar strategy with the same tools was recently used

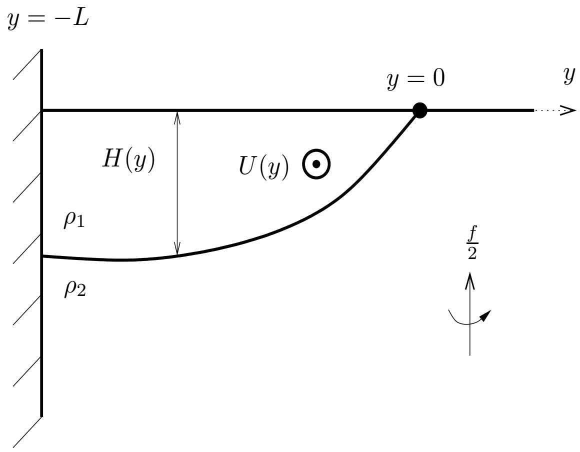

FIG. 3 – Schematic representation of the coastal current bounded by a density front.

for studying a close, but simpler problem of double density fronts (Scherer & Zeitlin (2008)). In the present paper we limit discussion by the one-layer model, the analysis of two-layer configurations is postponed to the Part II.

6.2.2 The model and the linear stability problem

Equations of motion, boundary conditions, and steady states

A typical configuration of a density-driven coastal current is shown in figure 3. The undisturbed flow is bounded by a surface front at $y = 0$, and by a rigid vertical boundary at $y = -L$, and the density gradient between the fluid layers is sharp. As is well known, in the limit of infinitely large thickness of the lower layer the problem can be reformulated in terms of shallow-water equations with the reduced gravity replacing the standard gravity.

The equations of the rotating shallow-water model on the f-plane are :

$$\begin{aligned} u_t + uu_x + vu_y - fv &= -gh_x, \\ v_t + uv_x + vv_y + fu &= -gh_y, \\ h_t + (hu)_x + (hv)_y &= 0, \end{aligned} \tag{1}$$

where (x, y) and (u, v) are the zonal and meridional coordinates and velocity components, respectively, h is the fluid depth, g is the reduced gravity, f is the constant Coriolis parameter, and the subscripts denote corresponding partial derivatives.

The basic state is assumed to be steady. It is easy to see that geostrophically balanced fields $u = U(y)$, $v = 0$, and $h = H(y)$,

$$U(y) = -\frac{g}{f} H_y(y) \tag{2}$$

provide an exact stationary solution of the equations (1).

We linearize equations (1) about this steady state. The linearized equations, where $u(x, y, t)$, $v(x, y, t)$ and $h(x, y, t)$ now denote the perturbations to the basic state fields, are :

$$\begin{aligned} u_t + Uu_x + vU_y - fv &= -g\, h_x, \\ v_t + Uv_x + fu &= -g\, h_y, \\ h_t + Uh_x &= -(Hu_x + (Hv)_y). \end{aligned} \tag{3}$$

We introduce the time scale f^{-1}, the horizontal scale L, which is the unperturbed width of the current, the velocity scale fL, and the vertical scale $(fL)^2/g'$. We will use only non-dimensional variables from now on without changing notation. Note that within this scaling the typical value of the velocity gives the value of the Rossby number. The following non-dimensional equations follow :

$$\begin{aligned} u_t + Uu_x + vU_y - v &= -\, h_x, \\ v_t + Uv_x + u &= -\, h_y, \\ h_t + Uh_x &= -(Hu_x + (Hv)_y). \end{aligned} \tag{4}$$

We impose the free-slip boundary condition at the coast : $v(-1) = 0$. The boundary conditions at the front are :

$$H(y) + h(x, y, t) = 0, \quad D_t Y_0 = v \quad at \quad y = Y_0 \ , \tag{5}$$

where $y = 0$ is the location of the free streamline of the balanced flow and $Y_0(x, t)$ is the position of the perturbed free streamline, D_t is the Lagrangian derivative. Physically, they correspond to the conditions that the fluid terminates at the boundary which is a material line. The linearized boundary conditions give :

- the relation between the perturbation of the position of the free streamline and the value of the height perturbation :

$$Y_0 = -\frac{h}{H_y}\bigg|_{y=0}, \tag{6}$$

- the continuity equation (1) evaluated at $y = 0$.

Hence, the only constraint to impose on the solutions of (4) is regularity of solutions at $y = 0$.

The PV of the mean flow, in non-dimensional terms, is :

$$Q(y) = \frac{1 - U_y}{H(y)}, \tag{7}$$

where the geostrophic equilibrium holds :

$$U(y) = -H_y(y). \tag{8}$$

The basic state height is then given by the solution of the following ODE :

$$H_{yy}(y) - Q(y)H(y) + 1 = 0, \ with \begin{cases} H(0) = 0 \\ H_y(0) = -U_0, \end{cases}$$

where $U(0) = U_0$ is the mean flow velocity at the front.

If we assume a zero PV flow : $Q(y) = 0$, it corresponds to the solution :

$$\begin{cases} H(y) = -U_0 y - \frac{y^2}{2}, \\ U(y) = U_0 + y. \end{cases}$$

which has been used by Stern (1980), Paldor (1983), and Kubokawa (1985). In the limit $U_0 = 1/2$, this profile also coincides with that used by Griffiths *et al.* (1982), who investigated the instability of a current bounded by two surface fronts, yet the two problems are not equivalent due to the different boundary conditions at $y = -1$.

If we assume a constant PV flow : $Q(y) = Q_0 \neq 0$, it corresponds to the solution :

$$\begin{cases} H(y) = \frac{1}{Q_0}[1 - U_0\sqrt{Q_0}\, sinh(\sqrt{Q_0}y) - cosh(\sqrt{Q_0}y)], \\ U(y) = U_0\, cosh(\sqrt{Q_0}y) + \frac{1}{\sqrt{Q_0}}\, sinh(\sqrt{Q_0}y). \end{cases}$$

which is similar to the solution used by Dahl (2005). The basic state height and velocity for both cases are plotted in figure 4.

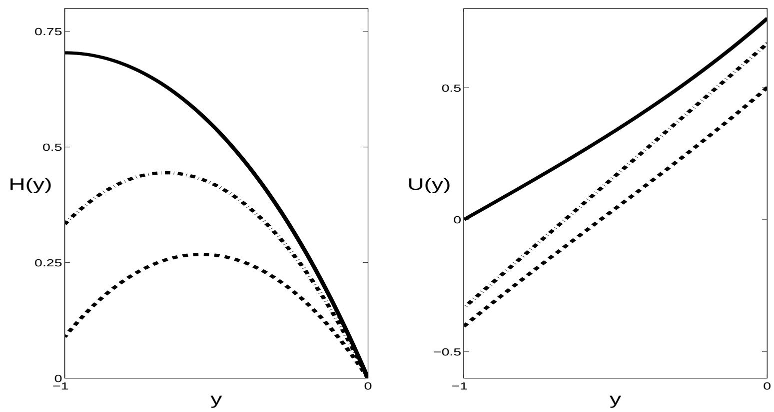

FIG. 4 – Examples of the basic state heights (left) and velocities (right) for constant PV flows with $U_0 = -sinh(-1)/cosh(-1)$ (thick line), $U_0 = 1/2$ (dotted line) and a zero PV flow (dash-dotted line)

Stability analysis by the collocation method

Assuming a harmonic form of the solution of (4) in the x-direction,

$$(u(x,y), v(x,y), h(x,y)) = (\tilde{u}(y), \tilde{v}(y), \tilde{h}(y))\ exp\,[i(kx - \omega t)], \tag{9}$$

we obtain an eigenvalue problem of order 3 which can be solved by applying the spectral collocation method as described in Trefethen (2000) and Poulin & Flierl (2003). A complete basis of Chebyshev polynomials is used to obtain a discrete equivalent of the equations. This is achieved by evaluating (4) on a discrete set of N collocation points (typically $N = 50\ to\ 100$). The eigenvalues and eigenvectors of the resulting operator are computed with the Matlab routine "eig". The occurrence of spurious eigenvalues is common in such discretization procedure. We therefore checked the persistence of the obtained eigenvalues by recomputing the spectrum with increasing N.

The disadvantage of the method is that it is not specially designed for treating singular eigenproblems. Indeed, the eigenproblem which results from injecting (9) into (4) has a well-known critical-layer singularity occurring whenever the real part of the eigen phase velocity of the perturbation $c = \omega/k$ is equal to the local flow velocity : $c = U(y)$. Singularities give rise to the stable singular eigenmodes which form a continuous spectrum (see e.g. Vanneste (1998) for a similar albeit simpler geophysical fluid dynamics problem with critical layers). These modes have Dirac-delta or stepfunction behaviour (depending on the variable) being, in fact distributions, not functions. Discrete counterparts of such singular eigenmodes will be retrieved by the straightforward collocation method. They may be, nevertheless, easily identified by their singular profiles and the fact that they accumulate with increasing resolution (see below). A filtering procedure based on gradient limiters was applied to eliminate these pseudo-modes. The method was extensively tested in the related problem of coupled density fronts within the same model (Scherer & Zeitlin (2008)), where more technical details may be found.

Instabilities of density fronts as resonances between the eigenmodes

The stability of the coastal current configurations with a front bounded by a wall has been investigated in previous studies. First, Killworth & Stern (1982) showed that a coastal density current in a one-layer model is unstable to long wave disturbances in two cases : 1) when the mean PV gradient is positive at the wall and the mean velocity is zero at the wall, or 2) when the current is not unidirectional (mean along-coast velocity and depth slope changing sign between the front and the coast, cf. Fig. 4) for flows with close to constant PV. Paldor (1983) examined the condition for stability for a basic flow with zero PV and showed that the current is stable provided the mean velocity of the basic flow exceeds fL (where f is the Coriolis parameter and L the width of the current), but he wasn't able to find any unstable waves when the flow did not satisfy this criterion.

It should be stressed that the most physically transparent way to understand instabilities of a given flow is to interpret them as the resonances between the eigenmodes and corresponding crossings of dispersion curves. The most known examples come from baroclinic interactions in a vertically sheared flow, e.g. Jones (1967), Sakai (1989), but the same mechanism works for barotropic horizontally sheared flows, e.g. Satomura (1981), Hayashi & Young (1987)). It is, in particular, valid for the instabilities of the density fronts. Thus, the classical GKS instability as described in Griffiths *et al.* (1982), for the one-layer reduced gravity model of coupled density fronts (a gravity current that is bounded by two free streamlines), which was already mentioned above, results from the resonance between two eigenmodes propagating along each front, respectively, cf Pratt *et al.* (2008), Scherer & Zeitlin (2008). We will refer to such modes trapped in the vicinity of the density front as frontal modes. [2]

The coastal current configuration of the present paper does contain the frontal waves trapped in the vicinity of the front, but also has another type of localized modes which are trapped near the coast, e.g. Kubokawa & Hanawa (1984). Kubokawa (1986) showed that the flow is indeed unstable when the condition of stability of Paldor (1983) is not satisfied, and identified the corresponding unstable modes for the zero-PV configuration as a resonance between a frontal wave and a coastal trapped wave. In the idealized case of vertical boundary we are considering, the coastal trapped waves are just Kelvin and Poincaré waves.

The frontal wave is described in Iga (1993) as a mixed Rossby-gravity wave, in a sense that it behaves like a Rossby mode as long as the wavenumber is small, but like a gravity mode when the wavenumber becomes large. Note that Hayashi & Young (1987), among others, refer to this mode as a Kelvin wave. More generally, the frontal mode can be interpreted as a vortical mode as in Meacham & Stephens (2001), in a sense of a wave that exists due to the PV gradient at the outcropping point, because this point may be interpreted as a point connecting the finite-depth layer with a layer of infinitesimal thickness (Boss *et al.* (1996)).

As an example of the just-described resonance interpretation of the instability of the coastal current, we present the results of linear stability analysis for the constant-PV flow corresponding to the basic state given by (6.2.2), cf. figure 4. The growth rates of the most unstable modes are represented in figure 5 for $R_d = 1$ and U_0

[2]It should be mentioned that the instability of an *isolated front* in a one-layer reduced gravity model, described in Killworth (1983*a*) and Kubokawa (1985), is more complicated in nature than that of a pair of coupled fronts. It is a *critical layer* type instability which can be explained in terms of resonance between the frontal mode and a superposition of several singular modes from the continuous spectrum by the mechanisms described in Iga (1999), who showed that such instability can occur when the sign of the intrinsic phase speed of the non-singular mode (the frontal wave) and that of the gradient of the PV at the critical level are the same. A similar "critical layer" behaviour was noticed by Barth (1989*b*) in a configuration where the interface displacement has a rapide phase change across the point where the phase speed of the wave equals the mean flow velocity. An investigation of such configuration using the collocation method (not presented), perfectly matches this interpretation.

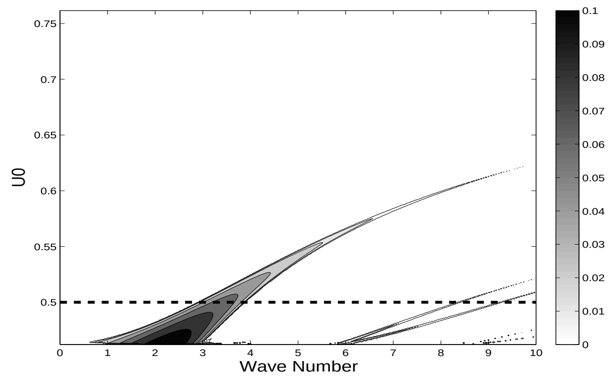

FIG. 5 – Stability diagram in the $(\frac{U_0}{fL}, k)$ plane for the constant PV current. The values of the growth rates corresponding to grey levels are given in the right column.

between the two limit values corresponding to : (a) zero velocity at the wall, resulting for $U_0 = -sinh(-1)/cosh(-1) \approx 0.75$, (b) zero height at the wall, resulting for $U_0 = [1 - cosh(-1)]/sinh(-1) \approx 0.46$.

Note that such basic state is always unstable within these limits, according to Ripa's criterion (Ripa (1983)), which states that sufficient conditions for stability are that :

$$\exists \alpha / \ \forall y \begin{cases} (U-\alpha)\frac{dQ}{dy} \leq 0, \\ (U-\alpha)^2 \leq g'H. \end{cases} \tag{10}$$

The first condition is always satisfied as $Q = const$. Due to the front at $y = 0$ $(H(0) = 0)$, the second condition can be satisfied only for $\alpha = U_0$. The flow will then be unstable as long as $(U_0 - U(-1))^2 \geq g'H(-1)$, which is verified in the range of U_0 plotted in figure 5.

Figure 6 represents the dispersion diagram in phase speed - wavenumber plane for $U_0 = 0.75$, which corresponds to a stable case with zero velocity at the wall. We can use this case in order to identify various modes typical for the coastal current configuration. Two sets of Poincaré waves marked by P_n can propagate either at the coast or at the front, and are, as usual, almost dispersionless in the short-wave limit and strongly dispersive in the long-wave limit. Kelvin mode (marked by K, with $c_K \approx 0.75$ in the figure) propagates uniquely along the coast with low dispersion, and the frontal mode (marked by F, with $c_F = 0$ at $k = 0$) is quite dispersive for low wavenumbers $k < 10$. The resonances between different modes will lead to instabilities when U_0 diminishes.

Figure 7 shows the dispersion diagram and corresponding growth rates as a function of k for $U_0 = 0.5$ corresponding to the dashed line in figure 5. The flow has a counter current and is now likely to become unstable according to the criterion exposed earlier. There are indeed several instability zones. The main area of instability ($k \approx 3.5$) corresponds to the resonance of the frontal mode and the Kelvin mode, as can be deduced from the intersection of the respective dispersion curves. Figure 8 shows the most unstable mode at $k = 3.44$, where one can recognize the characteristic structure of a Kelvin wave propagating along the coast ($y = -1$) with no normal to the wall velocity, and the frontal mode at the front ($y = 0$). Note the apparently balanced character (velocity following the isobars) of the frontal mode.

Other instability zones, visible in figure 7 at wavenumbers higher than 8, and with much lower growth rates, correspond to the resonance of the Kelvin mode and the first

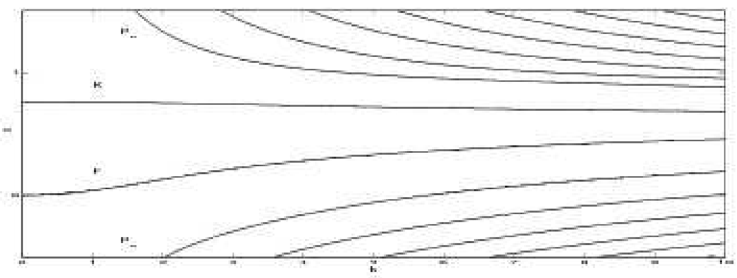

FIG. 6 – Dispersion diagram for $U_0 = -sinh(-1)/cosh(-1)$ and $Q_0 = 1$. The flow is unidirectional with zero zonal velocity at the coast, and is stable.

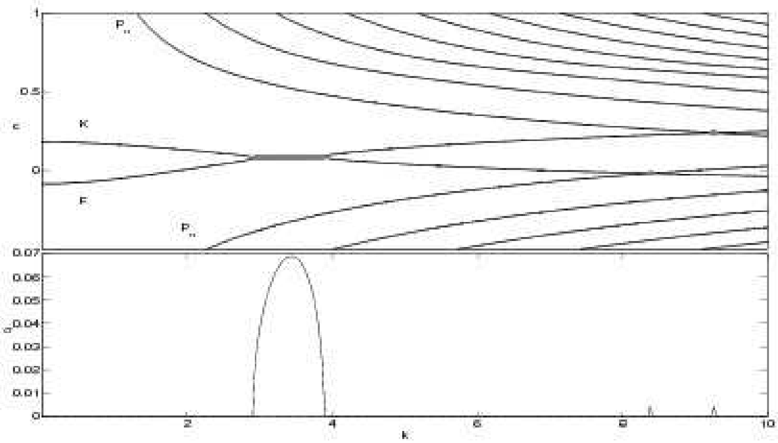

FIG. 7 – Dispersion diagram for $U_0 = 0.5$ and $Q_0 = 1$. The flow is unstable. Crossings of the dispersion curves in the upper panel correspond to instability zones and nonzero growth rates in the lower panel.

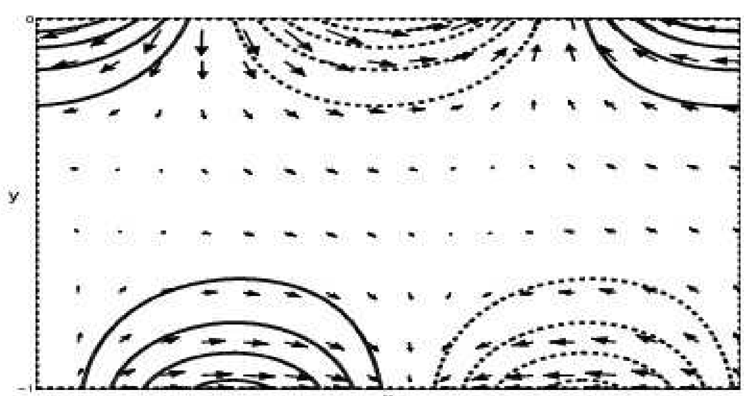

FIG. 8 – Height and velocity fields of the most unstable mode of figure 7 for $k = 3.5$, corresponding to the resonance between the Kelvin and the frontal mode. Only one wavelenght is plotted. On this and similar figures below full lines correspond to positive and the dotted lines to negative values.

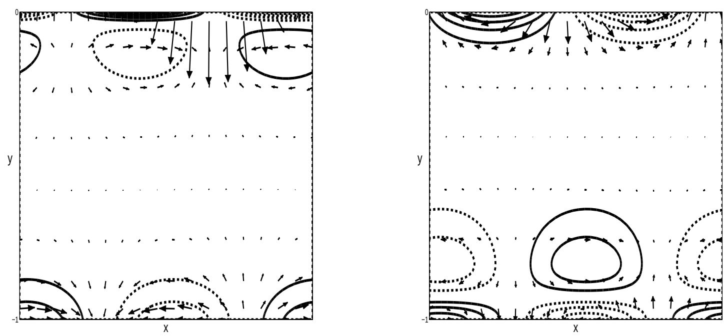

FIG. 9 – Height and velocity fields of higher wavenumber unstable modes of figure 7 for (a) $k = 8.4$ and (b) $k = 9.25$. (a) Resonance between the Kelvin and a frontally trapped Poincaré mode and (b) Resonance between a coastally trapped Poincaré mode and the frontal mode. Only one wavelenght is plotted.

frontally trapped unbalanced Poincaré mode, and the interaction of the first coastally trapped Poincaré mode with the balanced frontal mode, respectively. The structure of both unstable modes is presented in figure 9.

We also explored other basic state configurations with different heights and velocity profiles, with constant or non-constant PV, and got similar results, which we do not display. It should be noted that a return flow is not a necessary condition for the instabilities to occur, as a basic state with zero mean velocity at the coast can be unstable if the mean PV gradient is positive at the coast. For example a profile defined as :

$$H(y) = -\frac{f}{g}(U_0 y + \frac{1}{2}y^2 + \frac{L - U_0}{3L^2}y^3) \,, \tag{11}$$

$$U(y) = U_0 + y + \frac{L - U_0}{L^2}y^2 \,, \tag{12}$$

satisfies the necessary conditions for the frontal instability.

We, thus, confirmed and extended earlier results on linear stability of the coastal currents in the one-layer reduced-gravity model, and got a transparent physical interpretation of the instability in terms of wave-wave resonance, which will allow for better understanding of its nonlinear stage. We will perform below fully nonlinear DNS by initializing our numerical code with above-calculated unstable eigenmodes. It should be stressed that the collocation method gives the structure of the unstable modes with any desired accuracy.

6.2.3 Non-linear evolution of the leading instability

Brief reminder of the finite-volume methods for the rotating shallow-water model

Recent progress in finite-volume numerical schemes for shallow-water equations allows for implementationally simple and quantitatively reliable high-resolution modelling of fully nonlinear dynamics. We apply the high-resolution finite-volume numerical method by Bouchut (2004, 2007) which has the following properties, decisive in the context of outcropping coastal fronts/currents :

- it preserves geostrophic equilibria (i.e. the stationary states in the case of a straight front) ;
- it resolves wave breaking and shock formation ;
- it allows to treat outcropping/drying.

It should be stressed that no explicit dissipation is introduced in the numerical scheme.

As was shown in previous applications of the method by Bouchut *et al.* (2004, 2005)and Scherer & Zeitlin (2008), energy is extremely well-preserved, the only significant energy loss being associated with sharp gradient formation (shocks, or bores), Bouchut (2004), or with reconnection of the streamlines (barotropic Rossby, or frontal wave breaking, Bouchut *et al.* (2005) and Scherer & Zeitlin (2008), respectively), which produce localized dissipation zones. We briefly recall the main ingredients of the method. The shallow-water equations are discretized in the flux-form on a regular grid within the framework of the finite-volume approach. The finite-volume scheme is then fully prescribed by the choice of the numerical flux function and the treatment of the remaining source terms associated with the Coriolis force. At each time step and in each direction, the Coriolis terms are reformulated following the apparent topography method first introduced by Bouchut (2004). The numerical flux function is associated with a relaxation solver adapted to treat topography, as proposed by Audusse *et al.* (2004). This choice of the numerical flux function ensures the ability of the numerical procedure to compute solutions of the shallow-water equations even in the case of terminating depth. The advantage of the scheme is that correct Rankine-Hugoniot conditions guaranteeing the decrease of energy across the shocks are automatically satisfied by the method, i.e. numerical viscosity is indeed a dissipation. The numerical simulations presented hereafter were obtained with typical resolution 0.005 L and lasted for a couple of hours on a personal computer.

The numerical treatment of boundary conditions is usually done quite easily within the finite volume framework (see Bouchut (2004)). We typically work with periodic boundary conditions along the wall. The free-slip condition at the coast is realized by defining a symmetric ghost value in the cell beyond the wall, such as : $h_0^n = h_1^n$ and $v_0^n = -v_1^n$ for adjacent cells separated by the wall. The sponge boundary conditions, if necessary, are realized by extending the computational domain beyond the physical one by several cells, and annihilating the return momentum fluxes.

Non-linear evolution of the most unstable mode

We present below the results of the DNS of fully nonlinear evolution of the instability corresponding to the most unstable mode with $k_0 = 3.44$ with the structure presented at figure 8. The boundary conditions are periodic in the zonal direction, with a period $\frac{2n\pi}{k_0}$. Thus, the periodicity with n wavelengths of the most unstable mode is imposed in the simulation. The numerical method allowing for drying, we compute the solution on the $[-L, 5L]$ interval in the meridional direction with a free-slip condition at the wall at $y = -L$ and a sponge boundary condition at $y = 5L$. The front being initially situated at $y = 0$, we carefully check that the fluid never reaches the boundary at $y = 5L$ during simulations.

The evolution of the height field in the (x, y)-plane is shown in figures 10 and 11 for $n = 1$. As can be inferred from the figure 12 (left panel) where the time evolution of the energy of the perturbation is displayed, the instability initially develops exponentially (for $t < 20$). The average growth rate during this first stage is $\sigma \approx 0.06$, relatively close to the value obtained from the linear stability analysis (see figure 7).

As we have shown earlier, the unstable mode under investigation is composed of a

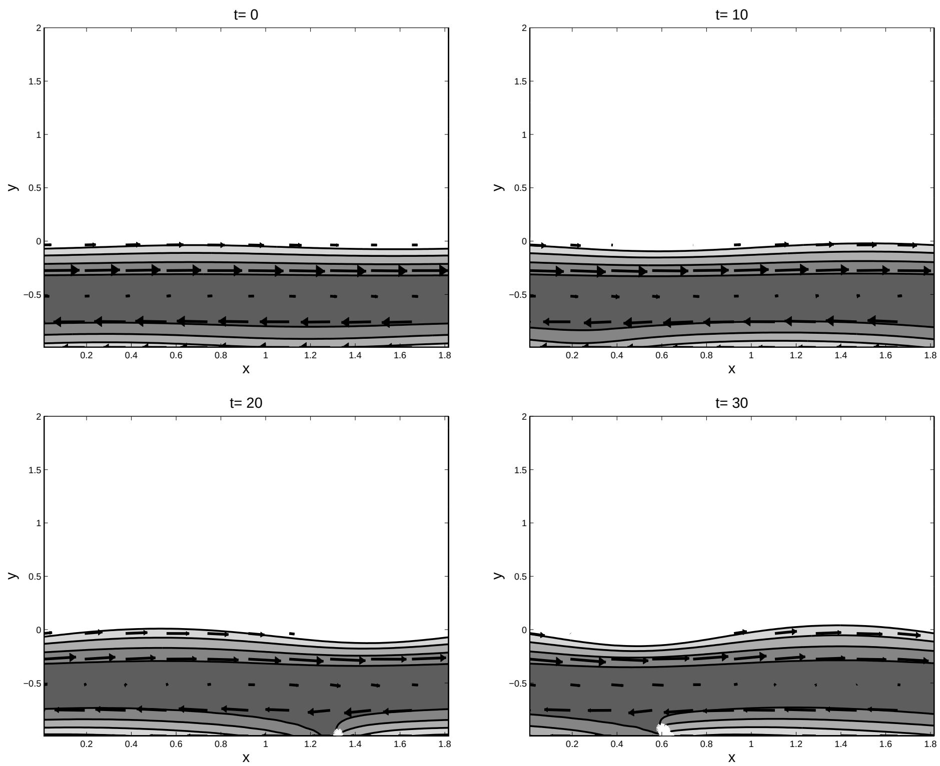

FIG. 10 – Levels of $h(x, y, t)$ at the interval 0.05 at $t = 0, 10, 20, 30$ for the evolution of the most unstable mode of figure 8 corresponding to the basic flow with constant PV as defined by (6.2.2). The arrows indicate the mass flux $h\vec{v}$. The initial amplitude of the perturbation is 10% of the maximum depth of the balanced flow. The calculation domain is periodic in the x-direction and corresponds to one wavelenght of the most unstable mode. White area superimposed on the isolines of the height field gives spatial distribution of the dissipation rate beyond the threshold 0.003 and up to maximum value 0.03. The dissipation rate is calculated as the deviation from the energy balance in each cell per time-step in non-dimensional units.

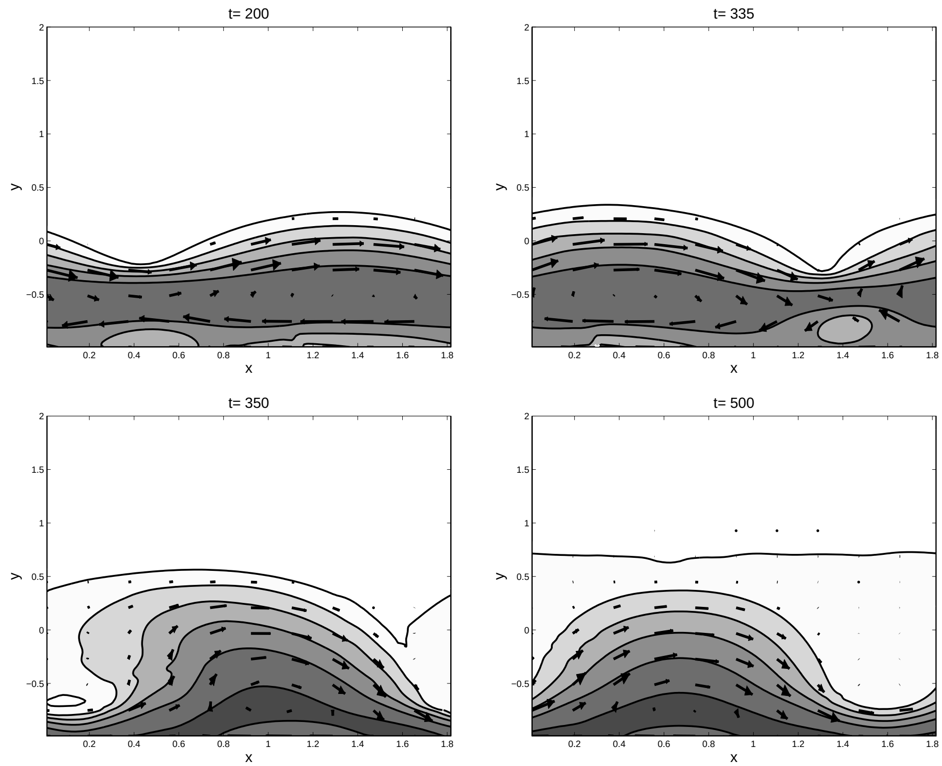

FIG. 11 – Same as in Fig. 10 but at $t = 200, 335, 350, 500$. The second stage of the development of the most unstable mode of figure 8. Contours correspond to 0.01, 0.05, and further on at the interval 0.05.

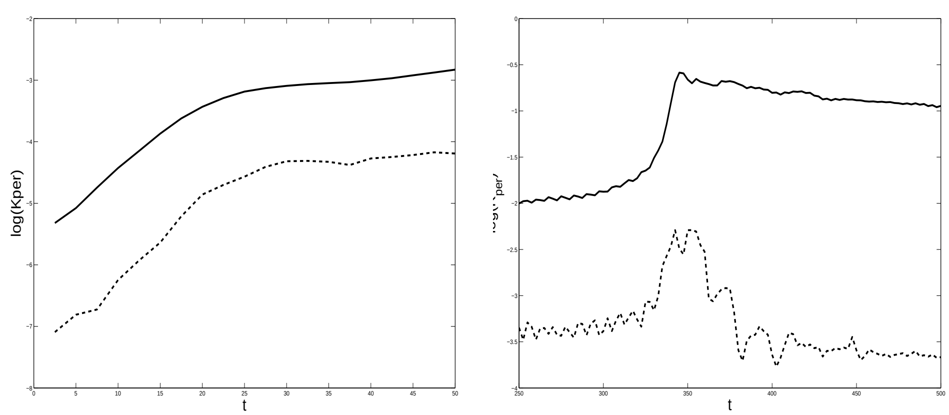

FIG. 12 – Logarithm of the kinetic energy K_{per} of the perturbation for the simulation of figure 11 (normalized by initial total kinetic energy) for mode $k = 1$ in x (thick line) and sum of the modes $k > 1$ (dashed line), as a function of time. Left and right panels correspond to Fig. 10 and Fig. 11, respectively.

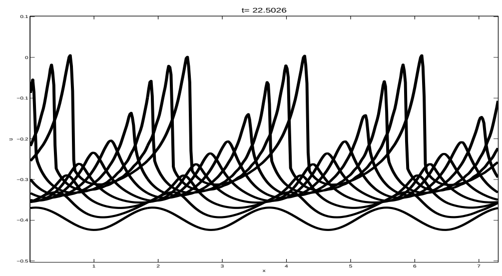

FIG. 13 – Evolution of the tangent (zonal) velocity of the flow at $y = -L$ (at the wall) for $t = 0, 2.5, 5, 7.5, 10, 12.5, 15, 17.5, 20, 22.5$ (from lower to upper curves)

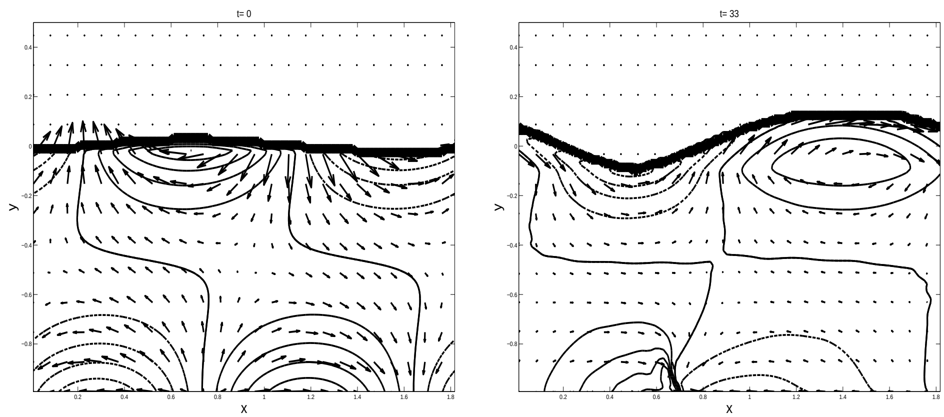

FIG. 14 – Height and velocity fields of the perturbation at $t = 0$ (left) and $t = 30$ (right). Kelvin front is clearly seen at the bottom of the right panel.

frontal and a Kelvin wave. It is known that Kelvin waves have a tendency to steepen, and to ultimately break (Bennett (1973)) forming Kelvin fronts (Fedorov & Melville (1995)). As usual (cf Bouchut *et al.* (2005)), the breaking process should enhance dissipation at the breaking location and, thus, contribute to the viscous saturation of the instability. Indeed, as shown in figure 13 where the zonal velocity of the flow close to the wall is plotted at different times during the initial development of the unstable mode, the steepening of the Kelvin wave does take place and its location does correspond to the enhanced dissipation zone displayed in figure 10, which thus finds its explanation. A closer view of the structure of the unstable mode after 30 inertial periods is presented in figure 14 and confirms the breaking Kelvin wave scenario.

A recently discovered feature of the Kelvin fronts is associated secondary inertia-gravity wave (IGW) emission (Fedorov & Melville (2000), LeSommer *et al.* (2004)). [3] This emission is confirmed by our simulations, as is clear from the horizontal divergence and corresponding height perturbation fields presented in figure 15.

It should be noted that Kelvin wave breaking induces a) significant interaction between the wave field and the mean flow, and b) dissipation, yielding advective PV fluxes

[3] Although in the aforementioned papers it was the IGW emission by *equatorial* Kelvin waves which was observed and explained, the argument is easily transposable to coastal Kelvin waves.

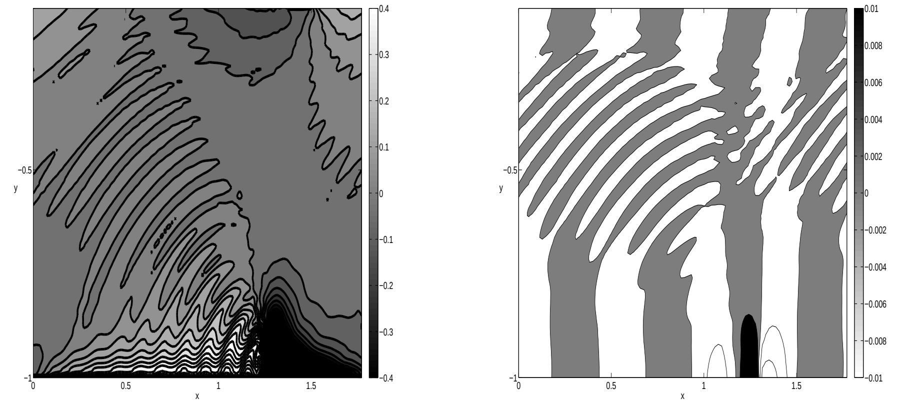

FIG. 15 – Horizontal divergence of the velocity field (left) and zonally filtered height field (right) at $t = 20$ for the simulation of figure 10.

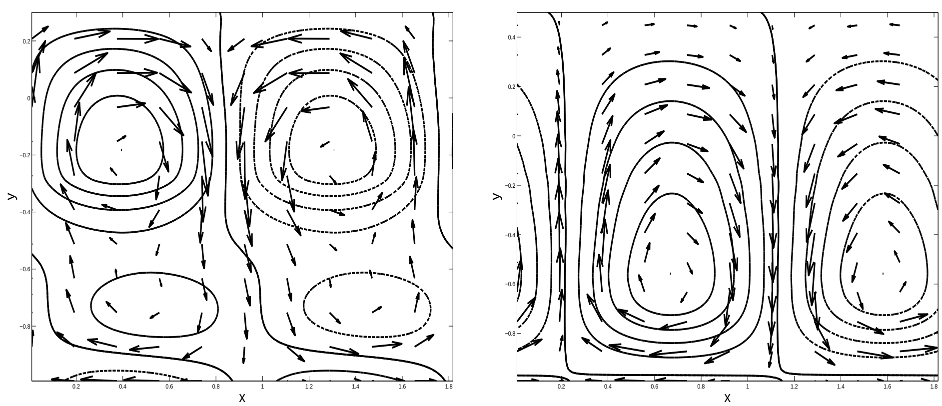

FIG. 16 – Height and velocity fields of the perturbation with $k = k_0$ at $t = 335$ (left) and $t = 500$ (right).

which modify irreversibly the PV distribution (cf LeSommer *et al.* (2004), Bouchut *et al.* (2005)). The amplitude of the mean zonal velocity is weakened at the wall, due to the steepening of the Kelvin mode and subsequent dissipation and wave-meanflow interactions thereafter. The mean flow is thus significantly modified and may give rise to new, secondary instabilities. This is what indeed happens.

As can be seen from the figure 12 (right panel), a second stage of the instability develops after some time, manifesting itself by a sharp rise of the energy of the perturbation. A $k = k_0$ mode develops with a maximal growth rate $\sigma \approx 0.05$. The structure of this mode (the velocity and the depth of the flow with the zonal mean being removed) is represented in figure 16 (left panel). We see a Rossby-like wave close to the wall which resonates with the (modified) frontal wave.

To understand this secondary instability, a linear stability analysis of the modified mean flow is needed. After the growth stage of the primary instability the mean zonal velocity of the flow is weakened close to the wall due to the breaking of the Kelvin mode,

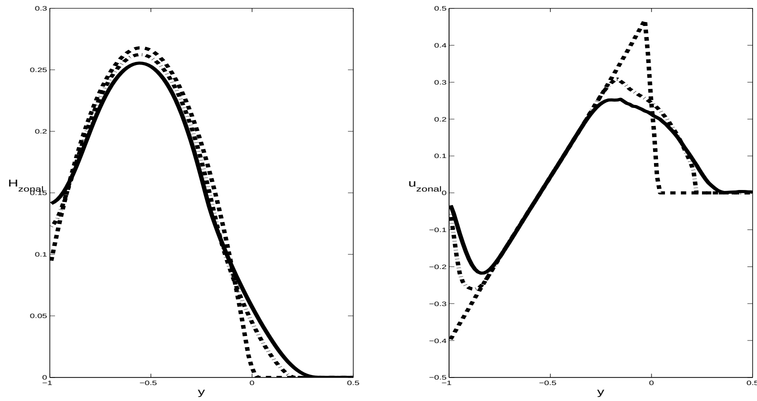

FIG. 17 – Evolution of the mean zonal height (left) and mean zonal velocity (right) for the simulation of figure 10 : Initial state $t = 0$ (dashed line), primary unstable mode saturated at $t = 40$ (dash-dotted line), late stage $t = 300$ (thick line).

and the front is spreaded due to the growth of the frontal mode, as shown in figure 17.

We thus consider the mean flow of figure 17 (thick line) as a new basic state, and repeat the linear stability analysis. The corresponding dispersion diagram and growth rates are presented in figure 18, and the structure of the most unstable eigenmode is displayed in figure 19, where we see that a frontal mode is now resonating with a Rossby-like mode in a larger than for the primary instability wavenumber range $0 < k < 4$. This instability is of the Rossby-Rossby type, if we follow classification of Sakai (1989).

A qualitative explaination of the modified stability properties of the flow may be given in terms of PV. The PV is no longer constant in the fluid layer, as a negative gradient of PV near the wall appears due to Kelvin wave breaking and related dissipation. If we also take into account the positive PV gradient due to the drying at the front, the Rayleigh-Kuo criterion, namely that the horizontal PV gradient has to change sign for instability to occur, will then be satisfied by the flow. To support this reasoning, we present the evolution of the PV field in figure 20.

As follows from figure 18, the growth rate of the secondary instability for the wavenumber $k = k_0 = 3.44$ is $\sigma = 0.056$ which fits quite well the growth rate observed during the simulation, see figure 12. Note that it does not correspond to the largest possible growth rate of this instability which would be obtained for $k = 2.5$, because the periodic zonal condition of the numerical experiment does not allow for wavenumbers less than $k_0 = 3.44$. The instability then saturates via unstable Rossby-type breaking, as can be seen in figure 11 at $t \approx 350$. The flow reaches a new state of equilibrium after this stage, see panel (d) of figure 11, with anticyclonic vortex meanders. The corresponding filtered field (cf. figure 16) shows a Rossby wave slowly propagating with the mean flow.

The total energy loss during the whole simulation is about 20% of the total initial energy, as shown in figure 21. It is non-negligible but stays quite acceptable compared to rather long duration ($t = 500f^{-1}$) of the simulation. In the numerical scheme we are using, the numerical dissipation acts only in the zones of high gradients. The events of enhanced dissipation take place during the two stages of instability at the time of Kelvin and Rossby wave breaking, which is consistent with what was stated earlier. The slow monotonic decrease of energy during the whole simulation is explained by the fact that

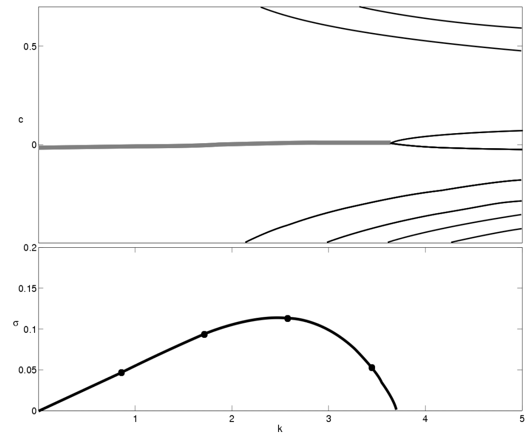

FIG. 18 – Dispersion diagram of the eigenmodes corresponding to the basic state profile of the flow at $t = 335$, at the beginning of the secondary instability stage (see Fig. 17).

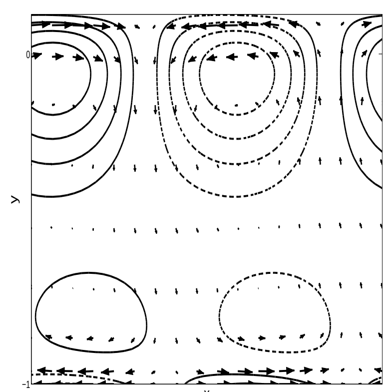

FIG. 19 – Height and velocity fields of the most unstable mode of figure 18 for $k = k_0$. Only one wavelenght is plotted. Note the similarity with the mode observed in the simulation, Fig. 16

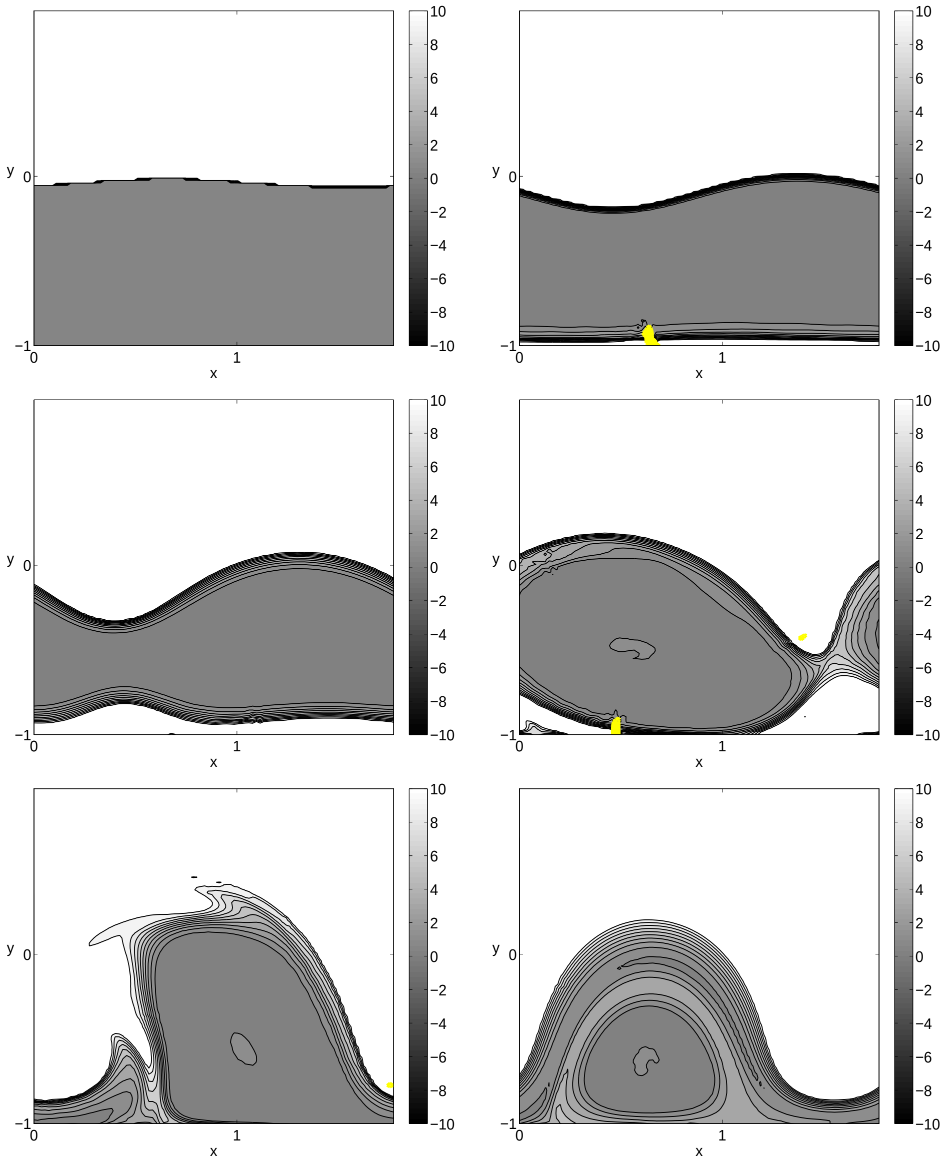

FIG. 20 – PV field corresponding to the simulation of of Figs. 10, 11 at $t = 0, 30, 200, 335, 350, 500$. Contours at interval 1.

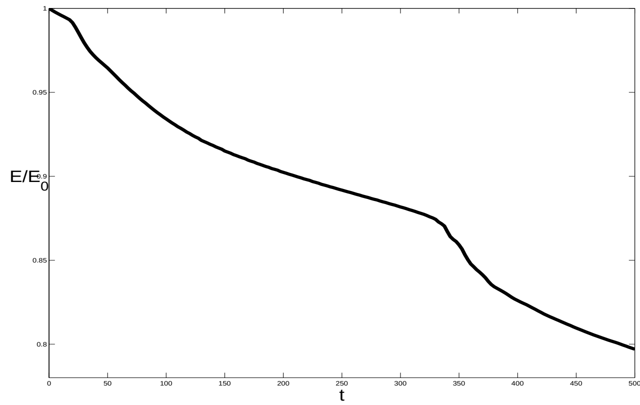

FIG. 21 – Time evolution of the total energy normalized by the initial energy for the evolution of the primary instability. The events of stronger decrease correspond to the events of Kelvin and Rossby wave breaking.

it is easy to generate micro shocks in the shallow regions of the fluid in the drying zone.

Non-linear evolution of the most unstable mode : the role of boundary conditions

As we have seen in the previous subsection, the choice of the along-current boundary condition does affect the nonlinear evolution of the instability at the second stage by selecting a specific unstable mode of the mean flow modified by the primary instability. In order to investigate the sensibility of the nonlinear evolution scenario to this effect, we performed the same simulation with quadrupled spatial period. This means that development of perturbations with wavelength up to 4 times longer than the wavelength of the most unstable mode was allowed. The corresponding evolution of the height field in the (x, y)-plane is shown in figure 22. The evolution of the kinetic energies of the perturbation modes with $k = k_0,\ 0.75\ k_0$ and $0.5\ k_0$ are plotted in figure 23.

One can see that the primary instability develops in the same way as in the previous simulation for $0 < t < 30$. The $k = k_0$ mode grows with a growth rate $\sigma \approx 0.06$, as expected from the linear stability analysis until the breaking event of the Kelvin mode. But then the evolution of the flow differs, as we now allow for modes with lower wavenumbers $k = 0.75k_0, 0.5k_0$ and $0.25k_0$ to develop. The evolution of the kinetic energy for each of these modes (figure 23) shows that they grow at the second stage of the instability with the growth rates $\sigma \approx 0.05,\ 0.09,\ 0.07$, and 0.04 for $k = k_0,\ 0.75k_0,\ 0.5k_0$ and $0.25k_0$, respectively. These are to be compared with the growth rates of the stability analysis of figure 18, which gives $\sigma = 0.05,\ 0.1,\ 0.085$, and 0.04 respectively. This means that, again, it is just the linearly unstable reorganized mean flow which is at the origin of secondary growing modes, and not e.g. the parametric instability of the primary unstable mode.

The filtered velocity and height fields of the secondary growing modes as given by the direct simulation are presented in figure 24. They are in a very good agreement with the corresponding eigenmodes computed from the linear stability analysis which are plotted in figure 25 for the same wavenumbers, thus comforting the interpretation of the secondary growing modes as linearly unstable modes on the background of the

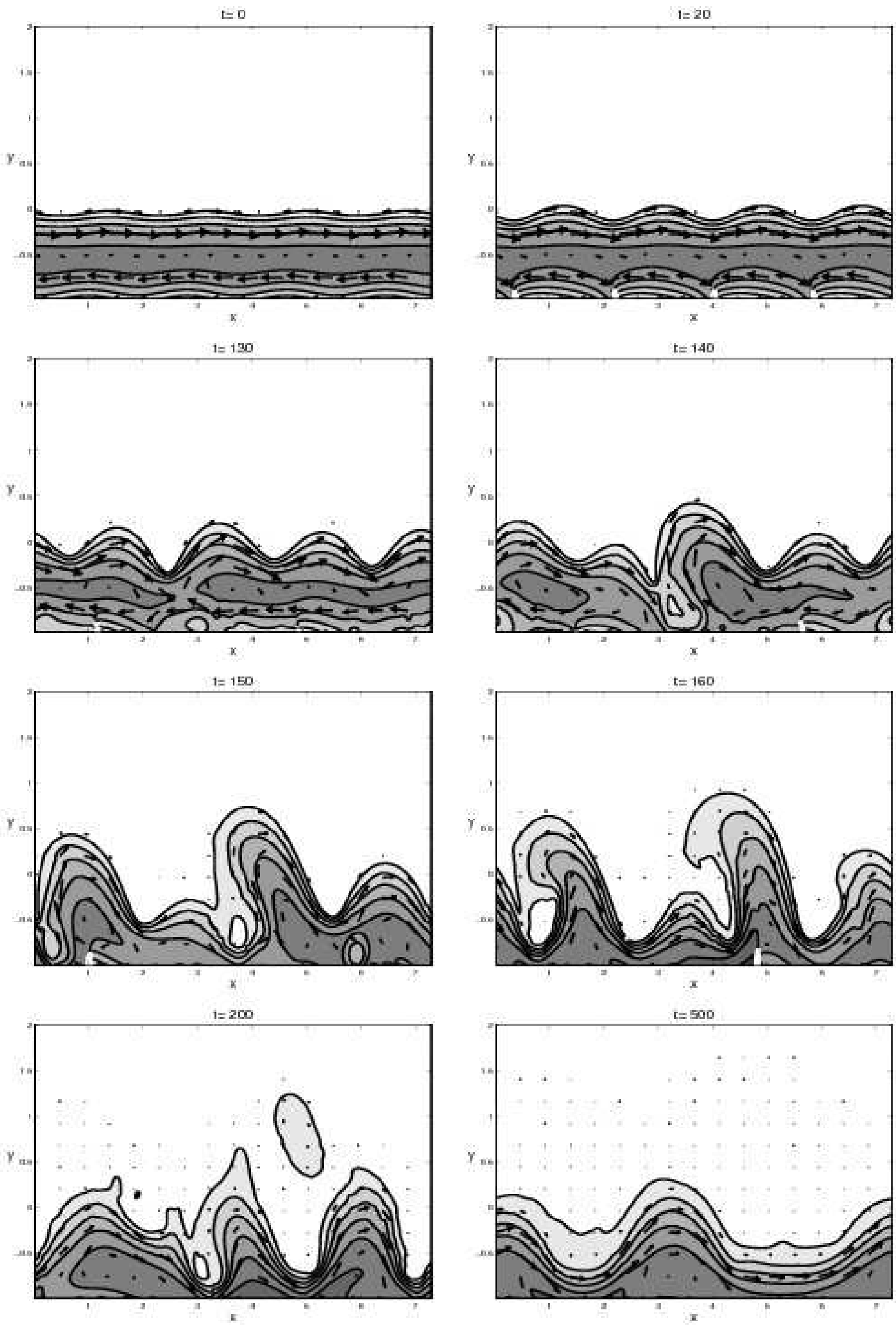

FIG. 22 – Levels of $h(x, y, t)$ are shown at $t = 0, 20, 130, 140, 150, 160, 200$ and 500 for the development of the most unstable mode of figure 8 corresponding to the basic flow with constant PV as defined by (6.2.2). Contours displayed are 0.01, 0.05, and further on at the interval 0.05. The arrows indicate the mass flux $h\vec{v}$. The initial amplitude of the perturbation is 10% of the maximum depth of the balanced flow. The calculation domain is periodic in the x-direction and corresponds to 4 wavelenghts of the most unstable mode. White area superimposed on the isolines of the height field corresponds to spatial distribution of the dissipation rate between 0.005 and 0.05 (the maximum value).

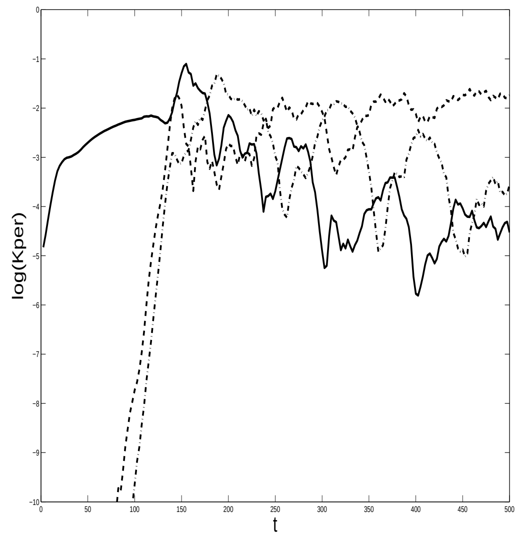

FIG. 23 – Logarithm of the kinetic energy K_{per} (normalized by initial total kinetic energy) of the most energetic perturbation modes $k = k_0$ in x (thick line), $k = 0.75\ k_0$ (dashed line), and $k = 0.5\ k_0$ (dash-dotted line) as a function of time for the simulation of figure 22.

mean flow modified by the development of the primary instability.

As to the nonlinear stage of the secondary instability, the presence of several growing modes with comparable growth rates leads to spatial modulation of the breaking Rossby-wave patterns, as can be seen in figure 22.

Similar simulations have been performed for other sizes of the zonal domain giving results that support the same interpretation.

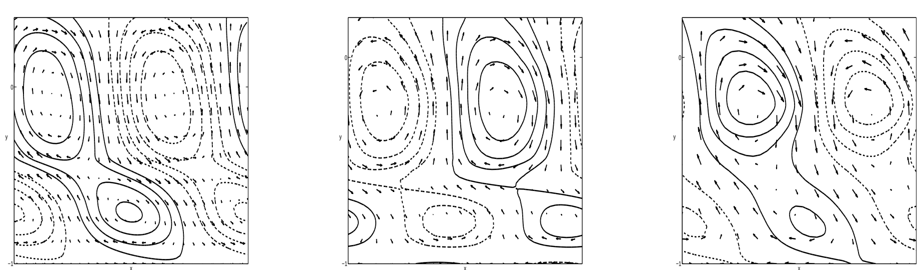

FIG. 24 – Height and velocity fields for the secondary unstable modes with wavenumbers (a) $k = 0.5\ k_0$, (b) $k = 0.75\ k_0$ and (c) $k = k_0$ for the simulation of figure 22 at $t = 140$.

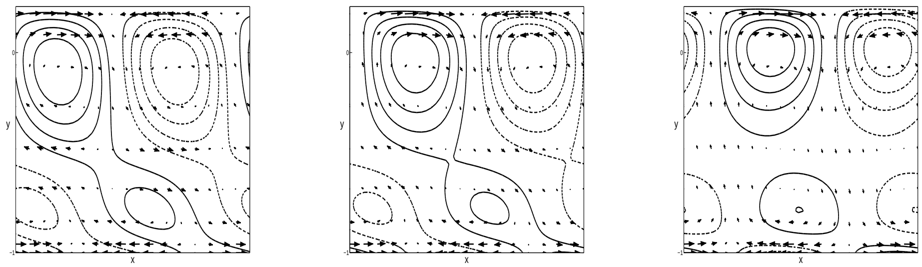

FIG. 25 – Height and velocity fields of the unstable modes with wavenumbers (a) $k = 0.5\ k_0$, (b) $k = 0.75\ k_0$ and (c) $k = k_0$ computed from the linear stability analysis of the reorganized mean flow (see figure 18).

Manifestations of the instability in the initial-value problems

In the preceding subsections we deliberately initialized nonlinear simulations by superposing the most unstable spatially periodic mode onto the basic flow. A question, however, arises, what is the role of the instability in the evolution of the localized initial perturbations of the basic flow ?

In this (more realistic) context Stern (1980) studied finite-amplitude perturbations of a coastal current with zero PV and found several classes of perturbations which could steepen with time or block the transport in the current. Paldor (1988) used asymptotic expansion techniques to study perturbations and found the existence of solitary and cnoidal waves, governed by the Korteweg-de Vries equation. Dahl (2005) investigated perturbations of arbitrary initial shape of a constant PV current and found that the initial perturbation gives rise mainly to the two distinguished wave modes, the Kelvin wave and the frontal wave, while the rest of the perturbation is advected and slowly smeared out by the current.

To answer this question we have chosen a localized initial perturbation of the form :

$$h(x, y) = Ae^{(-x/L_p)^2}, \tag{13}$$

with a smooth regularization in y at the front location $y = 0$, and superposed it first on the *stable* basic flow with zero zonal velocity at the wall, and with dispersion diagram of figure 6. The corresponding evolution of the height field in the (x, y)-plane is shown in figure 26.

The x-coordinate has been rescaled (divided by time $t = 45$) in order to give the Doppler-shifted phase velocity of the different waves excited by the perturbation. One can verify that the perturbation excites mainly the two type of waves described in the previous sections, the faster one with its maximum at the coast beeing a Kelvin wave, and the slower one with its maximum at the front being a frontal wave. The comparison of the dispersion relation of these waves as deduced from figure 26, which provides both the phase speed and the corresponding wavelength, with that following from the figure 6 shows that our interpretation is consistent. We thus recover weakly dispersive Kelvin waves with $0.65 < c < 0.75$, the maximum of their amplitude propagating in the direction of the current with the characteristic Kelvin wave speed $c \approx \sqrt{g'H(-L)}$. The frontal waves have a greater dispersion $0 < c < 0.5$, the first mode beeing almost stationary, while higher modes propagate in the direction of the current. In this simulation with a stable basic flow the two families of waves just propagate at different velocities,

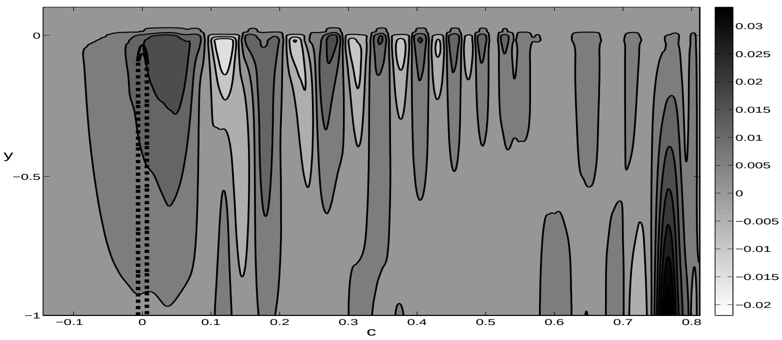

FIG. 26 – Levels of $h(x, y, t)$ at $t = 45$ for the evolution of a localized initial perturbation (dashed black line) imposed on a linearly stable basic state. The initial amplitude of the perturbation A is 0.05 and the width of the perturbation is $L_p = 0.5$.

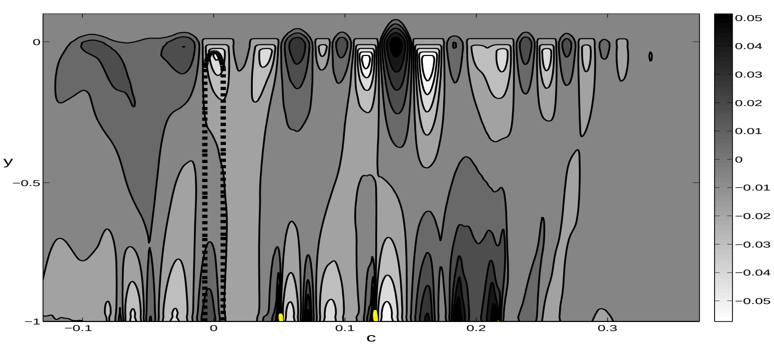

FIG. 27 – Same as in figure 26, but for a linearly unstable basic state, and with a rescaling in x in order to zoom into developping instability.

one at the coast, one at the density front, without 'feeling' each other.

We then imposed the same initial perturbation on a *linearly unstable* flow with a return current at the coast. The frontal and the Kelvin waves are excited similarly by the perturbation but now, consistently with the resonance interpretation of the instability, their Doppler-shifted phase velocities are close. Figure 27 shows the perturbation height for such flow after $t = 45$. From this simulation we extract the phase speed of the frontal waves to be from $c \approx -0.1$ for low k to $c \approx 0.3$ for greater k, and the Kelvin waves phase speed from $c \approx 0.2$ for low k to $c \approx -0.1$ for greater k. These results fit well the linear analysis of figure 7. As repeatedly stated before, the unstable character of the flow is due to the resonance between these two types of waves corresponding to a crossing between the two respective disperion curves, i.e. close phase speeds in some range of wavenumbers. Such phase-locking is clearly visible in figure 27, the two types of waves having close wavenumbers and phase speeds in the domain $0.1 < c < 0.18$. Consistently, the amplitude of the perturbation height is growing in this area being, roughly, twice higher than in the stable situation of figure 26 for $0.1 \leq c \leq 0.3$.

6.2.4 Summary and concluding remarks

Linear instabilities of the coastal buoyancy-driven currents and their fully nonlinear evolution have been studied within the reduced-gravity rotating shallow-water model. By using the collocation method, we benchmarked the classical linear stability results on zero PV fronts, and generalized them to non-zero PV fronts. In both cases, we found instabilities due to the resonance of frontal and coastal Kelvin waves trapped in the current, and identified the most unstable long-wave mode.

We then studied the nonlinear evolution of the unstable modes with the help of a high-resolution well-balanced finite-volume numerical scheme for shallow-water equations. The simulations have been initialized both with the unstable modes obtained from the linear stability analysis and with localized perturbations. We found that the most unstable mode is growing to finite amplitude, and then saturates leading to a reorganization of the mean flow, and hence of the PV field. The saturation of the primary instability is due to the breaking of its Kelvin-wave component, formation of Kelvin fronts with enhanced dissipation, and emission of short-scale inertia-gravity waves

A linear stability analysis of thus modified mean flow, shows that it is unstable to a secondary instability, of the type of the classical barotropic instability due to change of sign of the gradient of PV within the current. This scenario is verified in the direct numerical simulations showing that after the saturation of the first instability, the secondary instability leads to growth and ultimate breaking of the unstable Rossby-type mode, leading to the formation of coherent balanced vortex structures.

For a coastal current, the lower layer can rarely be considered dynamically inactive. The coupling between the two layers is likely to allow for different types of baroclinic interactions that were forbidden in the reduced gravity model to appear. The barotropic instability discussed in the previous sections, and subsequent finite amplitude development of the flow will also be modified by the presence of an active lower layer. For example, upper layer anticyclones which form in the final state of the reduced gravity simulations could couple with lower layer cyclones and propagate away from the coast. We address these questions in Part II of the present study, which is the subject of the companion paper (Gula *et al.* (2009*b*)).

6.3 De la gravité réduite au modèle deux couches

L'analyse de stabilité linéaire d'un courant côtier pour différents profils de hauteur et de vitesse a donc confirmé les résultats de Killworth & Stern (1982), Kubokawa & Hanawa (1984) et Kubokawa (1986) pour des écoulements avec une vorticité potentielle nulle, et étendu leur validité à des écoulements avec différentes distributions de vorticité potentielle. Cet écoulement peut donc devenir instable lorsque les modes côtiers (Kelvin et Poincaré) vont résonner barotropiquement avec les modes qui se propagent le long du front (frontal et Poincaré). Le mode le plus instable étant systématiquement l'interaction du mode de Kelvin et du mode frontal.

L'évolution non-linéaire de ces écoulements a ensuite été simulée à l'aide du code numérique en volume fini dans sa version une couche. Les simulations sont initialisées soit avec les modes instables issus de l'analyse de stabilité linéaire, soit avec une perturbation de hauteur localisée. Dans les deux cas les résultats sont similaires, à savoir la croissance du mode le plus instable à amplitude finie, puis la saturation de ce mode et enfin la réorganisation de l'écoulement moyen et du champs de vorticité potentielle. La saturation de l'instabilité primaire (KF) étant due au déferlement de l'onde de Kelvin se propageant le long de la côte, qui provoque l'apparition d'un front de Kelvin ainsi qu'une émission d'ondes d'inertie-gravité de petite échelle.

Une nouvelle analyse de stabilité linéaire de l'écoulement moyen ainsi modifiée par la saturation de l'instabilité primaire, montre que celui-ci est susceptible de développer une instabilité secondaire, une instabilité barotrope classique due à l'apparition d'un changement de signe du gradient de vorticité potentielle dans l'écoulement (voir critère de Rayleigh-Kuo dans la partie 2.5). Ce scénario est confirmé par les simulations qui montrent que cette instabilité secondaire va à son tour croître et déferler jusqu'à la formation de vortex équilibrés.

Mais pour les courants côtiers comme étudiés ici, la couche de fluide inférieure ne peut généralement être considérée comme inactive, ce qui était le cas dans le modèle à gravité réduite. Le couplage entre les deux couches et les différentes interactions baroclines sont alors susceptibles de modifier le scénario précédent. On peut par exemple supposer que les vortex anticycloniques qui se forment dans la couche supérieure sont susceptibles de se coupler avec des cyclones dans la couche inférieure et ainsi se propager vers le large. Nous allons donc maintenant nous intéresser à ces interactions baroclines dans la partie 6.4 dans le cadre d'une étude similaire à l'étude précédente, mais pour un modèle à deux couches.

6.4 *Instabilities of buoyancy driven coastal currents and their non-linear evolution in the two-layer rotating shallow water model. Part II. Active lower layer*

Les expériences de Griffiths & Linden (1981, 1982) et Chia *et al.* (1982) ont étudié des situations d'outcropping dans des fluides en rotation à deux couches, pour des configurations de type courant côtier (voir figure 6.28 (a)) ou de type "upwelling" (voir figure 6.28 (b)). Ils ont montré dans les deux situations que le courant était instable pour de grandes longueurs d'ondes suivant un mécanisme barocline identique.

Ce mécanisme a été confirmé par Killworth *et al.* (1984) qui a étudié les instabilités linéaires pour un front isolé (loin d'un bord) avec une couche inférieure active et par Kubokawa (1988) dans le cas d'un courant côtier, qui ont montré que cette configuration était instable. Cette instabilité est due à l'interaction barocline entre le mode frontal

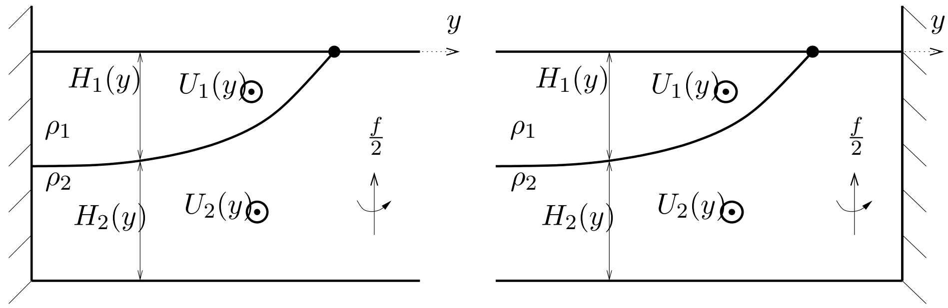

FIG. 6.28 – Configurations dans le modèle 2 couches pour (a) un courant côtier, (b) un courant de type upwelling.

présent dans la couche supérieure et des ondes de Rossby dans la couche inférieure, avec des taux de croissance plus importants lorsque la hauteur de la couche inférieure diminue. Les modes de Poincaré étant présents dans tous les types de configurations, les possibilités de résonances pour ces modes entre les deux couches (instabilité KH) sont aussi présentes, de même que la résonance entre modes de Poincaré dans la couche inférieure et le mode frontal pour de très grands nombres d'ondes (étant donné que le mode frontal a une structure de type onde de gravité à très grand nombre d'onde). Paldor & Ghil (1991) ont ainsi étudié ces instabilités de petite échelle dans le cas d'un courant côtier et montré qu'elles avaient des taux de croissances plus importants à mesure que les nombres d'ondes augmentaient et que la hauteur de la couche inférieure devenait faible.

L'instabilité barocline est retrouvée dans différentes études pour des cas d'upwelling comme Barth (1989a,b), qui a utilisé un modèle en eau peu profonde à deux couches mais en faisant l'approximation du moment géostrophique, et qui a aussi retrouvé une instabilité de plus petite échelle similaire à celle étudiée par Killworth (1983a) correspondant à une interaction du mode frontal avec les niveaux critiques. Lee & Csanady (1994) ont réalisé une étude similaire dans un modèle à trois couches et étudié les instabilités baroclines en montrant que la présence d'un bord vertical proche du front, dans le cas d'un upwelling, avait pour effet de stabiliser l'écoulement. Les résultats de Barth (1989a,b) ont été complétés par Haza *et al.* (2004), toujours dans le cas d'un modèle en eau peu profonde à deux couches et un upwelling, qui ont aussi montré que lorsque la couche inférieure avait une épaisseur assez faible des instabilités de petite échelle apparaissaient de manière similaire aux mécanismes étudiés dans Paldor & Ghil (1991).

Beaucoup d'études des instabilités de courants côtiers ont donc été réalisées dans le cadre de l'approximation quasi-géostrophique comme Ikeda (1983); Smeed (1988a,b) ou plus récemment Capet *et al.* (2002) et Capet & Carton (2004) qui ont travaillé dans un cadre quasi-géostrophique où les deux couches sont constituées d'une bande de vorticité potentielle constante à l'aide d'un modèle lagrangien de contour de vorticité potentielle. Dans le cas où le critère d'instabilité de Charney-Stern (voir partie 2.5) est satisfait, c'est-à-dire lorsque les deux couches possèdent un gradient de vorticité potentielle opposé, l'écoulement est instable et conduit à la formation et au détachement de vortex. La taille de ces vortex est liée à deux paramètres qui sont le transport et la largeur des deux couches. Citons enfin plusieurs études dans des modèles incorporant une stratification ou un gradient horizontal de température comme McCreary *et al.* (1991); Barth (1994); Fukamachi *et al.* (1995); Young & Chen (1995); Shi & Roed (1999).

Les résultats sur l'instabilité et l'évolution nonlinéaire des courants côtiers dans le modèle à deux couches font l'objet d'un article soumis à *Journal of Fluid Mechanics* (Gula *et al.* (2009*b*)). Ainsi nous les incluons en anglais.

Instabilities of buoyancy driven coastal currents and their nonlinear evolution in the two-layer rotating shallow water model. Part II. Active lower layer

J. Gula, V. Zeitlin[4] & F. Bouchut[5]

The present paper is the second part of the work on linear and nonlinear stability of buoyancy-driven coastal currents. Part I was presented in the companion paper Gula & Zeitlin (2009). In this part we use a fully baroclinic 2-layer model, with active lower layer. We revisit the linear stability problem for coastal currents and study nonlinear evolution of the instabilities with the help of high-resolution DNS. We show how nonlinear saturation of the ageostrophic instabilities leads to reorganization of the mean flow and emergence of coherent vortices. We follow the same lines as in Part I and, first, perform a complete linear stability analysis of the baroclinic coastal currents for various depths and density ratios. We then study the nonlinear evolution of the unstable modes with the help of the recent efficient two-layer generalization of the one-layer well-balanced finite-volume scheme for rotating shallow water equations, which allows to treat outcropping and loss of hyperbolicity associated to Kelvin-Helmholtz (KH) instabilities. The previous single-layer results are recovered in the limit of large depth ratios. For depth ratios of order one new baroclinic long-wave instabilities come into play due to the resonances among vortical (Rossby-like) and frontal or coastal trapped waves. These instabilities saturate by forming coherent baroclinic vortices, and lead to a complete reorganization of the initial current. For even smaller depth ratios short-wave instabilities of KH type with large growth rates develop shortly. We show that at nonlinear stage they produce rapidly growing short-wave meanders with enhanced dissipation. However, they do not change, globally, the structure of the mean-flow which undergoes secondary large-scale instabilities leading to coherent vortex formation and cut-off.

6.4.1 Introduction

In the companion paper Gula & Zeitlin (2009), which hereafter will be referred as Part I, we undertook a detailed analysis of the instabilitis of the buoyancy-driven coastal currents (BDCC in what follows) in the framework of the reduced-gravity one-layer rotating shallow water model. We have explained the leading linear instability in terms of resonance between Kelvin wave trapped at the coast, and so called frontal (Rossby-type) wave trapped at the density front, where the current terminates. By initializing the high-resolution DNS with the most unstable mode we were able to identify the saturation mechanism of the instability via the Kelvin wave breaking and reorganization of the mean flow which, in turn, leads to secondary instability saturating via frontal wave breaking and formation of coherent vortex structures.

As was already discussed in Part I, the simple and physically transparent one-layer reduced gravity model neglects the interactions between the upper layer, where evolves the BDCC, and the lower layer, which is assumed to be completely passive, i.e. infinitely thick. As it was also mentioned, the baroclinic effects, arising if the lower layer

[4]Laboratoire de Météorologie Dynamique, ENS,
24, rue Lhomond, 75231 Paris Cedex 05, France

[5]Département de Mathématiques et Applications, ENS,
45 rue d'Ulm, 75230 Paris, France

is activated, bring in completely new phenomena related to the interaction of waves propagating in the upper and lower layers. The goal of the present paper is, precisely, to study how these new phenomena influence linear and nonlinear stages of instability of BDCC. We will be globally following the lines of Part I, by undertaking first an exhaustive linear stability analysis with the help of the collocation method, and then by studying the nonlinear evolution of the developing instability with the help of the high-resolution DNS using a new finite-volume two-layer shallow water scheme (Bouchut & Zeitlin (2009)). It should be stressed that while there is no principal difference in what concerns the collocation approach between the linear stability analysis in the one-layer and two-layer cases, although calculations become much more cumbersome due to the increased number of dynamical variables for two layers, the difficulty of nonlinear simulations is qualitatively new, as the two-layer system, unlike the one-layer one, is of the mixed type and loses hyperbolicity for strong enough shear between the layers (e.g. LeSommer *et al.* (2003)).

In what follows we will insist on the new elements brought by the presence of the active lower layer, without dwelling into phenomena already discussed in Part I. Although the lower layer is active, we will limit ourselves by configurations where the mean velocity of the lower layer is always zero in linear stability analysis, or is initially zero in DNS. Obviously (and this will be a primary consistency check below), the "barotropic" reduced gravity results of Part I should be reproduced in the limit of very large thickness of the lower layer. We will be discussing mainly two different configurations : the case of barotropically (in the previous sense) stable, and the case of barotropically unstable current in the upper layer. In the first case all instabilities are purely baroclinic, while in the second case instabilities of baroclinic origin will be admixed to the leading barotropic instability.

6.4.2 The 2-layer rotating shallow water model and the linear stability problem

In this section we first remind the two-layer rotating shallow water model and its linearized version, and introduce the key parameters (section 6.4.2). We then display the results of the linear stability analysis by the collocation method : the instabilities, their growth rates and the structure of the unstable modes for a barotropically stable flow (section 6.4.2), and for a barotropically unstable flow (section 6.4.2).

The overview of the model

We consider the two-layer BDCC configuration presented in figure 29. It consists of an upper layer of lighter fluid of density ρ_1 with a free surface terminating at some point (a density front), and a mean steady velocity $U_1(y)$, and a lower layer of density $\rho_2 > \rho_1$ with a mean steady velocity $U_2(y)$. In the examples treated below $U_2(y)$ will be taken to be zero. The equations of two-layer rotating shallow water are

$$\begin{array}{rcl} D_j u_j - f v_j & = & -\frac{1}{\rho_j}\partial_x \pi_j, \\ D_j v_j + f u_j & = & -\frac{1}{\rho_j}\partial_y \pi_j, \\ D_j h_j + \nabla\cdot(h_j \mathbf{v_j}) & = & 0, \end{array} \qquad (1)$$

where the index $j = 1, 2$ denotes the upper and the lower layers, respectively, (x, y) and $\mathbf{v_j} = (u_j, v_j)$ are the zonal and meridional coordinates and velocity components, $h_j(x, y, t)$ are the depths of the layers, π_j, ρ_j are the pressures and the densities of the layers, $D_j = \partial_t + u_j\partial_x + v_j\partial_y$ is the Lagrangian derivative, and f is the constant Coriolis

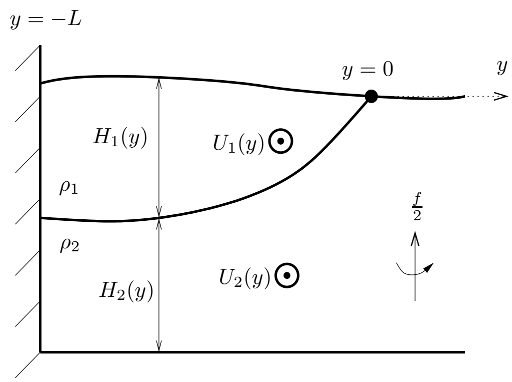

FIG. 29 – Schematic representation of a buoyancy driven coastal current in the two-layer model.

parameter. The pressures in the upper and lower layers are related to layers' depths via the hydrostatic balance relations.

We linearize these equations about the steady geostrophically balanced state with the depth profiles $H_j(y)$, and corresponding velocities $U_j(y)$:

$$\partial_y H_j = (-1)^{j-1} \frac{f}{g'} (U_2 - s^{j-1} U_1), \tag{2}$$

where $s = \rho_1/\rho_2$ is the stratification parameter and $g' = (1-s)g$ the reduced gravity. The linearized equations, where u_j, v_j and h_j are the perturbations to the basic state fields, are :

$$\begin{aligned} \partial_t u_j + U_j \partial_x u_j + v_j \partial_y U_j - f v_j &= -g\, \partial_x (s^{j-1} h_1 + h_2), \\ \partial_t v_j + U_j \partial_x v_j + f u_j &= -g\, \partial_y (s^{j-1} h_1 + h_2), \\ \partial_t h_j + U_j \partial_x h_j + H_j \partial_x u_j &= -\partial_y (H_j v_j), \end{aligned} \tag{3}$$

where we used that

$$\nabla \pi_j = \rho_j g \nabla (s^{j-1} h_1 + h_2). \tag{4}$$

In order to compare our results with those of the reduced gravity configuration of Part I, the setting and the non-dimensionalization are chosen in the same way. We introduce the time scale f^{-1}, the horizontal scale L, which is the unperturbed width of the current, the velocity scale fL and the vertical scale $(fL)^2/g'$. We will use only non-dimensional variables from now on without changing notation. The linearized equations thus are :

$$\begin{aligned} \partial_t u_j + U_j \partial_x u_j + v_j \partial_y U_j - v_j &= -\partial_x (s^{j-1} h_1 + h_2), \\ \partial_t v_j + U_j \partial_x v_j + u_j &= -\partial_y (s^{j-1} h_1 + h_2), \\ \partial_t h_j + U_j \partial_x h_j + H_j \partial_x u_j &= -\partial_y (H_j v_j). \end{aligned} \tag{5}$$

The important parameters in what follows are U_0, the non-dimensional velocity of the upper layer at the front location ($y = 0$), which is in fact equivalent to a Rossby number, the depth ratio $r = H_1(-1)/H_2(-1)$ and the density ratio $s = \rho_1/\rho_2$.

The boundary condition of no normal flow at the wall is the same as in the 1-layer case for both layers, $v_j(-1) = 0$.

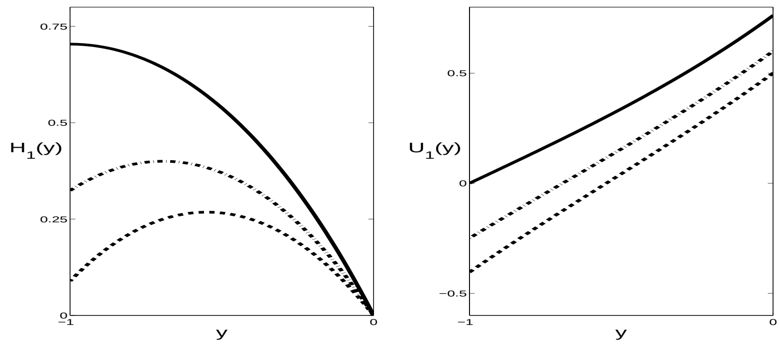

FIG. 30 – Examples of basic state depths (left) and velocities (right) for a constant PV flow in the upper layer with $U_0 = -sinh(-1)/cosh(-1)$ (thick line), and $U_0 = 1/2$ (dotted line), and a zero-PV flow (dash-dotted line).

The boundary condition at the front for the upper layer is also the same as in the 1-layer case, because the only constraint to be imposed is the regularity of $(u_1, v_1, h_1 + h_2)$ at $y = 0$.

For solutions harmonic in the x-direction

$$(u_j(x,y), v_j(x,y), h_j(x,y)) = (\tilde{u}_j(y), \tilde{v}_j(y), \tilde{h}_j(y))\ exp\left[i(kx - \omega t)\right], \tag{6}$$

π_2 satisfies the equation $\partial_{yy}\pi_2 = k^2\pi_2$ in the half plane $y > 0$ with no upper layer. Hence the solution which decays away from the free streamline as $y \to \infty$ has to satisfy the equation $\partial_y\pi_2 = -k\pi_2$ (we exclude fom our analysis the modes coupled to free gravity waves far from the front). In order for the solution of π_2 in the region $y < 0$ to match continuously the decaying solution for $y > 0$ we require that the two are identical at $y = 0$. Thus the boundary conditions at the front for the lower layer give (see Paldor & Killworth (1987) for details) :

$$\partial_y(sh_1 + h_2) = -k(sh_1 + h_2) \text{ at } y = 0.$$

Assuming (6) we obtain an eigenvalue problem of order 6 which can be solved by applying the spectral collocation method as described in Trefethen (2000) and Poulin & Flierl (2003) along the same lines as in Part I.

In the following, we will consider a bottom layer initially at rest ($U_2 = 0$) and an upper flow with constant PV. The constant PV in the upper flow corresponds to the solution of the equation $1 + H_{1yy} - Q_1 H_1 = 0$, which gives :

$$\begin{aligned}
U_1(y) &= U_0 cosh(\frac{y}{R_d}) + R_d sinh(\frac{y}{R_d}), && (7)\\
H_1(y) &= -\frac{1}{Q_1}\left[1 - \frac{U_0}{R_d} sinh(\frac{y}{R_d}) - cosh(\frac{y}{R_d})\right], && (8)\\
H_2(y) &= (r+s)H_1(-1) - sH_1(y)\ , && (9)
\end{aligned}$$

where Q_1 is the constant potential vorticity of the mean flow in the upper layer, U_0 is the current velocity of the upper layer at the front ($y = 0$) and $R_d = \sqrt{\frac{1}{Q_1}}$ (cf Part I).

Note that this basic state is always unstable, according to Ripa's criterion (Ripa (1991)), which states that sufficient conditions for stability are :

$$\exists\alpha/\ \forall y \begin{cases} (U_j-\alpha)\frac{dQ_j}{dy} \leq 0 \ \ (j=1,2), \\ \frac{(U_1-\alpha)^2}{H_1} + \frac{(U_2-\alpha)^2}{H_2} \leq g'. \end{cases} \tag{10}$$

Indeed, an inspection of (10) shows that :

– The first condition is always satisfied for the upper layer as $Q_1 = cste$.

– The first condition for the lower layer gives $\frac{\alpha U_1}{H_2^2} \leq 0$ which could be satisfied only for $[\alpha = 0]$ or $[\alpha \leq 0$ and $U_1(y) \geq 0]$ or $[\alpha \geq 0$ and $U_1(y) \leq 0]$, considering that H_2 stays finite.

– Due to the front at $y = 0$ ($H_1(0) = 0$), the second condition can be satisfied only for $\alpha = U_1(0)$, which is not compatible with previous conditions. Hence, it is impossible to satisfy both criteria for this basic state, except in the limit $H_2 \to +\infty$ where we recover the one-layer condition for instability (cf Part I).

Instabilities and resonances between the eigenmodes

As in the one-layer configuration of Part I, the instabilities of the BDCC in the two-layer case originate from resonances between the eigenmodes of the linearized problem (crossing of dispersion curves for different types of waves, cf Cairns (1979)). The wave species of the rotating shallow-water models are Poincaré (inertia-gravity) modes, Rossby modes (if PV gradients are present) and, in the bounded domains, unidirectional Kelvin modes trapped at the boundary, and frontal modes trapped in the vicinity of the free streamlines (outcropping/incropping lines). [6]

For the two-layer BDCC configuration with constant PV in the upper layer, which is the subject of the present work, we thus have Poincaré and Kelvin waves in both layers, Rossby waves in the lower layer, as the PV is not held constant in the lower layer, and a frontal wave in the upper layer. The instabilities which have been discussed previously in the literature for this configuration are related to the following resonances : (a) the barotropic resonance of a Kelvin or Poincaré mode and a frontal mode in the upper layer, which has already been discussed in the reduced-gravity model in Part I ; (b) the baroclinic resonance between a frontal mode in the upper layer and a Rossby mode in the lower layer (Killworth *et al.* (1984); Kubokawa (1988); Barth (1989*a*)), which is sometimes confused with the classical baroclinic instability, or is called mixed barotropic/baroclinic instability due to its energetics ; (c) high wavenumber resonances between a Poincaré wave in the lower layer and a frontal or Poincaré wave in the upper layer, all of them giving KH-type instabilities (Paldor & Ghil (1991)).

Other resonances are a priori also possible, but were not discussed in the literature in this context, to our knowledge : (a) the resonance between a Kelvin or Poincaré wave in the upper layer and a Rossby wave in the lower layer, which is usually called Rossby-Kelvin instability (RK) as discussed in (Sakai (1989); Gula *et al.* (2009*a*)) ; (b) the resonance between a Kelvin wave in the lower layer and the frontal wave in the upper layer, which would be similar to RK instability at low wavenumbers and to KH instability at high wavenumbers. We will demonstrate below that these resonances are indeed relevant.

[6] We do not discuss topographic effects here, which would significantly increase the variety of wave species, cf Leblond & Mysak (1978).

Two main configurations will be discussed in the following subsections. We will first study a barotropically stable basic state (stable in the reduced gravity model), and then a barotropically unstable basic state (unstable to frontal-Kelvin instability discussed in Part I). We will present an exhaustive linear stability analysis and identify the resonances leading to instabilities in both cases.

Unstable modes of a barotropically stable flow

We first consider a basic flow with zero velocity at the wall, cf. figure 30. This configuration corresponds to a flow with constant PV without reversal of velocity in the upper layer, and hence barotropically stable, as was shown in Part I. Figure 31 displays dispersion diagrams for the phase speed and growth rates for the decreasing values of the depth ratio $r = 100, 10, 2, 0.5, 0.1$ at stratification parameter $s = .5$. Compared to the one-layer case, several new features are manifest.

First, a new dispersion curve $kc = 1$ appears. It corresponds to inertial motion in the lower layer, with the quiescent upper layer, as follows from figure 32 where the velocity and pressure fields in both layers are presented. The clearly visible absence of pressure variations is typical for inertial oscillations. This mode was already discussed in Paldor & Ghil (1991). Again, as seen from figure 32, it is a lower-layer motion, which explains the absence of the corresponding curve in the one-layer dispersion diagram of Part I. In spite of intersections of this curve with other branches of the dispersion diagram, no resonances, and hence no instabilities between the inertial motion and other modes arise due to its pressureless character. Indeed, as shown by Cairns (1979), pressure fluctuations are necessary for the instability to arise.

Second, a bunch of dispersion curves with $c \approx 0$, which are all jammed into a single line in figure 31 due to insufficient graphical resolution, arises. A sequence of close dispersion curves is seen if zoomed in, cf figure 33. It corresponds to a set of Rossby modes in the lower layer, of different structure in the direction perpendicular to the coast, arising due to the variations of PV imposed by the inclined interface. These Rossby modes can resonate with the frontal mode and the Poincaré modes and produce instabilities even for the very large r, as seen from the figure 33. Yet, growth rates of these instabilities are indeed very small and their unstable wavenumbers intervals are very narrow for large r.

Panels (b) and (c) in figure 31, corresponding to $r = 10$ and $r = 2$ respectively, show two well-formed zones of instability that can be easily interpreted by looking at the dispersion curves for the corresponding modes. The first instability ($k < 1$) results from the already mentioned resonance between a Rossby wave in the lower layer and the frontal mode in the upper layer. The corresponding pressure and velocity fields in both layers are plotted in the panel (a) of figure 34 and comfort the interpretation.

The Rossby eigenmodes are absent in the upper layer owing to the uniformity of PV.[7] However, as was already discussed in Part I, the frontal mode has the characteristics of a Rossby wave for low wavenumbers, and the unstable mode under consideration is therefore very similar to the classical baroclinic instability which can be described as the interaction between two Rossby waves propagating in each layer, see Hoskins *et al.* (1985). It is interesting to note that the uniform PV in the upper layer does not satisfy the Charney-Stern theorem of the PV gradient inversion between the two layers. Hence, this instability has been interpreted as ageostrophic by numerous previous authors, but

[7] They are replaced by continuous spectrum of singular modes which do not interact with the modes in the lower layer as explained e.g. in Iga (1997).

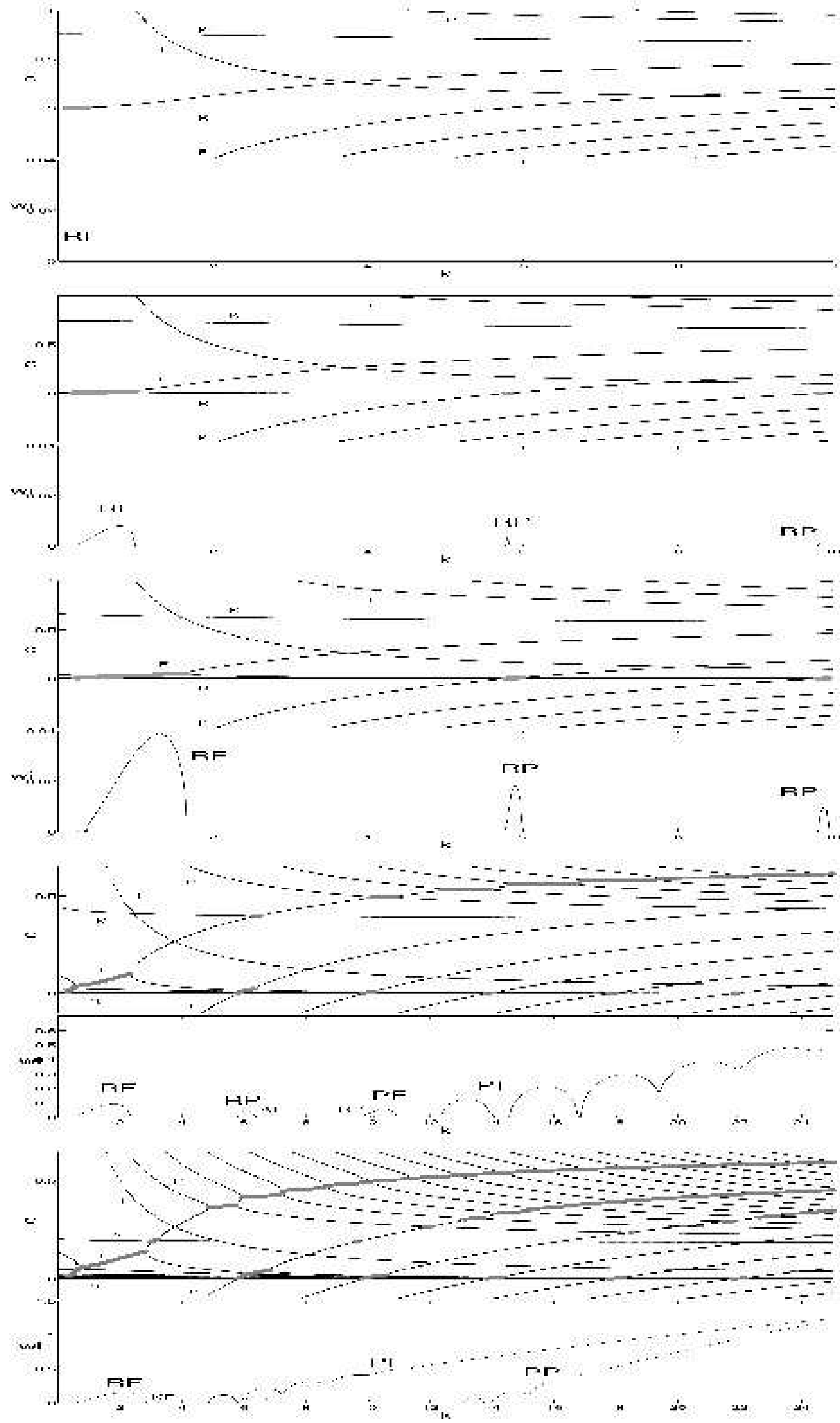

FIG. 31 – Dispersion diagrams of the eigenmodes for $R_d = 1$ corresponding to the basic state profile with constant potential vorticity in the upper layer and $s = .5$. The depth ratio between the lower and the upper layer is : (a) $r = 100$, (b) $r = 10$, (c) $r = 2$, (d) $r = 0.5$ and (e) $r = 0.1$. The horizontal scale of the two bottom panels was shrinked to show the appearance of short-wave KH instabilities.

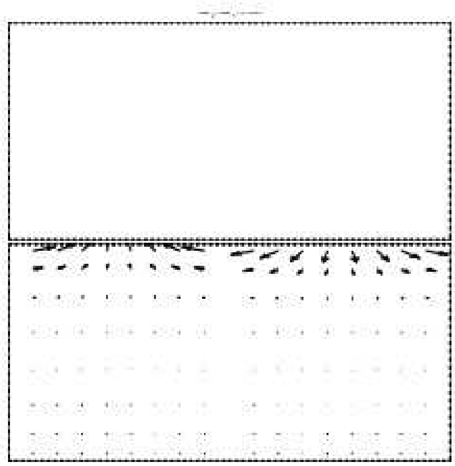

FIG. 32 – Pressure and velocity fields of the inertial mode in the upper layer (top) and in the lower layer (bottom) corresponding to the dispersion curve $kc = 1$ for $k = 10$ and $r = 100$. Maximum value for u_2 and v_2 is 0.8 while u_1, v_1, π_1 and π_2 are of order 10^{-6} or less and hence are not visible in the figure.

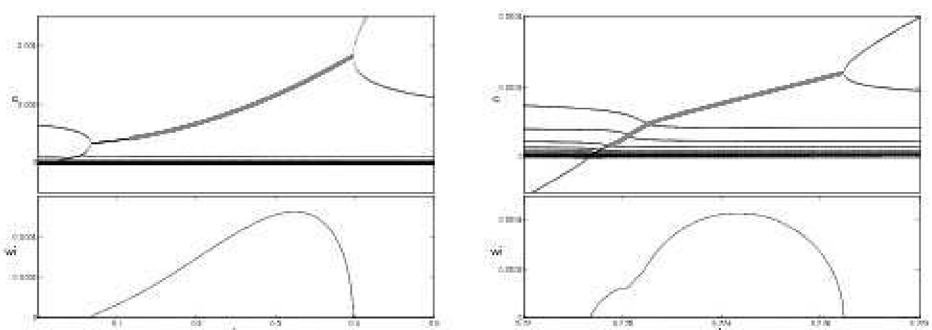

FIG. 33 – Zoom of the RF instability part (left) and RP instability part (right) of the figure 31, panel (a).

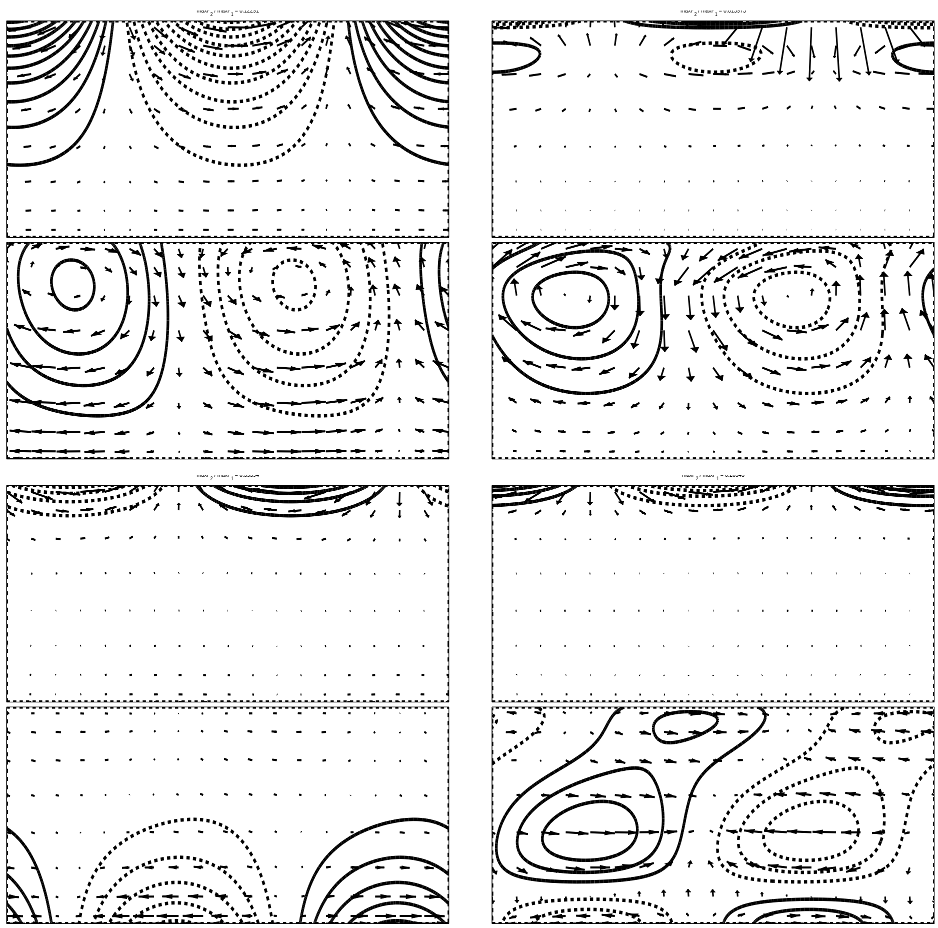

FIG. 34 – Pressure and velocity fields of the unstable modes of the barotropically stable current, from left to right, and top to bottom, (*a*) Rossby mode in the lower layer and the frontal mode in the upper layer (RF instability), (*b*) Rossby mode in the lower layer and the first Poincaré mode in the upper layer (RP instability), (*c*) first Poincaré mode in the lower layer and the frontal mode in the upper layer (PF instability). Pressure contours at the interval 0.015 in the lower layer, and at the interval 0.05 in the upper layer. Here and below the full lines correspond to positive and the dotted lines to negative values. Upper (lower) graph in each panel : upper (lower) layer.

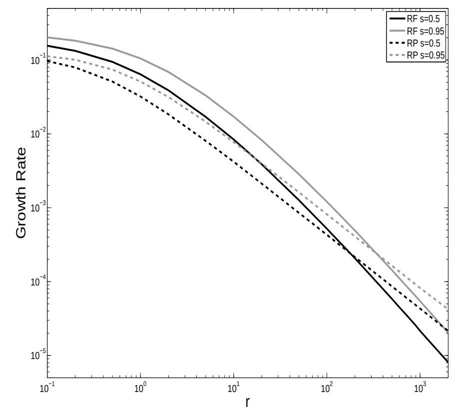

FIG. 35 – Maximum growth rates for the RF instability (thick line) and RP instability (dotted line) as a function of the depth ratio r for $s = 0.5$ (black) and $s = 0.95$ (grey).

it is also possible to interpret it as an extension of a QG instability, see a discussion of this point in Boss *et al.* (1996). We will call it RF in what follows.

The second instability corresponds to Poincaré modes in the upper layer resonating with a Rossby wave in the lower layer. The pressure and velocity fields for the second unstable mode are plotted in the panel (b) of figure 34, and confirm this interpretation. Note that the same instability appears at higher k for Poincaré modes of higher order with decreasing growth rates. We will call this instability RP. Note that this instability is often confused with Rossby-Kelvin instability, as in Sakai (1989).

Panel (d) in figure 31, corresponding to $r = 0.5$, displays a new zone of instability at $k = 6.25$ with very low growth rates corresponding to the interaction between the Kelvin mode in the lower layer and the frontal mode in the upper layer, which is plotted as (c) in figure 34, but above all it displays several new zones of instability at higher wavenumbers with very high growth rates. These are due to the interaction of the frontal mode in the upper layer with various Poincaré modes in the lower layer. This short-wave instability is analogous to the one described by Paldor & Ghil (1991) for the zero-PV case. The frontal mode has the characteristics of a gravity wave for high wavenumbers, this instability is therefore very similar to the Kelvin-Helmoltz (KH) one. The pressure and velocity fields for the first Poincaré mode in the lower layer are plotted as (d) in figure 34. The instabilities in question may be called PF, or simply KH.

Panel (e) in figure 31, corresponding to $r = 0.1$, is similar, with the addition of resonances between Poincaré modes in the lower layer and the upper layer corresponding to the standard KH instability, which may be also called PP to stress its origin (cf. Sakai (1989)).

We presented here the results of the stability analysis at varying r and fixed s. It is easy to repeat the analysis for fixed r and varying s (not shown). Not surprisingly, increasing (decreasing) s has destabilizing (stabilizing) influence. To give an idea of the s dependence of the growth rates, we plotted in figure 35 the dependence of the growth rates of RF and RP instabilities on r and s.

Let us summarize the linear stability analysis of the barotropically stable two-layer BDCC. For lower layers deeper than the upper layer the flow displays two types of baroclinic instabilities : a long-wave RF one, and a shorter-wave RP one. Both are extremely weak and of negligeable measure in k-space for very large depth ratios, but become more and more vigorous when the depth ratio is decreasing, having comparable growth rates. When the lower layer become of the order of, or shallower than the upper one, a series of short-wave vigorous KH instabilities appear.

Unstable modes of the barotropically unstable flow

We now consider the barotropically unstable basic flow. The basic state in the upper layer is now unstable, like in Part I. Figure 36 shows phase speed and corresponding growth rates for decreasing values of the depth ratio $r = 100, 10, 5, 2, 1.5$.

We recover the one-layer results when $r \to \infty$ (cf figure 4 in Part I, and panel (a) in figure 36), with the main resonance between the Kelvin mode and the frontal mode in the upper layer (KF1) and other instability zones at wavenumbers higher than 8, with much lower growth rates, corresponding to the resonance of the Kelvin mode and the first frontally trapped unbalanced Poincaré mode (KP1), and the interaction of the first coastally trapped Poincaré mode with the balanced frontal mode (PF1), respectively, as already mentioned in Part I.

The pressure and velocity fields of the related unstable KF1 mode in the upper layer are plotted in the upper graph of the panel (a) of figure 37, and show absolute coincidence with the corresponding mode of Part I. Note that related pressure perturbations in the lower layer (lower panel in figure 37) are at least one order of magnitude smaller than in the upper one for all instabilities, except for the KH one.

As the depth ratio decreases, the wavenumbers and growth rates for these unstable modes stay quasi-identical, but in parallel, as in the previous case, new instabilities appear due to the baroclinic resonances between a wave in the lower layer and a wave in the upper layer.

Panels (a), (b) and (c) in figure 36, corresponding to $r = 100$, $r = 10$ and $r = 5$, respectively, show three new zones of instability as compared to the one-layer case. They can be easily interpreted by looking at the dispersion curves of the corresponding modes. The first instability zone (from left to right on the wavenumber axis) is due to the resonance between a Rossby wave in the lower layer and the frontal mode in the upper layer, as in the previous barotropically stable case (RF instability). The corresponding pressure and velocity fields are plotted in panel (b) of figure 37. (Slight differences with respect to the similar mode presented in panel (a) of figure 34 are due to the difference in the mean flow profile.) The second instability zone corresponds to the barotropic instability mode which was already discussed above. The third instability zone corresponds to the resonance between a Rossby mode in the lower layer and a Kelvin mode in the upper layer, which is usually called Rossby-Kelvin (RK) instability (see Sakai (1989); Gula *et al.* (2009a)). Note that this unstable mode was not present in the previous case of zero zonal velocity at the wall. The corresponding pressure and velocity fields are plotted in panel (c) of figure 37. The fourth instability zone, as in the barotropically stable case, corresponds to the resonance between a Rossby wave in the lower layer and a Poincaré mode in the upper layer (RP instability which is often confused with RK instability). The pressure and velocity fields for this mode are plotted as (d) in figure 37.

Panel (d) in figure 36, corresponding to $r = 2$, displays new zones of instability at higher wavenumbers similar to those found in Paldor & Ghil (1991). These are due to the interaction of the frontal mode in the upper layer with various Poincaré modes in the lower layer, as in the barotropically stable case. An example of such unstable PF mode can be seen in figure 34. For high wavenumbers, the frontal mode behaves like a

Poincaré (gravity) mode and this instability indeed has then the properties of the KH instability, which is in fact should be called PP in terms of our conventions, cf. Sakai (1989).

Let us summarize the results of the linear stability analysis for the barotropically unstable two-layer BDCC. For very deep lower layers the only instability is the barotropic one of the one-layer reduced-gravity approximation. When the depth of the lower layer diminishes, the barotropic instability remains dominant, but RF, and RK/RP instabilities appear with, respectively, lower and higher characteristic wavenumbers. For lower layers of comparable or smaller than the upper one depth vigorous short-wave KH (i.e. PF and PP) instabilities appear.

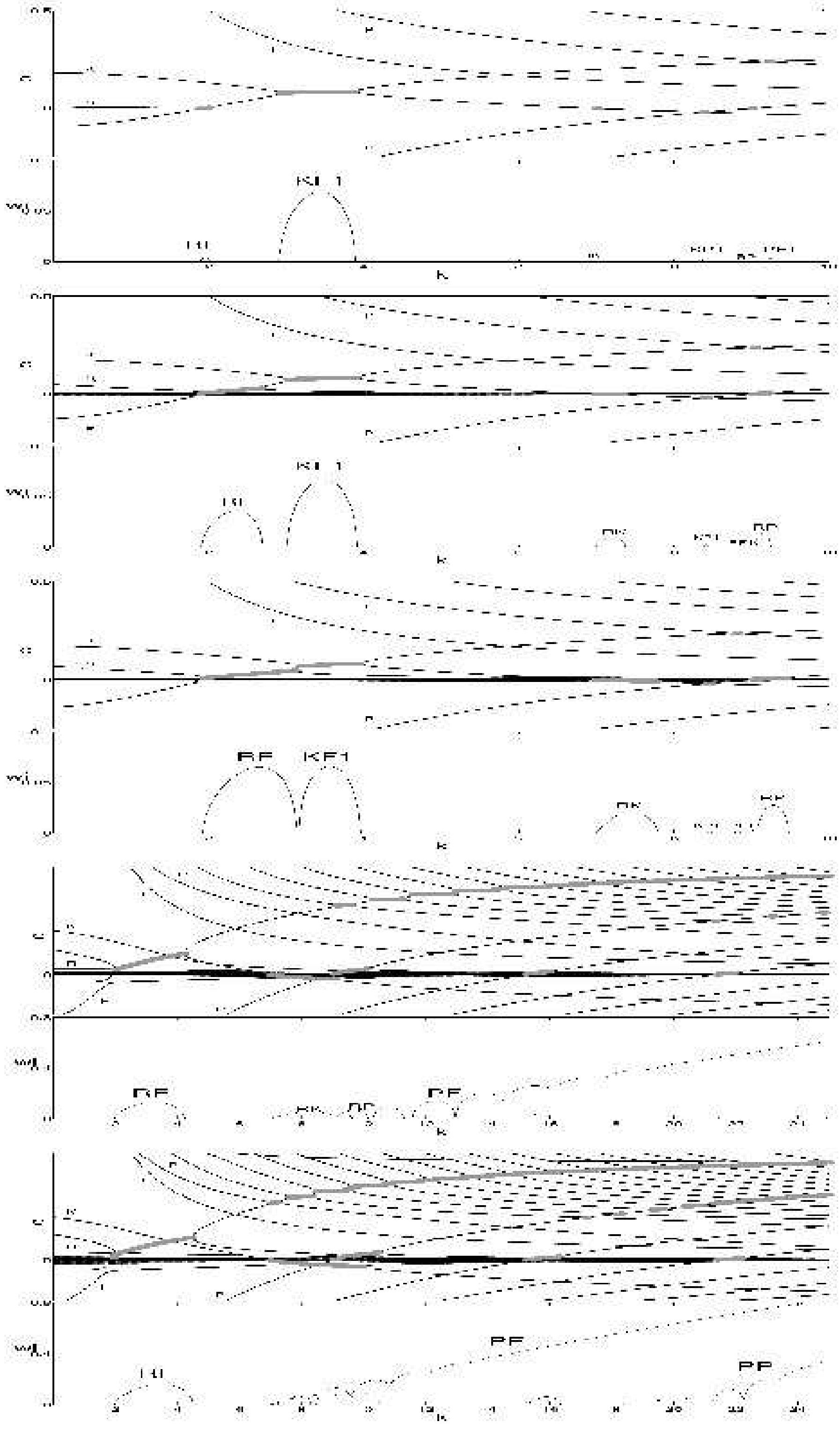

FIG. 36 – Dispersion diagrams of the eigenmodes for $s = 0.5$ and for $R_d = 1$ corresponding to the basic state profile with constant potential vorticity in the upper layer. The depth ratio between the lower and the upper layer varies as follows : (a) $r = 100$, (b) $r = 10$, (c) $r = 5$, (d) $r = 2$ and (e) $r = 1.5$. The horizontal scale of the two bottom panels was shrinked to show the appearance of short-wave KH instabilities.

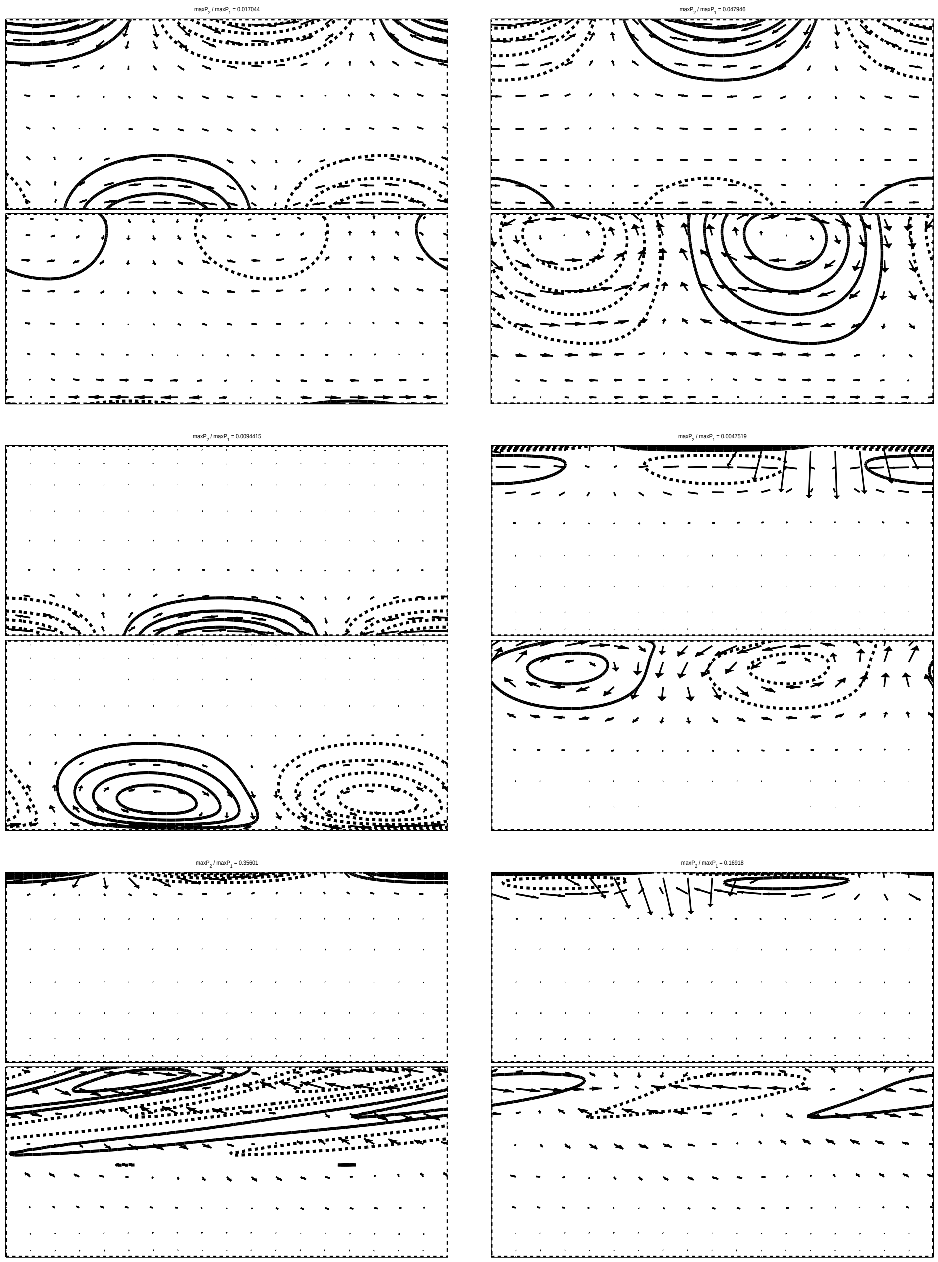

FIG. 37 – Pressure and velocity fields of the unstable modes for the barotropically unstable coastal current. From left to right and from top to bottom : (a) resonance between a Rossby mode and the frontal mode (corresponding to the frontal instability in the reduced gravity model), (b) resonance between a Rossby mode in the lower layer and the frontal mode (RF instability), (c) resonance between a Rossby mode in the lower layer and a Kelvin wave in the upper layer (RK instability), (d) resonance between a Rossby mode in the lower layer and the first Poincaré mode in the upper layer (RP instability), (e) resonance between a Poincaré mode in the lower layer and the frontal mode in the upper layer (KH instability) and (f) resonance between a Poincaré mode in the lower layer and a Poincaré mode in the upper layer (KH instability). Pressure contours interval is 0.1 in the upper layer for all panels, and pressure contours interval in the lower layer is 0.001 for (a) and (b), 0.0005 for (c) and (d), and 0.05 for (e) and (f). Upper (lower) graph in each panel : upper (lower) layer.

6.4.3 Non-linear evolution of unstable modes

Following the same philosophy as in Part I, we will investigate in this section the nonlinear evolution of the instabilities identified from the linear stability analysis. For this we need adequate numerical tools. As was already mentioned in the Introduction, the two-layer shallow water equations represent a system of mixed type, with transitions from hyperbolicity to ellipticity which are, generally, very difficult to treat numerically. Physically, the loss of hyperbolicity in the two-layer shallow water system corresponds to the onset of KH instability (LeSommer *et al.* (2003)). Another difficulty, which is more classical, is the lack of a conservative quantity, since only the total momentum is conserved, but not the momentum of each layer separately. This implies the lack of a unique set of Rankine-Hugoniot conditions for the weak solutions of the system. A recently proposed new well-balanced scheme for multi-layer shallow water equations, Bouchut & Zeitlin (2009), is the first which treats the loss of hyperbolicity in a satisfactory manner. In what follows, we will implement this scheme, with inclusion of rotation along the lines of Bouchut *et al.* (2004), in order to analyse nonlinear evolution of the unstable BDCC.

We first sketch the properties of the multi-layer version of the high resolution well-balanced finite-volume numerical scheme in section 6.4.3. We then study the nonlinear development of a perturbation for a barotropically stable flow in section 6.4.3, and the nonlinear evolution of the most unstable mode for a barotropically unstable flow in section 6.4.3.

A well-balanced entropy satisfying finite-volume scheme for the multi-layer rotating shallow-water model

The method of Bouchut & Zeitlin (2009) is based on the idea of operator splitting for the multi-layer shallow water equations, already implemented in Bouchut & Morales (2008). It consists in solving the equations successively layer by layer, treating the interfaces between the layers as effective topography for the layer under resolution. The method has the following advantages : a) if the resolution for each layer is performed with a well-balanced sub-scheme, the whole scheme is well balanced, b) if the resolution for each layer is performed with an entropy-satisfying sub-scheme, the whole scheme is entropy-satisfying, i.e. the total energy is decreasing through shocks, c) the scheme is nonnegative in level thicknesses, and allows for "drying" of layers, d) no estimate of the eigenvalues of the whole system (which become complex when the hyperbolicity is lost) is needed, the scheme is always consistent and one can use the CFL conditions associated with each subsystem. A variant of the splitting scheme allowing to solve simultaneously, and not successively, for all layers, a "sum scheme", cf Bouchut & Zeitlin (2009), is applied, with an upwind corrected hydrostatic reconstruction scheme and relaxation solver. A second-order reconstruction scheme in space is used, together with a two-step Heun scheme in time. The two-dimensional aspects are treated direction by direction.

Non-linear evolution of a barotropically stable flow

Baroclinic instability We will first consider the basic flow with zero velocity at the wall, see height and velocity profiles in figure 30. This corresponds to the barotropically stable flow studied in section 6.4.2

We simulate the fully nonlinear evolution of the instability corresponding to the most unstable mode (RF) (figure 34, panel (a)) with $k_0 = 0.98$ for the basic state with $r = 2$ (cf figure 31, panel (c)). The boundary conditions are periodic in the zonal direction, with period $2\pi/k_0$, and we initialize the simulation with the most unstable x-periodic eigenmode obtained from the linear stability analysis. The allowed wavenumbers are then integer multiples of k_0. Note that this wavenumber has been chosen in order to authorize also the RP instability which have a wavenumber $\approx 6k_0$, cf. figure 31. The spatio-temporal evolution of the instability is displayed in figure 38 and the growth of kinetic energy for the most energetic $k = k_0$ mode is presented in figure 39 for both layers. The unstable RF mode grows exponentially until $t = 125$ with an average growth rate $\sigma \approx 0.02$ leading to the formation of baroclinic vortices. Strong events of dissipation happen for $150 < t < 200$, essentially near the wall (see (c) in figure 38, where the white areas superimposed on the isolines of the height field correspond to spatial distribution of the dissipation rate). While the vortex develops, a local return current appears close to the wall, and a Kelvin front forms and breaks leading to shock formation and enhanced dissipation, as was explained in Part I (cf a zoom of this event in figure 40). The small scale motions in the lower layer at this stage are presented in figure 41, where the pressure and velocity fields of the main vortex have been filtered. They correspond to IGW emission by the Kelvin front, and the adjustment of the vortex. The dissipation due to the Kelvin front leads to reconnection of the vorticity isolines allowing for vortex detachment from the mean flow and its offshore motion. Figure 42 displays the pressure distribution in both layers at $t = 250$, when the vortex is well-formed and detaches. It is the dipolar structure of the vortex, particularly clearly seen in the lower layer, which drives it offshore. We present the cross-sections of the detaching vortex in figure 43, where its lens-like structure is clearly seen.

The total energy loss during the whole simulation is about 0.03% of the total initial energy or 25% of the initial kinetic energy, as shown in figure 44. It is non-negligible but stays quite acceptable compared to rather long duration ($t = 500f^{-1}$) of the simulation. In the numerical scheme we are using, the numerical dissipation acts only in the zones of high gradients. The events of enhanced dissipation take place during the detachment of the vortex, which is consistent with what was stated earlier. The slow monotonic decrease of energy during the whole simulation is explained by the fact that it is easy to generate micro shocks in the shallow regions where the upper layer is close to drying.

We have also directly simulated the nonlinear stage of the second and third instability zones of the phase diagram of figure 31, panels (b) and (c), corresponding to the resonances between a vortical mode in the lower layer and Poincaré modes of different orders in the upper layer (figure 34 (b)). These modes, as well as even higher-k unstable modes has high gradients close to the front and thus are likely to be damped owing to dissipation like it happens in the problem of instabilities of coupled density fronts, cf Scherer & Zeitlin (2008). Indeed we observed a rapid energy decay at the initial stage of the simulation. The growth of such unstable modes is almost immediatly arrested and they are hence unable to change the structure of the background flow in contradistinction with the main instability mode. After some time the perturbation eventually leads to the development of the aformentioned baroclinic instability. This means that in the context of long-time nonlinear evolution of coastal currents, the only relevance of these high wavenumber modes is to provide a dissipative sink of energy.

Joint evolution of KH and RF instabilities In order to study the role of short-wave KH instability, we repeat the previous simulation with the depth ratio lowered down to $r = 0.5$. The most unstable modes are now KH ones with typical wavenumbers $k > 20$, while the RF instability (panel (a) in figure 34) is still supposed to develop, but at a wavenumber $k = 1.4$, and with a lower growth rate as can be seen in the phase

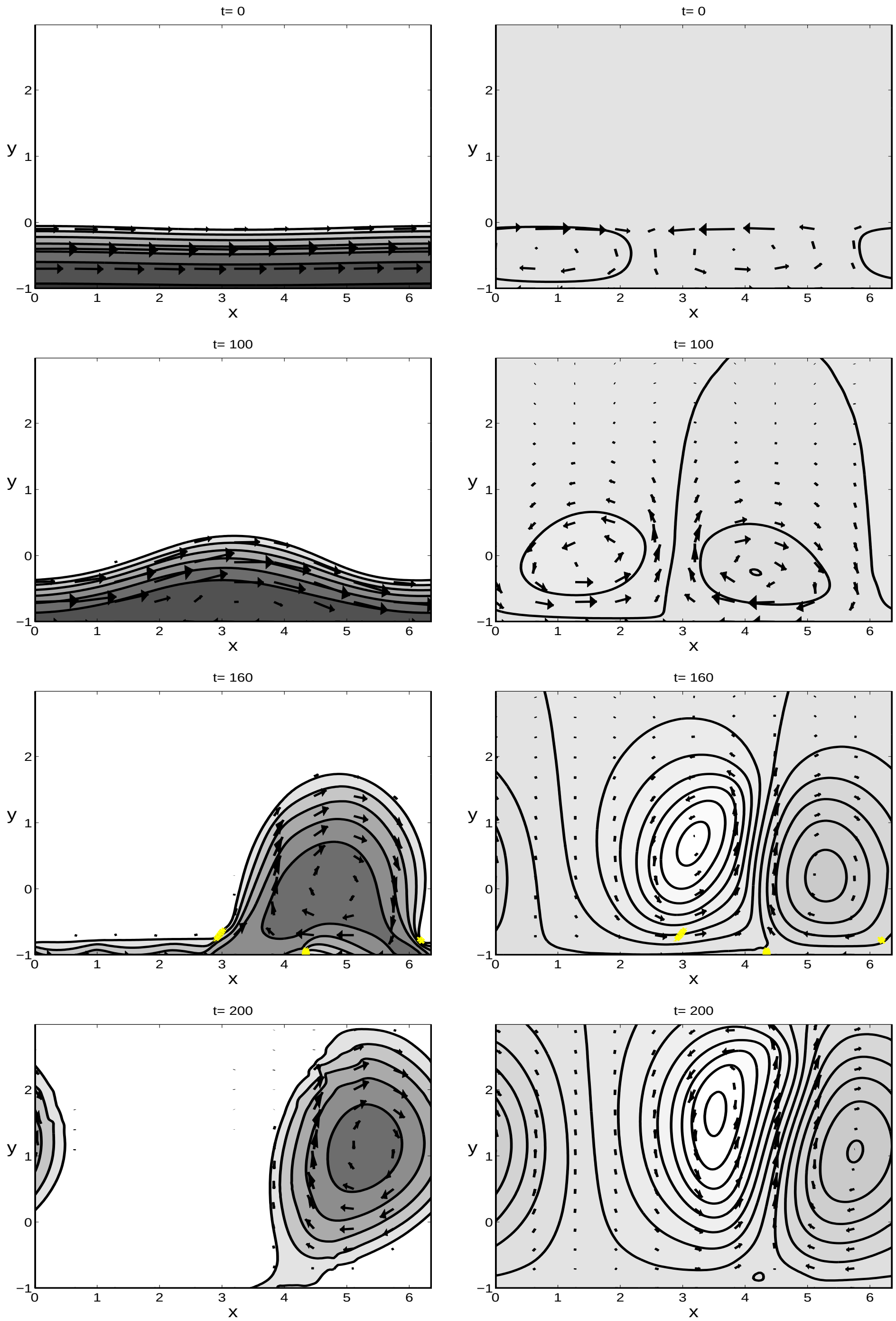

Fig. 38 – Levels of $h_1(x, y, t)$ in the upper layer (left) and isobars of $\pi_2(x, y, t)$ in the lower layer (right) at $t = 0, 100, 150$ and 200 (resp. a), b), c) and d) in the text) for the development of the unstable RF mode superposed on the basic flow with a depth ratio $r = 2$. Contours at interval is 0.1 for $h_1(x, y, t)$ (left column) and 0.01 for $\pi_2(x, y, t)$ (right column). Darker (lighter) zones correspond to positive (negative) anomalies of h_1 an π_2. The arrows indicate the mass flux $h\vec{v}$. The initial amplitude of the perturbation is 10% of the maximum depth of the balanced flow. The calculation domain is periodic in the x-direction. White area superimposed on the isolines of the height field corresponds to spatial distribution of the dissipation rate between 0.009 and 0.09 (the maximum value). The dissipation rate is calculated as the deviation from the energy balance in each cell per time step, in non-dimensional units.

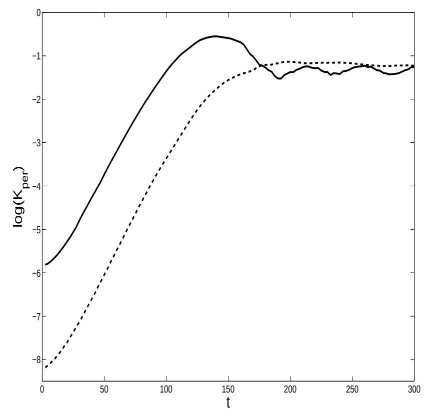

FIG. 39 – Logarithm of the kinetic energy K_{per} of the perturbation for the simulation of figure 38 (normalized by initial total kinetic energy) for mode $k = k_0$ in the upper layer (thick line) and in the lower layer (dashed line).

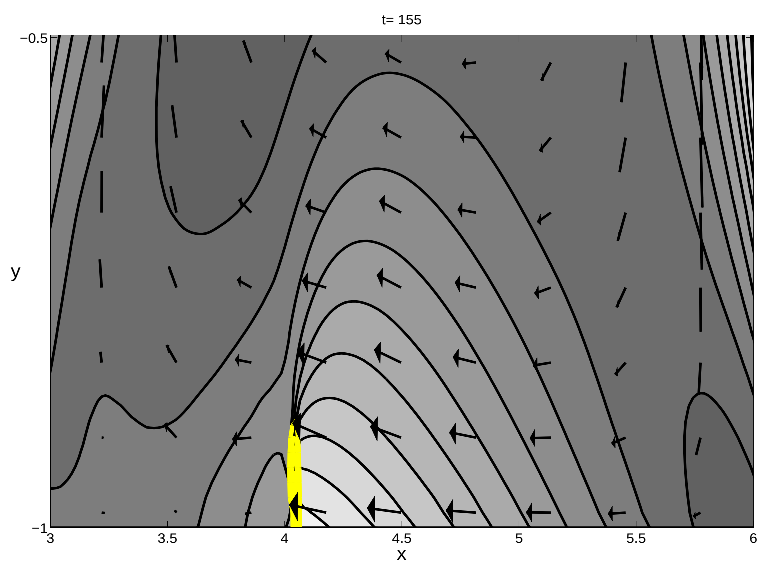

FIG. 40 – Zoom of the figure 38, panel (c).

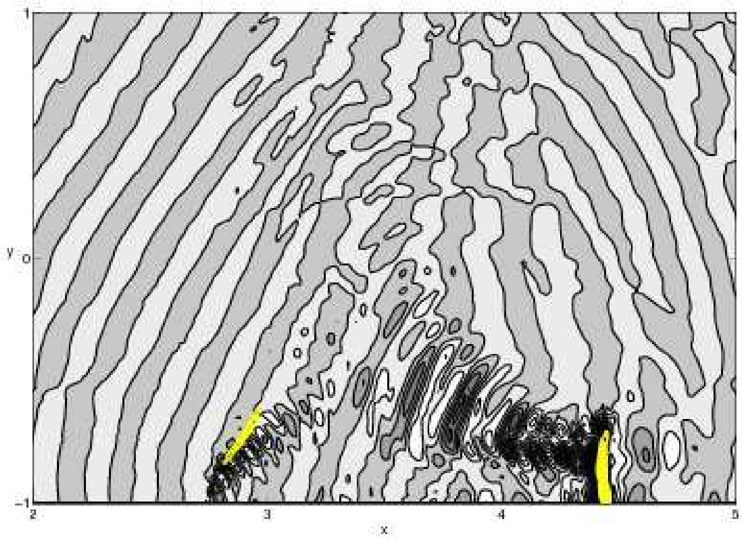

FIG. 41 – Isobars of $\pi_2(x, y, t)$ in the lower layer at $t = 160$ with mean zonal flow filtered out for simulation of figure 38. Only modes with $k > 4$ are represented.

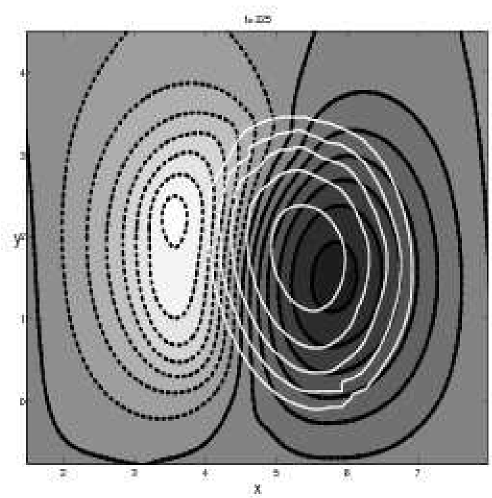

FIG. 42 – Isobars of $\pi_1(x, y, t)$ in the upper layer (white lines) and $\pi_2(x, y, t)$ in the lower layer (dark lines) at $t = 250$ for simulation of figure 38. Dark (light) background : anticyclonic (cyclonic) region.

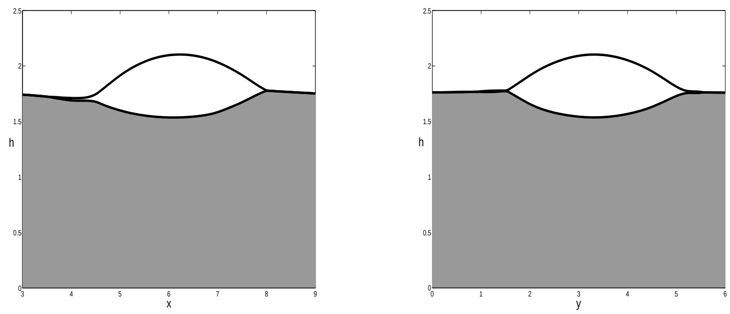

FIG. 43 – The x (left) and y (right) cross-sections of the detached vortex at $t = 300$ for the simulation of figure 38

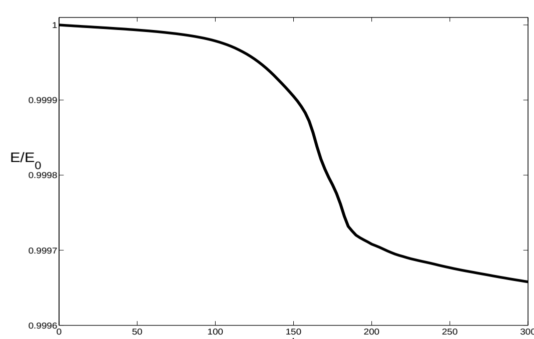

FIG. 44 – Time-dependence of the total energy normalized by the initial energy for the evolution of the instability.

diagram (panel (d) in figure 31).

Figure 45 shows the result of nonlinear evolution of the instability corresponding to the unstable RF mode with $k_0 = 1.4$ superimposed onto the basic flow. The zonal period is chosen to be $2\pi/k_0$ in non-dimensional units.

Looking at the right panel (b) of figure 45 and at the evolution of the kinetic energy K_{per} of the perturbation presented in figure 46, we see that short-wave structures are growing very fast during the earlier stage of the simulation ($t < 10$). The pressure and velocity fields of the corresponding perturbation are plotted in figure 47 and fit well the KH mode structure obtained from the linear stability analysis, cf. figure 34. From figure 48, where we plotted the energy spectrum of the flow at $t = 20$, we can see that the short-wave maximum is centered at $k \approx 29$. We can deduce that this mode has the growth rate $\sigma \approx 0.5$, which is coherent with the results of the linear stability analysis, see (d) in figure 31. Our numerical scheme allows to diagnose the loss of hyperbolicity, which is related to the KH instability, as was explained earlier. The non-hyperbolic domains are indicated in figure 47, which confirms their link with KH instability. Note that the system recovers its hyperbolicity once these instabilities are dissipated and disappear.

As we see, the small-scale KH instabilities do not qualitatively alter the flow, their only influence being to render it marginally KH stable through enhanced dissipation in the strong vertical shear regions. The mean current then develops secondary large-scale instabilities at $k = k_0$. The evolution is similar to the previous case of $r = 2$, except that, due to the thinner lower layer, the phase speed of the vortical waves in the lower layer increases, while the phase speed of the frontal wave remains the same, which makes the growth rate and wavenumber corresponding to the maximum growth rate increase (see figure 31 for comparison). The growth rate of this instability measured from the kinetic energy evolution is $\sigma \approx 0.1$, the instability then grows about 3 times faster than in the $r = 2$ case.

The total energy loss during the whole simulation is about 0.2% of the total initial energy or 25% of the initial kinetic energy as shown in figure 49. The events of enhanced dissipation take place during the appearance of KH instabilities (first peak of dissipation at $t \approx 10$) and during the detachment of the vortex ($t \approx 60$). Consistently with what was stated above, the overall dissipation during the saturation of small-scale KH instabilities is much less important than the dissipation during the saturation of the large-scale RF instability.

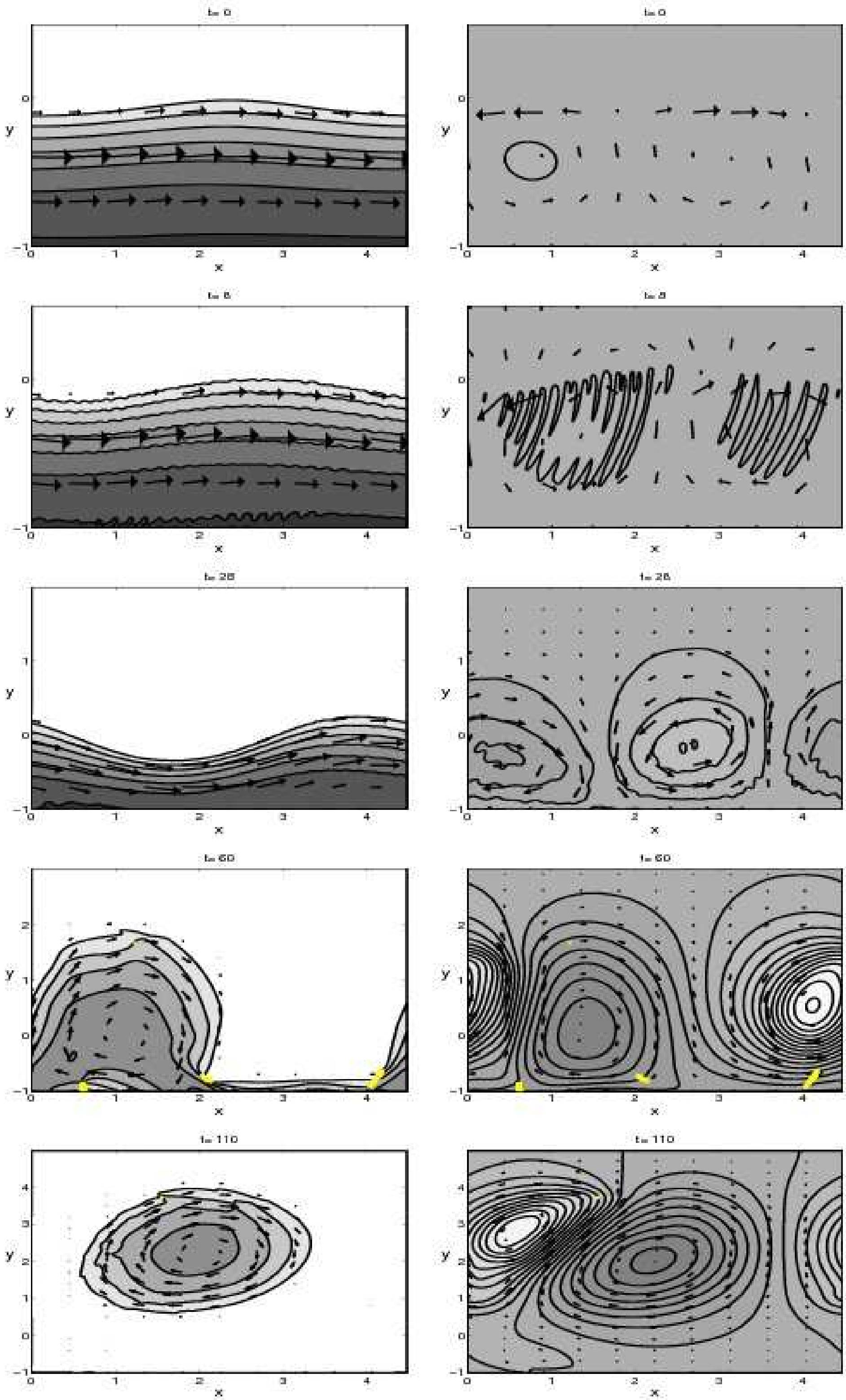

FIG. 45 – Levels of $h_1(x, y, t)$ in the upper layer (left) and isobars of $\pi_2(x, y, t)$ in the lower layer (right) at $t = 0, 20, 50, 100$ and 180 for the development of an initial perturbation superposed on the basic flow with a depth ratio $r = 0.5$. Same conventions as in fig. 38. Contours displayed are 0.01, 0.05, and further on at the interval 0.05.

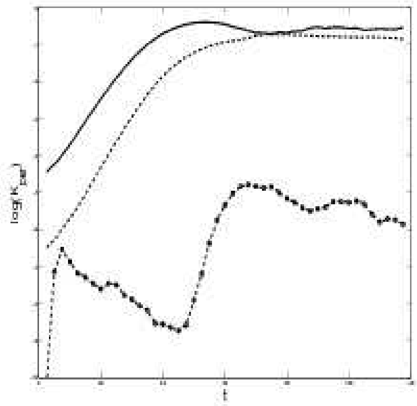

FIG. 46 – Logarithm of the kinetic energy K_{per} (normalized by initial total kinetic energy) of the perturbation for the simulation of figure 45 for mode $k = k_0$ in the upper layer (thick line) and in the lower layer (dashed line), and sum of modes with $k > 10\ k_0$ (dashed-dotted line).

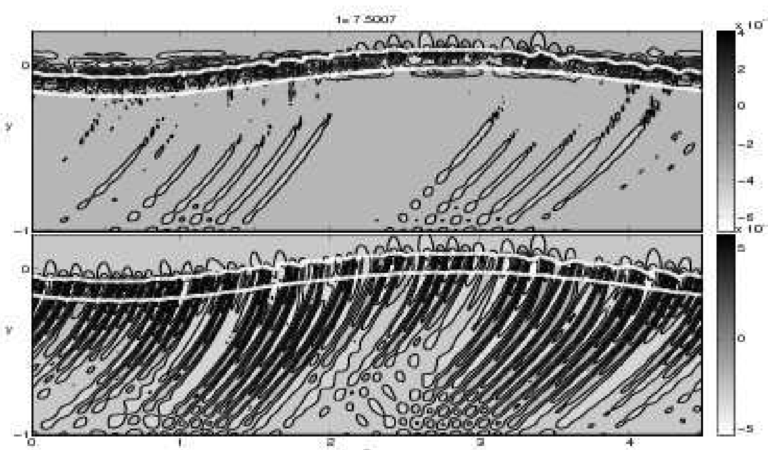

FIG. 47 – Contours of $\pi_1(x, y, t)$ (upper panel) and $\pi_2(x, y, t)$ (lower panel) with mean zonal flow filtered out (only modes with $k > 4\ k_0$ are represented) at $t = 20$ for the simulation of figure 45 with a depth ratio $r = 0.5$. The white line indicates the boundaries of non-hyperbolic domains.

FIG. 48 – Kinetic energy spectrum at $t = 20$ after development of the small-scale KH instabilities in the simulation of fig. 45.

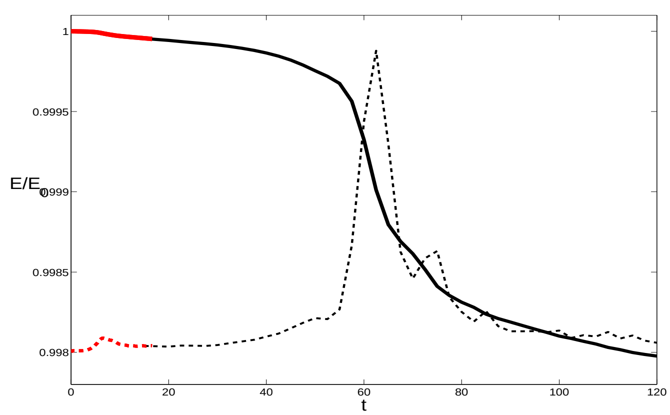

FIG. 49 – Time-dependence of the total energy normalized by the initial energy (thick line) and the dissipation rate (dashed line) for the evolution of the instability of figure 45.

Non-linear evolution of a barotropically unstable flow

In the previous section the barotropic instability of the upper-layer current, studied in Part I, was excluded. The natural question arises, how the admixture of the baroclinic instabilities change the evolution of the barotropic one. It is adressed in what follows.

Joint evolution of the barotropic and RF instability We simulate the fully nonlinear evolution of the instability corresponding to the most unstable mode with $k = 3.44$, as given by the linear stability analysis (cf figure 37, panel (a)) in a similar way as in Part I, but with the addition of an active lower layer. As expected from the linear stability analysis (figure 36 (a)), configurations with a very large depth ratio ($r = 100$), give absolute coincidence with the previous simulations in the reduced-gravity configuration. When the depth ratio is reduced to $r = 10$, baroclinic effects modify the flow. The stability diagram (figure 36 (b)) shows that even if the most unstable mode is still the barotropic one, some baroclinic instabilities also appear. The evolution of the flow in this case is shown in figures 50 and 52 illustrating, repectively, two different stages. The first stage ($t < 250$, figure 50) is close to reduced-gravity simulations of Part I : the unstable mode grows (panel (a)), saturates and modifies the mean flow (panel (b)), then a secondary instability grows and breaks (panel (c)) by reorganizing the flow (panel (d)). The evolution of the kinetic energy of the different perturbation modes in the upper layer presented in figure 51 is to be compared with that of the one-layer case (see figure 20 in Part I) and, as expected, is quite similar for $t < 200$. The total kinetic energy of the perturbation in the lower layer is also presented in figure 51. It is initially zero but is increasing throughout the simulation until the flow becomes clearly baroclinic.

The next stage of the evolution of the flow in both layers is shown in figure 52 for $t > 250$. As we have seen in Part I, the final state for the one-layer flow simulation exhibited a Rossby wave-like pattern, with anticyclones located near the coast inside meanders of the main current. As an active lower layer is now present, it will allow for interactions of such patterns with the vortical modes of the lower layer. In a similar way as for the barotropically stable flow of the previous section (figure 38), a baroclinic instability will then develop. Figure 52 shows the baroclinic interactions which lead to the formation of a vortex in the upper layer and of a dipole with a cyclone followed by an anticyclone in the lower layer, that detaches from the coast. Formation of cut-off vortices is clearly seen. As before it is the dipolar structure which is driving them offshore. We present the evolution of PV in both layers in this simulation in figure 53.

It should be noted that the evolution of the BDCC we observe here was quite forseable : with a deep lower layer the interaction betwen the two layers is rather weak and the rapid barotropic instability is dominant at the beginning. Baroclinic effects, as usual, come into play on longer time-scales.

The total energy loss during the whole simulation is about 0.08% of the total initial energy or 50% of the initial kinetic energy, as shown in figure 54. The events of enhanced dissipation take place during the breaking of the Kelvin mode (first peak of dissipation at $t \approx 25$), during the breaking of the secondary unstable wave ($t \approx 150$), and finally during the detachment of the vortex ($t \approx 300$).

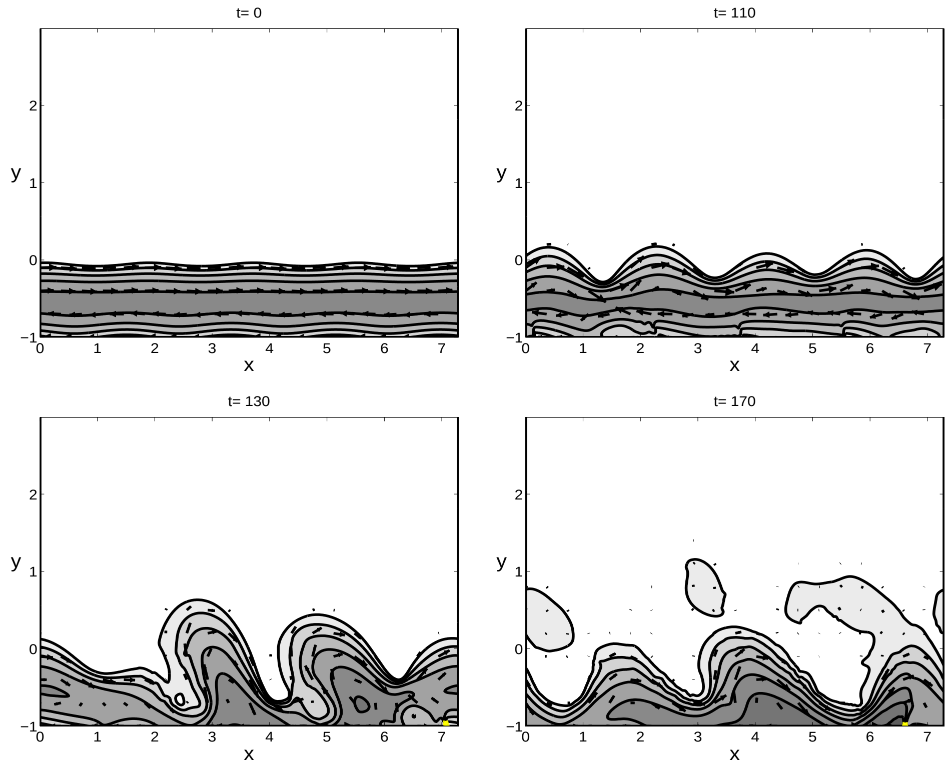

FIG. 50 – Levels of $h_1(x, y, t)$ at 0.05 interval are shown at $t = 0, 110, 130$ and 160 for the development of the most unstable mode of figure 37, panel (a), corresponding to the basic flow with constant PV and a depth ratio $r = 10$. Same conventions as in the previous figures of this type. The calculation domain is periodic in the x-direction and corresponds to 4 wavelenghts of the most unstable mode.

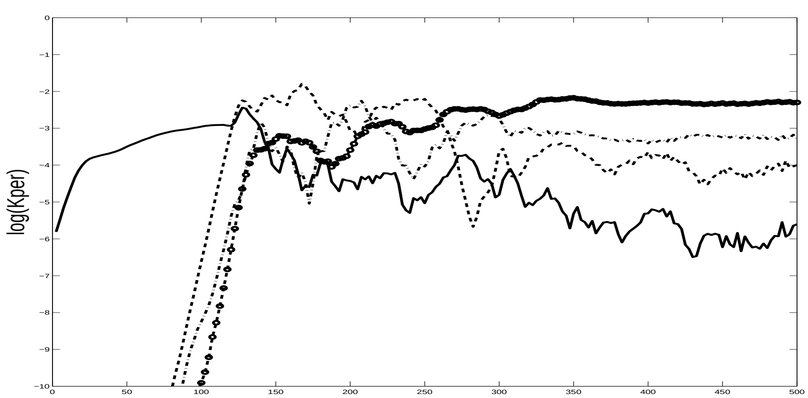

FIG. 51 – Logarithm of the kinetic energy K_{per} (normalized by initial total kinetic energy) of the perturbation for the simulation of figures 50 and 52 for mode $k = k_0$ in the upper layer (thick line), mode $k = 0.75\ k_0$ in the upper layer (dashed line), mode $k = 0.5\ k_0$ in the upper layer (dash-dotted line) and the total kinetic energy of the perturbation in the lower layer (round markers), as a function of time.

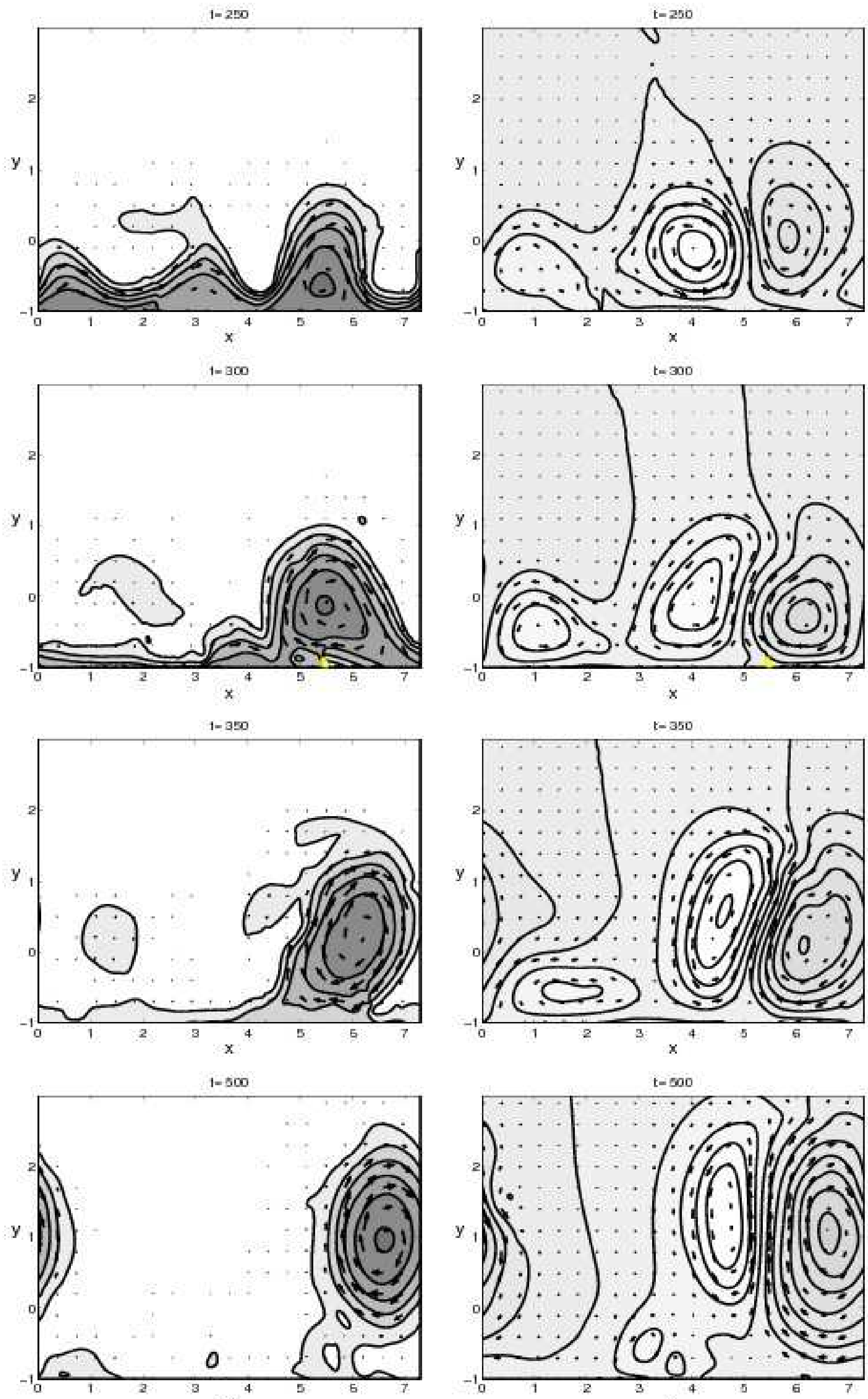

FIG. 52 – Levels of $h_1(x, y, t)$ (left) and $\pi_2(x, y, t)$ (right) at $t = 250, 300, 350$ and 500. Continuation of the simulation of figure 50. Contours at interval 0.05 for $h_1(x, y, t)$, and 0.005 for $\pi_2(x, y, t)$. Same conventions as in figure 38.

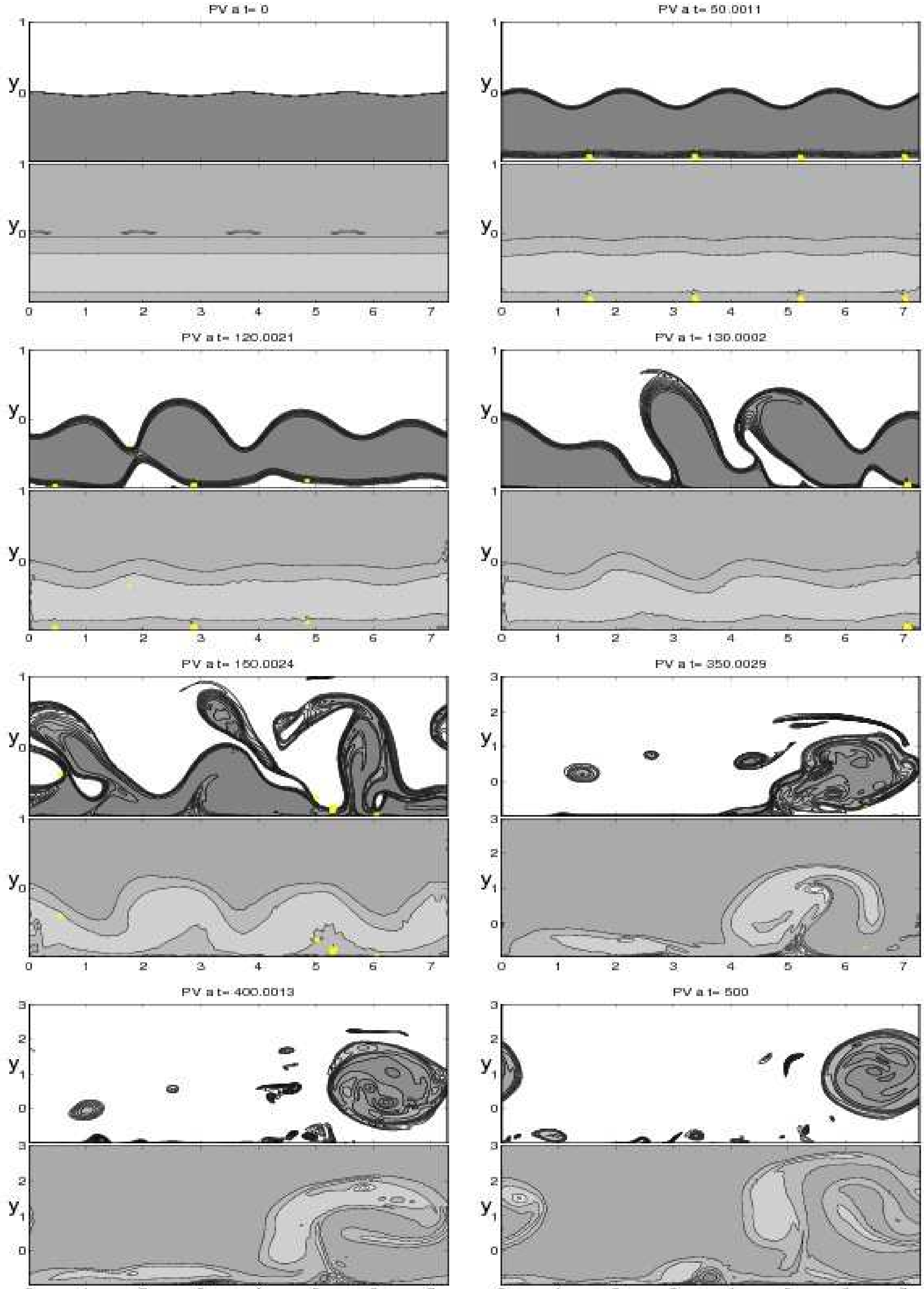

FIG. 53 – Contours of PV for the simulation 50 in the upper layer (top of each panel) and in the lower layer (bottom of each panel) for $t = 0, 50, 120, 130, 150, 350, 400, 500$. Contours at the interval 1 for PV in the upper layer and at the interval 0.1 for PV in the lower layer.

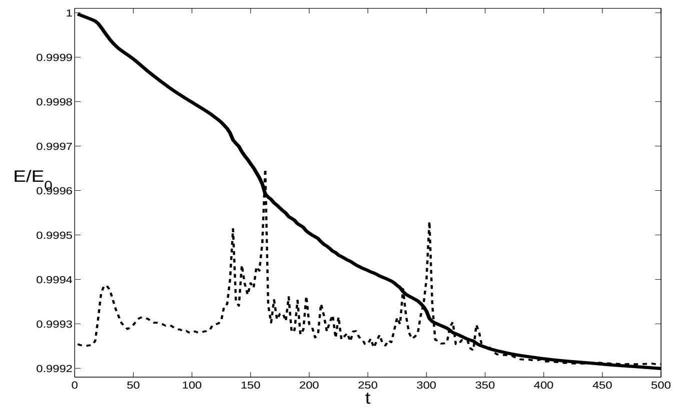

FIG. 54 – Time evolution of the total energy (continuous) normalized by the initial energy, and dissipation rate (dashed) for the simulation of figs. 50 and 52.

Joint evolution of the barotropic, KH and RF instabilities. We now investigate a flow with a small depth ratio, in order to understand the effect of strong coupling between the layers on the evolution of the barotropically unstable flow. Figure 55 shows the nonlinear evolution of the instability for a depth ratio $r = 2$. The zonal period is chosen to be $2n\pi/k_0$ with $k = 0.86$ and $n = 4$ in non-dimensional units.

As expected from the linear stability analysis, vigorously growing short-scale instabilities at the front develop during early stages of the simulation. The evolution of the kinetic energy K_{per} of the perturbation in the corresponding simulation is presented in figure 56. By similar reasoning as in the previous case, we can deduce that the kinetic energy of the short-scale modes ($k \approx 30$) is growing very fast for $t < 10$, with a growth rate $\sigma \approx 0.4$. The corresponding unstable short-wave mode is plotted in figure 57 (a), where one can clearly see the similarity with the linearly unstable mode of figure 34, with coupled short-wave Poincaré mode in the lower layer and short-wave frontal mode in the upper layer. As in the previous subsection we superimposed the borders of non-hyperbolic domains, which in fact are indicators of strong inter-layer shear, onto the figure 57. The system recovers hyperbolicity once these instabilities are dissipated.

The KH instabilities enhance dissipation but, as in the case of barotropically stable flow, do not significantly alter the mean flow. The unstable frontal mode (barotropic KF resonance) keeps on growing with a growth rate $\sigma \approx 0.06$ (see figure 36 (d) for comparison with the linear stability analysis). The Kelvin and frontal modes grow until the Kelvin mode breaks and modifies the mean flow along the coast (figure 57 (b)), in a similar way as in the simulations of Part I. The secondary unstable mode also described in Part I, then appears in the upper layer (figure 57 (c)) for the same wavenumber, in the form of two Rossby waves at each side of the flow. Contrary to the preceding simulations with larger depth ratio, the coupling between the two layers is much more important here, and the Rossby wave excited in the lower layer is strongly interacting with the upper layer one. The breaking of the unstable mode in the upper layer is then quite different, as it leads to quick formation of smaller vortices. This scenario is confirmed by the PV evolution presented in figure 58.

The total energy loss during the whole simulation is about 0.9% of the total initial energy or 65% of the initial kinetic energy as shown in figure 59. The events of enhanced

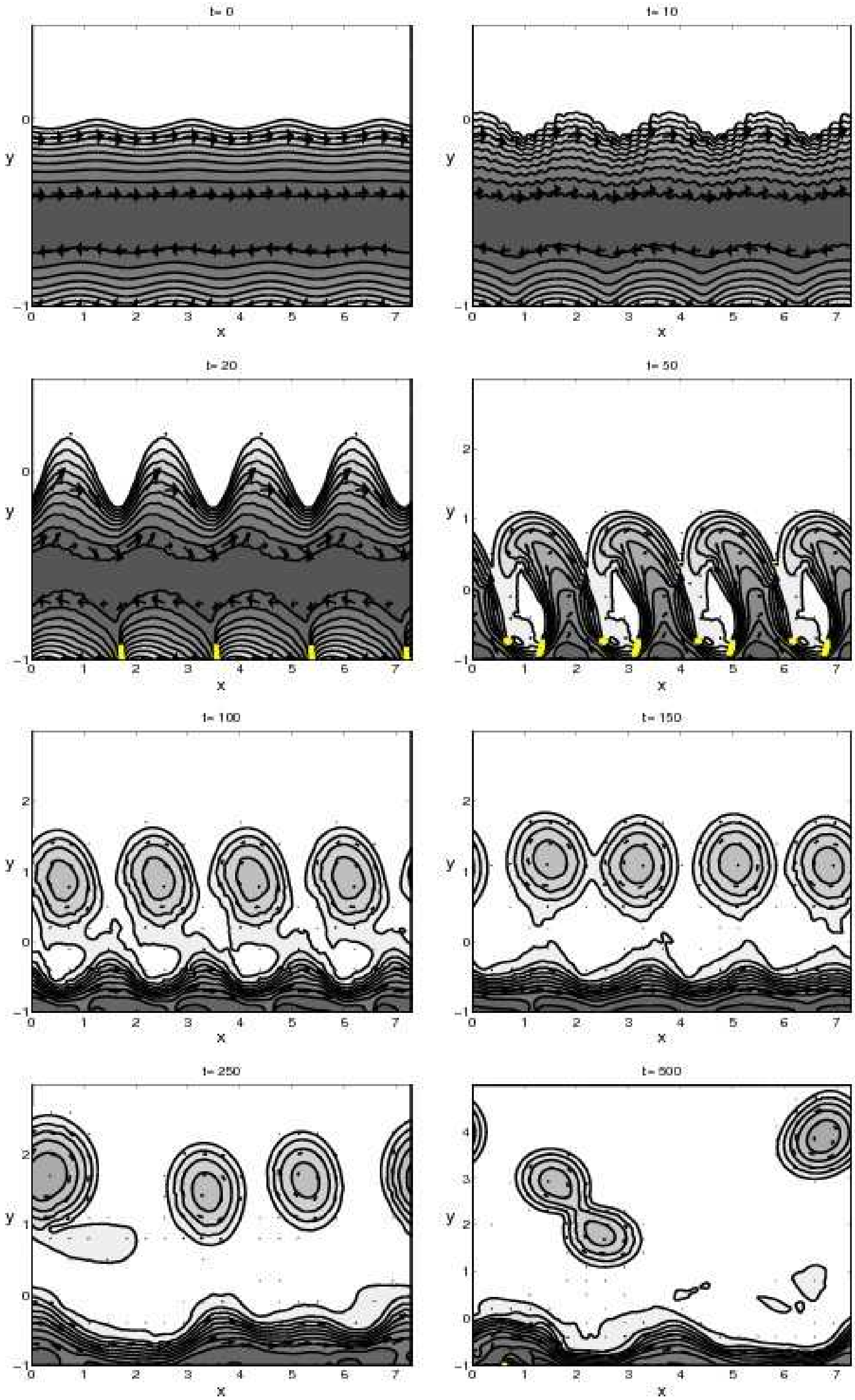

FIG. 55 – Levels of $h_1(x, y, t)$ at $t = 0, 10, 20, 50, 100, 150, 250$ and 500 for the development of the most unstable mode of figure 37, panel (a), corresponding to the basic flow with constant PV and a depth ratio $r = 2$. Contours at interval 0.025. Same conventions as in similar figures above.

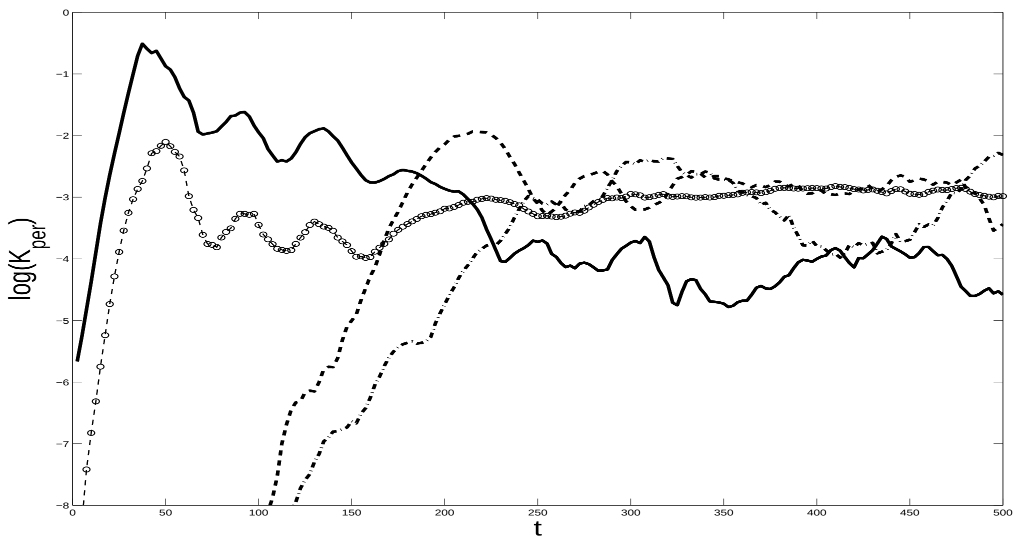

FIG. 56 – Logarithm of the kinetic energy K_{per} (normalized by initial total kinetic energy) of the perturbation for the simulation of figure 55 for mode $k = k_0$ in the upper layer (thick line), mode $k = 0.75\ k_0$ in the upper layer (dashed line), mode $k = 0.5\ k_0$ in the upper layer (dash-dotted line), and the total kinetic energy of the perturbation in the lower layer (round markers), as a function of time.

dissipation take place during the appearance of KH instability (first peak of dissipation at $t \approx 10$), during the breaking of Kelvin mode ($t \approx 30$) and during formation of vortices ($t \approx 50$).

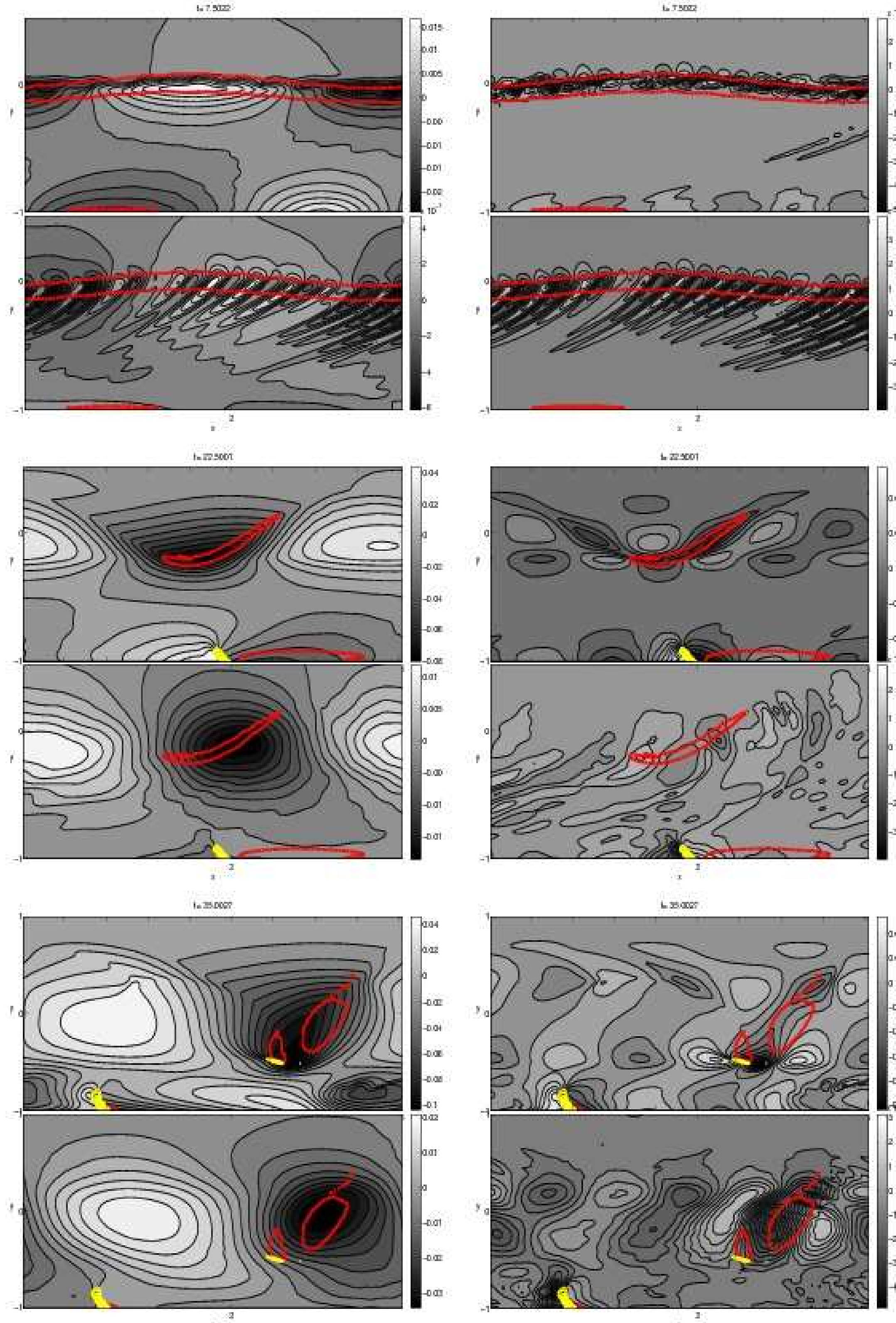

FIG. 57 – Isobars of $\pi_1(x, y, t)$ and $\pi_2(x, y, t)$ at $t = 7.5, 22.5$ and 35, with the zonal mean flow filtered out (left), and all modes with $k < 3\ k_0$ filtered out (right) for the simulation of fig. 55. The thick red line indicates the domains of hyperbolicity loss. The yellow line indicates spatial distribution of the dissipation rate.

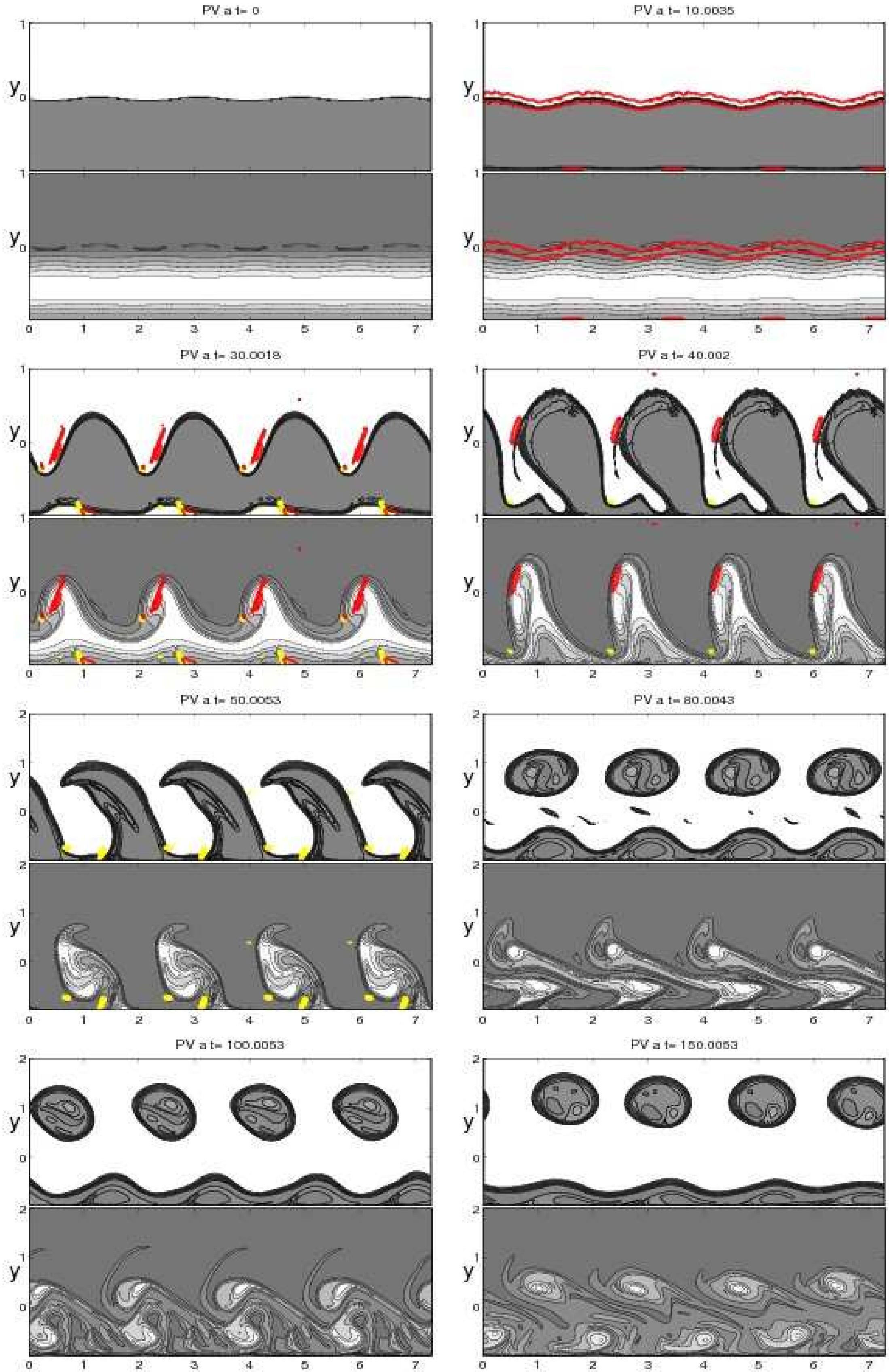

FIG. 58 – Contours of PV for the simulation 55 in the upper layer (top of each panel) and in the lower layer (bottom of each panel) for $t = 0, 10, 30, 40, 50, 80, 100, 150$. Contours at the interval 1. The thick red line indicates the borders of non- hyperbolic domains. The yellow line indicates spatial distribution of the dissipation rate.

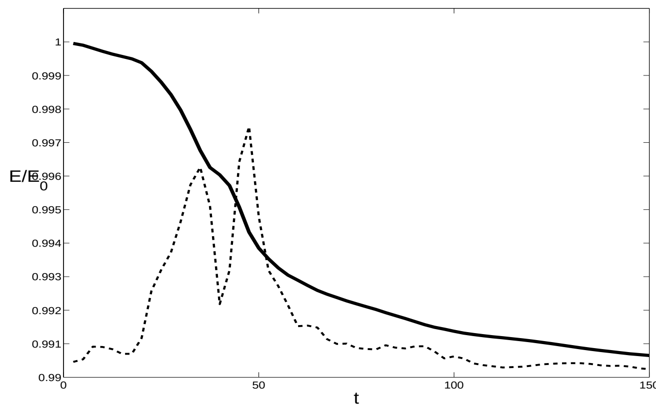

FIG. 59 – Time-dependence of the total energy normalized by the initial energy for the evolution of the instability.

6.4.4 Summary and Conclusions

We have investigated linear and nonlinear stability of buoyancy-driven coastal currents in the two-layer rotating shallow water model and generalized the results obtained for reduced-gravity one-layer model of Gula & Zeitlin (2009). We presented the results of exhaustive linear stability analysis of, respectively, configurations with stable or unstable in the barotropic (reduced-gravity, one-layer) limit upper-layer current. The linear instabilities were identified and classified according to the character of resonating eigenmodes forming the unstable modes, and their dependence on the depth ratio of the layers was displayed. The fully nonlinear DNS using a novel high-resolution entropy-satisfying well-balanced finite-volume scheme of Bouchut & Zeitlin (2009), which copes with losses of hyperbolicity associated to Kelvin-Helmholtz instabilities in multi-layer systems, were performed to understand the nonlinear stage of instability.

The main conclusions following from these DNS are as follows. In the case of barotropically stable upper-layer flow, for deep, but not extremely deep lower layers the baroclinicity destabilizes the system via an instability due to the resonance between the lower-layer Rossby wave, and an upper-layer frontal wave propagating along the outcropping line (RF instablity). The growing RF instability leads to breaking of the Rossby and the frontal wave in respective layers, and formation of coherent vortices which are able to detach from the coast due to their dipolar structure in the lower layer. Kelvin front formation at the coast plays an important role in this process. For sufficiently shallow lower layers the short-wave Kelvin-Helmholtz type instabilities dominate the initial evolution of the flow. They are, however, rapidly smeared out by dissipation, and do not lead to substantial reorganization of the flow, which is then subject to the RF instability with similar, as described above, evolution.

In the case of barotropically unstable upper-layer flow, and sufficiently deep lower layers, the barotropic instability resulting from the resonance of the frontal and Kelvin waves in the upper layer (KF instability), dominates following the scenario of Gula & Zeitlin (2009). However, at the later stages of the evolution the baroclinic RF instability steps in and excites vortical structures in the lower layer. The whole system then undergoes baroclinic instability leading to coherent vortex structures appearing in both layers and eventually detaching from the coast. For shallower lower layers, again, the

Kelvin-Helmholtz instabilities dominate at initial stages, being eliminated then by dissipation. They do not much influence the development of the barotropic KF instability, and subsequent switching of slower RF baroclinic instability. This latter leads to the formation of coherent vortices with pronounced baroclinic structure.

Let us finally mention that linear stability analysis exposed in the present paper and in Part I may be performed in cylindrical geometry used in experimental studies (cf. Griffiths & Linden (1982)), as was done by Gula *et al.* (2009*c*) for non outcropping configurations, with the results similar to those presented above.

6.5 Conclusion

L'étude de stabilité linéaire et non-linéaire pour un courant côtier dans le modèle à deux couches a donc permis de généraliser les résultats du modèle en gravité réduite de la partie 6.2. Nous avons pu répertorier les différentes instabilités linéaire pour un courant côtier, les interpréter en termes de résonances entre les modes stables du système et étudier l'influence du rapport de hauteur entre les deux couches. Comme précédemment l'évolution non-linéaire de ces modes a été étudiée à l'aide du code numérique en volume fini présenté dans la partie 3.2.

Les résultats du modèle à gravité réduite sont logiquement retrouvés pour l'analyse linéaire et les simulations non-linéaires lorsque le rapport de hauteur est grand (typiquement $r = H_2/H_1 > 100$), puisque dans ce cas le couplage entre les deux couches est faible.

Ensuite, dans le cas où la couche supérieure est barotropiquement stable, pour des rapports de hauteur typiquement de l'ordre de l'unité, les interactions baroclines entre des modes de Rossby présents dans la couche inférieure et le mode frontal présent dans la couche supérieure déstabilisent l'écoulement. Cette instabilité se développe alors jusqu'au déferlement de l'onde de Rossby et du mode frontal qui vont former des vortex dans les deux couches avec une structure dipolaire dans la couche inférieure qui va permettre un détachement du vortex qui se propage alors vers le large. Lorsque le rapport de hauteur est suffisamment faible $r < 1$, une instabilité de Kelvin-Helmholtz de petite longueur d'onde se développe dans la zone frontale, mais cette instabilité est rapidement évacuée à cause de la dissipation sans provoquer de modification significative de l'écoulement moyen et l'écoulement retrouve alors l'évolution décrite précédemment.

Lorsque la couche supérieure est barotropiquement instable, pour des rapports de hauteur assez grands, on retrouve dans un premier temps le scénario étudié dans le cadre du modèle à gravité réduite avec le développement du mode instable correspondant à l'interaction dans la couche supérieure entre le mode de Kelvin et le mode frontal. Des structures vorticales apparaissent néanmoins dans la couche inférieure à des temps plus longs et permettent ensuite le développement d'une instabilité barocline et la formation de vortex qui vont finir par se détacher de la côte. Comme dans le cas précédent, pour des rapports de hauteur plus faibles l'instabilité de Kelvin-Helmholtz apparaît, sans modification notable du scénario ultérieur.

On peut noter qu'il est tout à fait possible de réaliser les analyses de stabilité linéaires précédentes avec une géométrie cylindrique correspondant à celle utilisée dans les expériences (cf. Griffiths & Linden (1982) et Bouruet-Aubertot & Linden (2002)), comme cela avait été fait dans la partie 4 dans le cadre de configurations sans outcropping.

Chapitre 7

Résumé et conclusions

'Au moins tu sais, toi, océan, - Qu'il est inutile - De rêver ta fin.'
Eugène Guillevic.

Nous nous sommes intéressés dans cette thèse aux mécanismes d'instabilité couplant des mouvements tourbillonnaires équilibrés avec des mouvements non-équilibrés (onde de gravité, onde de Kelvin). Nous avons examiné en particulier l'instabilité Rossby-Kelvin dans un fluide à deux couches dans un canal et dans un anneau, et les différentes interactions du mode frontal avec des modes vorticaux ou de gravité pour des courants côtiers. Des études de stabilité linéaire ont été réalisées avec la méthode de collocation pour les différentes configurations et des simulations non-linéaires dans le modèle de l'eau peu profonde avec une méthode numérique aux volumes finis et dans un fluide continument stratifié à l'aide d'un modèle méso-échelle.

Dans le modèle de l'eau peu profonde à deux couches dans un canal, dans le cas rectiligne et dans le cas cylindrique, les analyses de stabilité linéaire systématiques réalisées montrent l'importance du mode RK à nombre de Rossby fini. Lorsque ce dernier est très faible, l'écoulement n'est susceptible de développer que l'instabilité barocline classique, instabilité équilibrée, conformément aux intuitions quasi-géostrophiques. Mais certains régimes de paramètres peuvent donner lieu à une compétition entre l'instabilité barocline classique et l'instabilité RK, avec des taux de croissance comparables et même supérieurs pour l'instabilité RK. L'analyse linéaire ne suffit alors pas pour déterminer le comportement de l'écoulement dans ces régimes.

Il est important de se rappeler que l'appellation "Rossby-Kelvin" telle que définie par Sakai (1989) regroupe à la fois les interactions entre modes de Rossby et modes de Kelvin et les interactions entre modes de Rossby et modes de Poincaré. Les différentes analyses de stabilité montrent à cet égard que si le couplage de l'onde de Rossby avec le mode de Kelvin est pertinent dans les configurations étudiées, le couplage entre un mode de Rossby et un mode de Poincaré est par contre beaucoup moins efficace. Les taux de croissances des instabilités impliquant des modes de Poincaré sont systématiquement plus faibles que ceux des instabilités impliquant des modes de Kelvin, et leurs nombres d'ondes instables sont compris dans des intervalles significativement plus étroits. Ces nombres d'ondes sont d'ailleurs plus élevés, ce qui rend ces interactions d'autant plus susceptibles d'être "noyées" par l'instabilité Kelvin-Helmholtz, dont les taux de croissances sont notablement plus importants.

Le couplage entre modes vorticaux et modes de gravité est donc plus particulièrement efficace en présence d'un bord, du fait de la présence des ondes de Kelvin. Il a alors été naturel d'évoluer vers des configurations océaniques comme les courants côtiers. Nous avons montré que pour de telles configurations, l'écoulement pouvait devenir barotropiquement instable du fait de la résonance entre un mode de Kelvin se propageant le long du bord et d'un mode frontal (mode vortical) se propageant le long du front (instabilité KF). Ce mécanisme d'instabilité est par bien des égards analogue à l'instabilité RK. Les interactions entre le mode de Kelvin ou le mode frontal et les différents modes de Poincaré se propageant le long du bord ou de la côte sont aussi une possibilité. Les résultats des analyses linéaires montrent une fois encore que ces instabilités, contrairement à l'instabilité KF, possèdent des taux de croissance faibles et des intervalles de nombres d'onde instables très étroits qui les rendent vraisemblablement inaptes à jouer un rôle dans l'évolution de l'écoulement. C'est ce que confirment les simulations numériques effectuées dans le modèle de l'eau peu profonde, qui montrent que ces instabilités sont très rapidement dissipés dans tous les cas et ne sont alors pas capables de croître significativement ni de modifier notablement l'écoulement.

Les simulations non-linéaires dans le modèle de l'eau peu profonde montrent que les instabilités RK et KF ont un développement non-linéaire similaire et plus particulièrement un mécanisme de saturation qui influence de manière importante l'évolution de l'écoulement. Dans les deux cas, après la croissance exponentielle conforme à la théorie linéaire, ces instabilités atteignent une amplitude finie et saturent selon un scénario identique. C'est la partie "onde de Kelvin" qui guide cette saturation puisque celle-ci déferle et arrête ainsi la croissance du mode. Dans le cadre des simulations non-linéaires réalisées dans le modèle de l'eau peu profonde, ce déferlement est associé à une formation d'un front de Kelvin et à une zone de dissipation et de mélange intense et très localisée. Les effets du déferlement de l'onde de Kelvin sur l'écoulement se manifestent de deux façons : par émission d'ondes d'inertie-gravité, il introduit des mouvements non-équilibrés de (relativement) petite échelle. Et surtout, ce déferlement modifie l'écoulement moyen, ce qui se traduit principalement par un ralentissement de l'écoulement zonal le long de la côte sur laquelle se propageait l'onde de Kelvin, et l'apparition d'une anomalie de vorticité potentielle. La réorganisation de la distribution de vorticité potentielle, et la création de gradients de vorticité potentielle dans l'écoulement peut conduire au développement d'une nouvelle instabilité comme on a pu le voir dans le cas des courants côtiers.

Les résultats précédents sur l'instabilité RK ayant été obtenus dans le modèle de l'eau peu profonde à deux couches, la question de la persistance de ces instabilités dans la situation plus réaliste du fluide continument stratifié a été étudiée à l'aide du modèle méso-échelle WRF (Weather Research and Forecast). L'existence des modes d'instabilité RK dans des régions frontales d'un fluide continument stratifié a été montrée dans ces simulations idéalisées. Les taux de croissance et structures de ces modes sont très semblables à ceux obtenus dans le cas de l'eau peu profonde si ce n'est leur sensibilité importante à l'intensité des fronts. Le développement initial, mais aussi les différents aspects de la saturation de l'instabilité RK sont aussi relativement bien reproduits. Le déferlement de l'onde de Kelvin comporte néanmoins quelques différences étant donné la dynamique verticale du modèle. Celui-ci est caractérisée par l'apparition d'instabilités de petite échelle et de vitesses verticales intenses le long de bord. La réorganisation de l'écoulement moyen est quand à elle similaire à celle constatée dans le modèle de l'eau peu profonde.

Ces instabilités agéostrophiques procurent donc à nombre de Rossby fini un mécanisme par lequel les mouvements équilibrés vont transférer de l'énergie vers des mouvements non-équilibrés, générant de la dissipation et du mélange à petite échelle.

Annexe A

Compléments au chapitre 5

A.1 Toit rigide Vs surface libre

Comme on l'a vu lors de la dérivation des équations du modèle de l'eau peu profonde (partie 2.1), en considèrant une surface libre au lieu d'un toit rigide, les équations du modèle à 2 couches sur le plan f vont s'écrire :

$$\begin{aligned} \partial_t \mathbf{v}_i + \mathbf{v}_i \cdot \nabla \mathbf{v}_i + f \hat{\mathbf{z}} \wedge \mathbf{v}_i + \frac{1}{\bar{\rho}_i} \nabla(\bar{\rho}_1 g h_1 + \bar{\rho}_i g h_2) &= 0, \quad i = 1, 2 && \text{(A.1)} \\ \partial_t h_i + \nabla \cdot (h_i \mathbf{v}_i) &= 0, \quad i = 1, 2. && \text{(A.2)} \end{aligned}$$

où les indices 1 (2) désignent la couche supérieure (inférieure) respectivement. (x, y) et $\mathbf{v_j} = (u_j, v_j)$ sont les coordonnées et vitesses zonales et méridionales, $h_j(x, y, t)$ les hauteurs des couches, π_j, ρ_j les pressions et densités et f le paramètre de Coriolis.

On considère donc un modèle à 2 couches sur le plan f dans un canal de largeur y_L avec un cisaillement de vitesse vertical constant comme représenté sur la figure A.1. En linéarisant les équations autour de l'état de base défini par les vitesses constantes $U_1 = -U_2 = U_0$ et les hauteurs $H_j(y)$, où u_j, v_j et h_j sont les perturbations de cet état de base, on obtient :

$$\begin{aligned} \partial_t u_j + U_j \partial_x u_j - f v_j &= -g\, \partial_x (s^{j-1} h_1 + h_2)\ , \\ \partial_t v_j + U_j \partial_x v_j + f u_j &= -g\, \partial_y (s^{j-1} h_1 + h_2)\ , \\ \partial_t h_j + U_j \partial_x h_j + H_j \partial_x u_j &= -\partial_y (H_j v_j)\ , \end{aligned} \qquad \text{(A.2)}$$

avec $s = \rho_1/\rho_2$ le paramètre de stratification et $g' = (1 - s)g$ la gravité réduite.

Les taux de croissance et les vitesses de phase des différents modes ainsi obtenus sont représentés sur les figures A.2 et A.3.

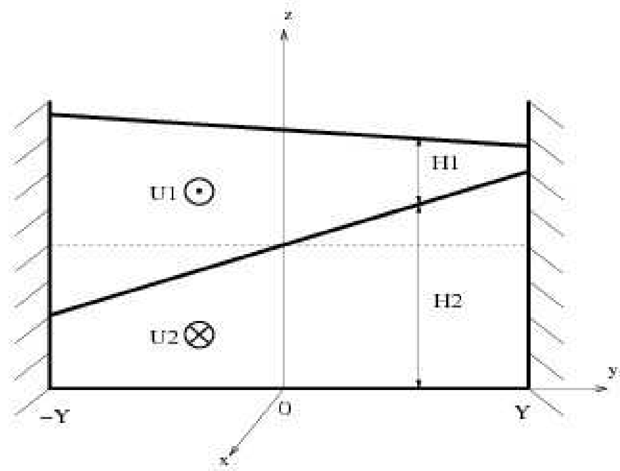

FIG. A.1 – Schéma du modèle

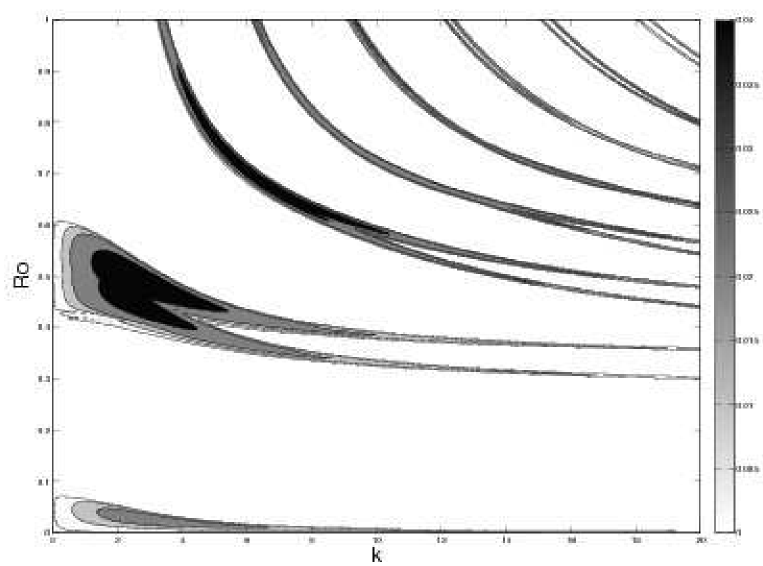

FIG. A.2 – Taux de croissance des instabilités représentés dans le plan (Ro, k). Les contours sont représentés à 0.01, 0.02 puis avec un intervalle de 0.02

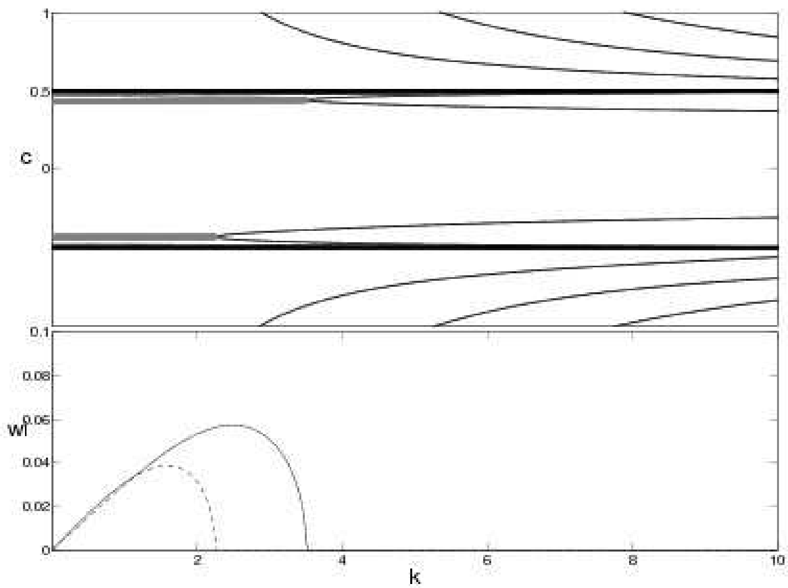

FIG. A.3 – Taux de croissance des instabilités selon la section $Ro = 0.5$. En haut la vitesse de phase et en bas le taux de croissance en fonction du nombre d'onde. Toutes les grandeurs sont adimensionnées

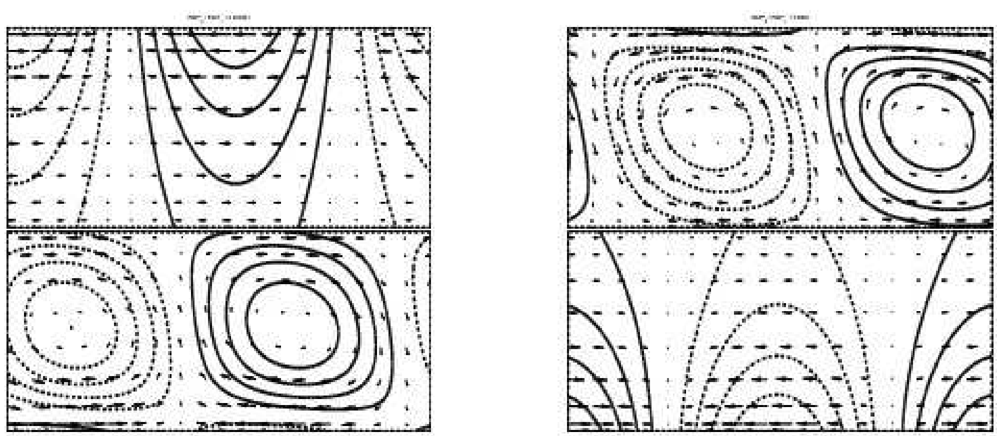

FIG. A.4 – Champ de pression et de vitesses dans chacune des 2 couches pour l'instabilité RK. A gauche pour $k = 1.5$ et $Ro = 0.5$ et à droite pour $k = 2.7$ et $Ro = 0.5$

A.2 Evolution non-linéaire du mode RK dans le modèle de l'eau peu profonde

Nous avons étudié dans le chapitre 5 le développement non-linéaire de l'instabilité RK pour des écoulements continument stratifiés à l'aide de simulations idéalisées effectuées avec le modèle météorologique méso-échelle WRF. Ces simulations nous ont permis de montrer la pertinence de ces modes dans une configuration plus réaliste ainsi que d'étudier certains aspects de leur croissance et saturation. Nous allons simplement montrer ici que les conclusions concernant le développement non-linéaire de ces instabilités sont comparables pour des simulations numériques dans le modèle de l'eau peu profonde.

L'évolution non-linéaire du mode RK est donc simulée à l'aide du code numérique en volume fini dans sa version deux couches. Les simulations étant initialisées avec les modes instables issus de l'analyse de stabilité linéaire présentée dans la partie A.1 pour un canal périodique en rotation avec une surface libre.

La figure A.5 montre l'évolution des champs de pression et de vitesse pour le mode instable représenté figure A.4, et la figure A.6 l'énergie cinétique de la perturbation pour cette même simulation.

La saturation du mode RK est tout à fait similaire à ce que l'on a pu voir pour la saturation de l'instabilité frontale d'un courant côtier dans les simulations numériques ddu chapitre 6. Elle est provoquée par le déferlement de l'onde de Kelvin se propageant le long de la côte, qui est caractérisé par l'apparition d'un front de Kelvin, d'une émission d'ondes d'inertie-gravité de petite échelle et une modification de l'écoulement moyen.

Cette évolution non-linéaire est aussi comparable avec celle obtenue pour les simulations idéalisées d'un flude continument stratifié effectuées avec le modèle WRF (chapitre 5). Quelques différences sont néanmoins notables dans le processus de saturation du mode en raison de la dynamique verticale plus développée dans le modèle WRF.

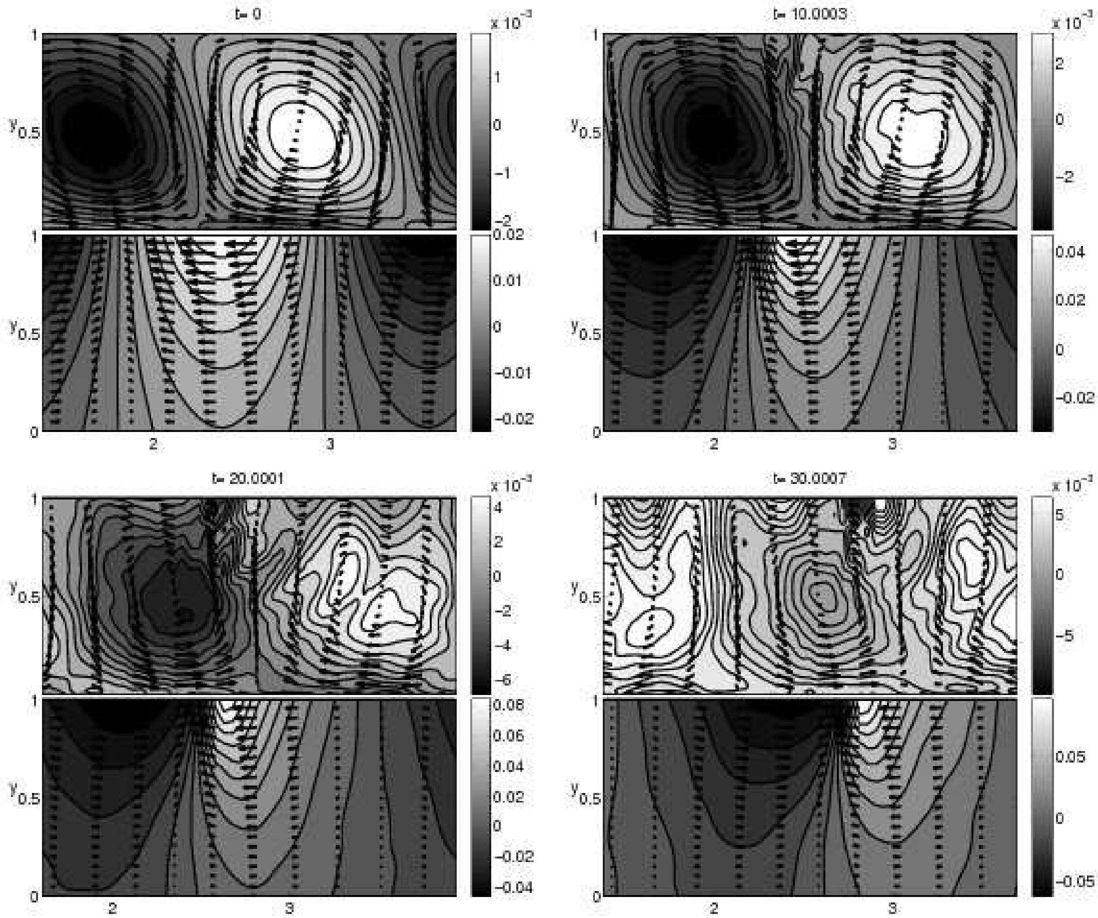

FIG. A.5 – Champs de vitesse et de pression dans la couche supérieure (haut de chaque panneau) et dans la couche inférieure (bas de chaque panneau) à $t = 0, 10, 20, 30$ de gauche à droite et de haut en bas.

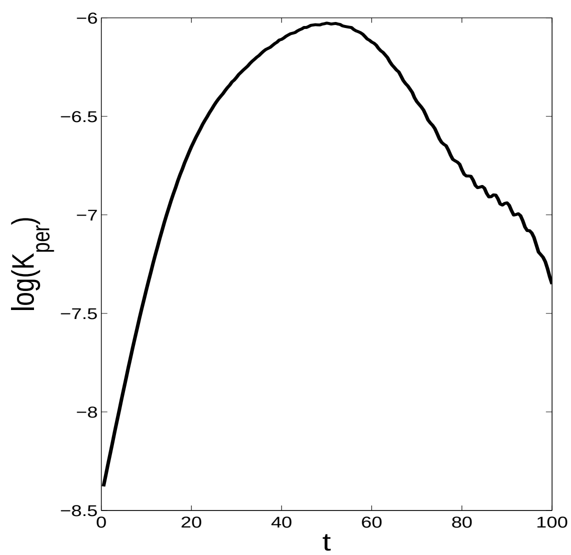

FIG. A.6 – Evolution de l'énergie cinétique de la perturbation (normalisée par l'énergie cinétique initiale totale) pour la simulation representée figure A.5

Bibliographie

AFANASYEV, Y. 2003 Spontaneous emission of gravity waves by interacting vortex dipoles in a stratified fluid : laboratory experiments. *Geophys. Astrophys. Fluid Dyn.* **97** (2), 79–95.

ANDREWS, D.G., HOLTON, J.R. & LEOVY, C.B. 1987 *Middle atmosphere dynamics*. Academic Press.

AUDUSSE, E., BOUCHUT, F., BRISTEAU, M.-O., KLEIN, R. & PERTHAME, B. 2004 A fast and stable well-balanced scheme with hydrostatic reconstruction for shallow water flows. *SIAM J. Sci. Comput.* **25**, 2050–2065.

AUSTIN, J. & COLLABORATORS 2003 Uncertainties and assessment of chemistry-climate models of the stratosphere. *Atm. Chem. Phys.* **3**, 1–27.

BALMFORTH, N.J. 1999 Shear instability in shallow water. *J. Fluid Mech.* **387**, 97–127.

BARTH, J.A. 1989*a* Stability of a coastal upwelling front, 1. model development and a stability theorem. *J. Geophys. Res.* **94**, 10844–10856.

BARTH, J.A. 1989*b* Stability of a coastal upwelling front, 2. model results and comparison with observations. *J. Geophys. Res.* **94**, 10857–10883.

BARTH, J.A. 1994 Short-wavelenght instabilities on coastal jets and fronts. *J. Geophys. Res.* **99**, 16095–16115.

BENJAMIN, T.B. 1963 Classification of unstable disturbances in flexible surfaces bounding inviscid flows. *J. Fluid Mech.* **16**, 436–450.

BENNETT, J.R. 1973 A theory of large-amplitude kelvin waves. *J. Phys. Oceanogr.* **3**, 57–60.

BLUMEN, W. 1972 Geostrophic adjustment. *Reviews of Geophysics and Space Physics* **10** (2), 485–528.

BOSS, E., PALDOR, N. & THOMPSON, L. 1996 Stability of a potential vorticity front : from quasi-geostrophy to shallow water. *J. Fluid Mech.* **315**, 65–84.

BOUCHUT, F. 2004 *Nonlinear stability of finite volume methods for hyperbolic conservation laws, and well-balanced schemes for sources*. Frontiers in Mathematics series, Birkhauser.

BOUCHUT, F. 2007 *Efficient numerical finite-volume schemes for shallow water models*, pp. 189 – 256. in "Nonlinear dynamics of rotating shallow water : Methods and advances" (ed. V. Zeitlin), Edited Series on Advances in Nonlinear Science and Complexity, Vol. 2.

BOUCHUT, F., LE SOMMER, J. & ZEITLIN, V. 2004 1D rotating shallow water : non-linear semi-geostrophic adjustment, slow manifold and nonlinear wave phenomena. Part 2. High-resolution numerical simulations. *J. Fluid Mech.* **514**, 35–63.

BOUCHUT, F., LE SOMMER, J. & ZEITLIN, V. 2005 Breaking of equatorial waves. *Chaos* **15**, 013503–1–013503–19.

BOUCHUT, F. & MORALES, T. 2008 An entropy satisfying scheme for two-layer shallow water equations with uncoupled treatment. *M2AN* **42**, 683–698.

BOUCHUT, F. & ZEITLIN, V. 2009 A robust well-balanced scheme for multi-layer shallow-water equations. *Discr. and Cont. Dyn. Sys.* **In Press**.

BOURUET-AUBERTOT, P. & LINDEN, P.F. 2002 The influence of the coast on the dynamics of upwelling fronts. Part I : laboratory experiments. *Dyn. Atmos. Ocean* **36**, 153–173.

BROWN, E., COLLING, A., PARK, D., PHILLIPS, J., ROTHERY, D. & WRIGHT, J. 2001 *Ocean circulation*. Open University.

CAIRNS, R.A. 1979 The role of negative energy waves in some instabilities of parallel flows. *J. Fluid Mech.* **92**, 1–14.

CAPET, X.J. & CARTON, X. J. 2004 Nonlinear regimes of baroclinic boundary currents. *J. Phys. Oceanogr.* **34**, 1400–1409.

CAPET, X.J., CHÉRUBIN, L. & MOREL, Y. 2002 Influence of the transport on the instability of a boundary current. *J. Phys. Oceanogr.* **32**, 2806–2815.

CHARNEY, J.G. 1947 The dynamics of long waves in a baroclinic westerly current. *J. Met.* **4**, 135–163.

CHIA, F., GRIFFITHS, W. & LINDEN, P.F. 1982 Observed interannual oscillations of planetary wave forcing in the Northern Hemisphere winter. *Geophys. Astrophys. Fluid Dyn.* **19**, 189–206.

CRAIK, A.D.D. & ADAM, J.A. 1979 'explosive' resonant wave interactions in a three-layer fluid flow. *J. Fluid Mech.* **92**, 15–33.

DAHL, O.H. 2005 Development of perturbations on a buoyant coastal current. *J. Fluid Mech.* **527**, 337–351.

DALIN, P., KIRKWOOD, S., MOSTROM, A., STEBEK, K., HOFFMANN, P. & SINGER, W. 2004 A case study of gravity waves in noctilucent clouds. *Ann. Geophys.* **22**, 1875–1884.

DRAZIN, P.G. & REID, W.H. 1981 *Hydrodynamic Stability*. Cambridge University Press.

DUDHIA, J. 1993 A nonhydrostatic version of the Penn State/NCAR mesoscale model : validation tests and simulation of an atlantic cyclone and cold front. *Mon. Weath. Rev.* **121**, 1493–1513.

DUNKERTON, T.J. 1997 The role of gravity waves in the quasi-biennial oscillation. *J. Geophys. Res.* **102**, 26053–26076.

DUNKERTON, T., LELONG, P. & C. SNYDER, EDS. 2008 Spontaneous imbalance. *J. Atmos. Sci.* **Special collection**, `http://ams.allenpress.com/perlserv/?request=get-collection&coll_id=20&ct=1`.

DURRAN, D.R. 1998 *Numerical methods for wave equations in geophysical fluid dynamics*. Number 32 in Texts in applied mathematics. Springer Verlag New York.

EADY, E.T. 1949 Long waves and cyclone waves. *Tellus* **1**, 33–52.

E.I., OLAFSDOTTIR, DAALHUIS, A.B. OLDE & VANNESTE, J. 2008 Inertia-gravity-wave generation by a sheared vortex. *J. Fluid Mech.* **569**, 169–189.

FEDOROV, A.V. & MELVILLE, W.K. 1995 Propagation and breaking of nonlinear Kelvin waves. *J. Phys. Oceanogr.* **25**, 2519–2531.

FEDOROV, A.V. & MELVILLE, W.K. 2000 Kelvin fronts on the equatorial thermocline. *J. Phys. Oceanogr.* **30**, 1692–1705.

FJØRTOFT, R. 1950 Application of integral theorems in deriving criteria of stability for laminar flows and for the baroclinic circular vortex. *Geophys. Publ.* **17**, 1–52.

FLOR, J.B. 2008 Frontal instability, inertia-gravity wave radiation and vortex formation. In *Proceedings of the ICMI International Conference on Multimodal Interfacings, London, U.K.*.

FORD, R. 1994 Gravity wave radiation from vortex trains in rotating shallow water. *J. Fluid Mech.* **281**, 81–118.

FORD, R., MCINTYRE, M. E. & NORTON, W. A. 2000 Balance and the slow quasi-manifold : some explicit results. *J. Atmos. Sci.* **57**, 1236–1254.

FRITTS, D.C. & ALEXANDER, M.J. 2003 Gravity wave dynamics and effects in the middle atmosphere. *Reviews of Geophysics* **41** (1), 1003.

FRITTS, D.C. & NASTROM, G.D. 1992 Sources of mesoscale variability of gravity waves. Part II : Frontal, convective, and jet stream excitation. *J. Atmos. Sci.* **49** (2), 111–127.

FUKAMACHI, Y., JR., J.P. MCCREARY & PROEHL, J.A. 1995 Instability of density fronts in layer and continuously stratified models. *J. Geophys. Res.* **100**, 2559–2577.

FULTZ, D., LONG, R.R., OWENS, G.V., BOHAN, W., KAYLOR, R. & WEIL, I. 1959 Studies of thermal convection in a rotating cylinder with some implications for large-scale atmospheric motions. *Met. Monograph* **4**, 1–104.

GRIFFITHS, R.W., KILLWORTH, P.D. & STERN, M.E. 1982 Ageostrophic instability of ocean currents. *J. Fluid Mech.* **117**, 343 – 377.

GRIFFITHS, R. W. & LINDEN, P. F. 1981 The stability of buoyancy-driven coastal currents. *Dyn. Atmos. Ocean* **5**, 281–306.

GRIFFITHS, R. W. & LINDEN, P. F. 1982 Part I : density-driven boundary currents. *Geophys. Astrophys. Fluid Dyn.* **19**, 159–187.

GUEST, F., REEDER, M., MARKS, C. & KAROLY, D. 2000 Inertia-gravity waves observed in the lower stratosphere over Macquarie Island. *J. Atmos. Sci.* **57**, 737–752.

Gula, J., Plougonven, R. & Zeitlin, V. 2009*a* Ageostrophic instabilities of fronts in a channel in the stratified rotating fluid. *J. Fluid Mech.* **627**, 485–507.

Gula, J. & Zeitlin, V. 2009 Instabilities of buoyancy driven coastal currents and their nonlinear evolution in the two-layer rotating shallow water model. part I. Passive lower layer. *submitted to J. Fluid Mech.* .

Gula, J., Zeitlin, V. & Bouchut, F. 2009*b* Instabilities of buoyancy driven coastal currents and their nonlinear evolution in the two-layer rotating shallow water model. part II. Active lower layer. *submitted to J. Fluid Mech.* .

Gula, J., Zeitlin, V. & Plougonven, R. 2009*c* Instabilities of two-layer shallow-water flows with vertical shear in the rotating annulus. *J. Fluid Mech.* **638**, 27–47.

Hart, J. E. 1972 A laboratory study of baroclinic instability. *Geophys. Astrophys. Fluid Dyn.* **3**, 181–209.

Hart, J. E. & Kittelman, S. 1986 A method for measuring interfacial wave fields in the laboratory. *Geophys. Astrophys. Fluid Dyn.* **336**, 179–185.

Hayashi, Y.-Y. & Young, W.R. 1987 Stable and unstable shear modes of rotating parallel flows in shallow water. *J. Fluid Mech.* **184**, 477 – 504.

Haza, A.C., Paldor, N. & Mariano, A.J. 2004 Linear isntabilities of a two-layer geostrophic surface front near a wall. *jmr* **62**, 639–662.

Helmholtz, L.F. 1868 On the discontinuous movements of fluids. *Monthly Reports of the Royal Prussian Academy of Philosophy in Berlin* **23**, 215.

Hide, R. 1958 An experimental study of thermal convection in a rotating liquid. *Philosophical Transactions of the Royal Society of London. Series A, Mathematical and Physical Sciences* **250** (983), 441–478.

Hide, R. & Fowlis, W.W. 1965 Thermal convection in a rotating annulus of liquid : effect of viscosity on the transition between axisymmetric and non-axisymmetric flow regimes. *J. Atmos. Sci.* **22**, 541–558.

Holmboe, J. 1962 On the behaviour of symmetric waves in stratified shear flows. *Geophys. Publ.* **24**, 67.

Holton, J.R., Haynes, P.H., McIntyre, M.E., Douglass, A.R., Rood, R.B. & Pfister, L. 1995 Stratosphere-troposphere exchange. *Reviews of Geophysics* **4** (403-409).

Holton, J. R. 1992 *An introduction to dynamic meteorology*, 3rd edn. Academic Press.

Hoskins, B.J., McIntyre, M.E. & Robertson, A.W. 1985 On the use and significance of isentropic potential vorticity maps. *Q.J.R. Meteorol. Soc.* **111** (470), 877–946.

Iga, K. 1993 Reconsideration of Orlanski's instability theory of frontal waves. *J. Fluid Mech.* **255**, 213–236.

Iga, K. 1995 Transition modes of rotating shallow water waves in a channel. *J. Fluid Mech.* **294**, 367–390.

IGA, K. 1997 Instability of a front with a layer of uniform potential vorticity. *J. Met. Soc. Japan* **75**, 1–11.

IGA, K. 1999 Critical layer instability as a resonance between a non-singular mode and continuous modes. *Fluid Dyn. Res.* **25**, 63–86.

IGA, K. & IKAZAKI, H. 2000 Instability of a front formed by two layers with uniform potential vorticity. *J. Met. Soc. Japan* **78**, 491–498.

IKEDA, M. 1983 Linear instability of a current flowing along a bottom slope using a three-layer model. *J. Phys. Oceanogr.* **13**, 208–223.

JAMES, I.N. 1977 Stability of flow in a slowly rotating two-layer system. *Occasional Note Met O 27/77/2* .

JEFFREYS, H. 1925 On the dynamics of geostrophic winds. *Q.J.R. Meteorol. Soc.* **52**, 85–104.

JONES, W.L. 1967 Propagation of internal gravity waves in fluids with shear flow and rotation. *J. Fluid Mech.* **30**, 439–448.

KELVIN 1871 Hydrokinetic solutions and observations. *Phil. Mag.* **42**, 362–377.

KILLWORTH, P.D. 1983*a* Long-wave instability of an isolated front. *Geophys. Astrophys. Fluid Dyn.* **25**, 235–258.

KILLWORTH, P.D. 1983*b* On the motion of isolated lenses on a beta-plane. *J. Phys. Oceanogr.* **13**, 368–376.

KILLWORTH, P.D., PALDOR, N. & STERN, M.E. 1984 Wave propagation and growth on a surface front in a two-layer geostrophic current. *J. Mar. Res.* **42**, 761–785.

KILLWORTH, P.D. & STERN, M.E. 1982 Instabilities on density-driven boundary currents and fronts. *Geophys. Astrophys. Fluid Dyn.* **22**, 1–28.

KIM, Y.-J., ECKERMANN, S.D. & CHUN, H.-Y. 2003 An overview of the past, present and future of gravity-wave drag parametrization for numerical climate and weather prediction models. *Atmosphere-Ocean* **41**, 65–98.

KNESSL, C. & KELLER, J.B. 1995 Stability of linear shear flows in shallow water. *J. Fluid Mech.* **303**, 203–214.

KNOX, J.A., MCCANN, D & WILLIAMS, P.D. 2009 Reply to comments on 'application of the Lighthill-Ford theory of spontaneous imbalance to clear-air turbulence forecasting'. *J. Atmos. Sci.* .

KUBOKAWA, A. 1985 Instability of a geostrophic front and its energetics. *Geophys. Astrophys. Fluid Dyn.* **33**, 223–257.

KUBOKAWA, A. 1986 Instability caused by the coalescence of two modes of a one-layer coastal current with a surface front. *J. Oceanograph. Soc. Japan* **42**, 373–380.

KUBOKAWA, A. 1988 Instability and nonlinear evolution of a desity-driven coastal current with a surface front in a two-layer ocean. *Geophys. Astrophys. Fluid Dyn.* **40**, 195–223.

Kubokawa, A. & Hanawa, K. 1984 A theory of semigeostrophic gravity waves and its application to the intrusion of a density current along a coast. part 1. *J. Oceanograph. Soc. Japan* **40**, 247–259.

Kuo, H.L. 1949 Dynamic instability of two-dimensional non-divergent flow in a barotropic atmosphere. *J. Met.* **6**, 105–122.

Leblond, P.H. & Mysak, L.A. 1978 *Waves in the ocean*. Elsevier.

Lee, S.K. & Csanady, G.T. 1994 Instability waves in the gulf stream front and its thermocline layer. *J. Mar. Res.* **52**, 837–863.

Leith, C.E. 1980 Nonlinear normal mode initialization and quasi-geostrophic theory. *J. Atmos. Sci.* **37**, 958–968.

LeSommer, J., Medvedev, S., Plougonven, R. & Zeitlin, V. 2003 Singularity formation during relaxation of jets and fronts towards the state of geostrophic equilibrium. *Communications in Nonlinear Science and Numerical Simulations* **8**, 415–442.

LeSommer, J., Reznik, G. & Zeitlin, V. 2004 Nonlinear geostrophic adjustment of long-wave disturbances in the shallow-water model on the equatorial beta-plane. *J. Fluid Mech.* **515**, 135–170.

Leveque, R.J. 2002 *Finite volume methods for hyperbolic problems*. Cambridge University Press.

Lighthill, J.M. 1952 On sound generated aerodynamically. *Proc. Roy. Soc. London* **211 (A)**, 564–587.

Lin, C. C. 1945 On the stability of two-dimensional parallel flows Part. II. *Quart. Appl. Math.* **3**, 218–234.

Lorenz, E.N. 1980 Attractor sets and quasi-geostrophic equilibrium. *J. Atmos. Sci.* **37**, 1685–1699.

Lott, F., Plougonven, R. & Vanneste, J. 2009 Gravity waves generated by sheared potential-vorticity anomalies. *J. Atmos. Sci.* .

Lovegrove, A.F., Read, P.L. & Richards, C.J. 2000 Generation of inertia-gravity waves in a baroclinically unstable fluid. *Q.J.R. Meteorol. Soc.* **126**, 3233–3254.

Marinone, S.G. & Ripa, P. 1984 Energetics and instability of a depth independant Equatorial jet. *Geophys. Astrophys. Fluid Dyn.* **30**, 105–130.

Martin, A. & Lott, F. 1986 Critical levels in shear flows. *Annu. Rev. Fluid Mech.* **18**, 405–432.

McCreary, J.P., Fukamachi, Y. & Kundu, P.K. 1991 A numerical investigation of jets and eddies near an eastern ocean boundary. *J. Geophys. Res.* **96**, 2515–2534.

Meacham, S.P. & Stephens, J.C. 2001 Instabilities of gravity currents along a slope. *J. Phys. Oceanogr.* **31**, 30–53.

Mohebalhojeh, A.R. & Dritschel, D.G. 2001 Hierarchies of balance conditions for the f-plane shallow-water equations. *J. Atmos. Sci.* **58**, 2411–2426.

Molemaker, M.J., McWilliams, J.C. & Yavneh, I. 2005 Baroclinic instability and loss of balance. *J. Phys. Oceanogr.* **35**, 1505–1517.

Nakamura, N. 1988 Scale slection of baroclinic instability - effects of stratification and nongeostrophy. *J. Atmos. Sci.* **45** (21), 3253–3267.

Obukhov, A.M. 1949 On the question of geostrophic wind (in Russian). *Izv. Akad. Nauk. SSSR Ser. Geografs.-Geofiz.* **13** (4), 281–306.

Orlanski, I. 1968 Instability of frontal waves. *J. Atmos. Sci.* **25**, 178–200.

Ortiz, S., Chomaz, J-M. & Loiseleux, T. 2002 Spatial holmboe waves. *Phys. Fluids* **14** (8), 2585–22597.

O'Sullivan, D. & Dunkerton, T.J. 1995 Generation of inertia-gravity waves in a simulated life cycle of baroclinic instability. *J. Atmos. Sci.* **52** (21), 3695–3716.

Paldor, N. 1983 Stability and stable modes of coastal fronts. *Geophys. Astrophys. Fluid Dyn.* **27**, 217–228.

Paldor, N. 1988 Amplitude-wavelenght relations of nonlinear frontal waves on coastal currents. *J. Phys. Oceanogr.* **18**, 753–760.

Paldor, N. & Ghil, M. 1990 Finite-wavelenght instabilities of a coupled density front. *J. Phys. Oceanogr.* **20**, 114–123.

Paldor, N. & Ghil, M. 1991 Shortwave instabilities of coastal currents. *Geophys. Astrophys. Fluid Dyn.* **58**, 225–241.

Paldor, N. & Killworth, P.D. 1987 Instabilities of a two-layer coupled front. *Deep-Sea Res.* **34**, 1525–1539.

Parker, D.J. 1998 Secondary frontal waves in the North Atlantic region : a dynamical perspective of current ideas. *Q.J.R. Meteorol. Soc.* **124**, 829–856.

Pedlosky, Joseph 1987 *Geophysical Fluid Dynamics*, 2nd edn. Springer-Verlag.

Perkins, J. & Renardy, M. 1997 Stability of equatorial currents with nonzero potential vorticity. *Geophys. Astrophys. Fluid Dyn.* **85** (31-64).

Phillips, N.A. 1954 Energy transformations and meridional circulations associated with simple baroclinic waves in a two-level, quasi-geostrophic model. *Tellus* **6** (6), 273–286.

Pierce, R.B. & Fairlie, T.D.A. 1993 Chaotic advection in the stratosphere : implications for the dispersal of chemically perturbed air from the polar vortex. *J. Geophys. Res.* **98** (D10), 18,589–18,595.

Plougonven, R., Muraki, D.J. & Snyder, C. 2005 A baroclinic instability that couples balanced motions and gravity waves. *J. Atmos. Sci.* **62**, 1545–1559.

Plougonven, R., Muraki, D.J. & Snyder, C. 2006 Erratum regarding 'a baroclinic instability that couples balanced motions and gravity waves'. *J. Atmos. Sci.* **63**, 1672–1673.

Plougonven, R. & Snyder, C. 2005 Gravity waves excited by jets : propagation versus generation. *Geoph. Res. Lett.* **32** (L18892), doi :10.1029/2005GL023730.

Plougonven, R. & Snyder, C. 2007 Inertia-gravity waves spontaneously generated by jets and fronts. Part I : Different baroclinic life cycles. *J. Atmos. Sci.* **64**, 2502–2520.

Plougonven, R., Snyder, C. & Zhang, F. 2009 Comments on 'application of the Lighthill-Ford theory of spontaneous imbalance to clear-air turbulence forecasting'. *J. Atmos. Sci.* **66**, 350–354.

Plougonven, R., Teitelbaum, H. & Zeitlin, V. 2003 Inertia-gravity wave generation by the tropospheric mid-latitude jet as given by the fastex radiosoundings. *J. Geophys. Res.* **108** (D21), 4686.

Plougonven, R. & Zeitlin, V. 2002 Internal gravity wave emission from a pancake vortex : an example of wave-vortex interaction in strongly stratified flows. *Phys. of Fluids* **14** (3), 1259–1268.

Poulin, F.J. & Flierl, G.R. 2003 The nonlinear evolution of barotropically unstable jets. *J. Phys. Oceanogr.* **33**, 2173–2192.

Pratt, L.J., Helfrich, K. & Leen, D. 2008 On the stability of ocean overflows. *J. Fluid Mech.* **602**, 241–266.

Rayleigh, Lord 1880 On the stability, or instability of certain fluid motions. *Proc. R. Soc. Lond.* **9**, 57–70.

Read, P.L. 1992 Applications of singular systems analysis to 'baroclinic chaos'. *Physica D* **58**, 455–468.

Reznik, G.M., Zeitlin, V. & Ben Jelloul, M. 2001 Nonlinear theory of geostrophic adjustment. Part 1. Rotating shallow-water model. *J. Fluid Mech.* **445**, 93–120.

Richter, J. H., Sassi, F., Garcia, R. R., Matthes, K. & Fischer, C. A. 2008 Lateral mixing in the equatorial pacific : The importance of inertial instability. *J. Geophys. Res.* **113**, D08101, doi :10.1029/2007JD009269.

Ripa, P. 1983 General stability conditions for zonal flows in a one-layer model on the β-plane or the sphere. *J. Fluid Mech.* **126**, 463 – 489.

Ripa, P. 1991 General stability conditions for a multi-layer model. *J. Fluid Mech.* **222**, 119 – 137.

Rossby, C.G. 1938 On the mutual adjustment of pressure and velocity distributions in certain simple current systems II. *J. Mar. Res.* **1**, 239–263.

Sakai, S. 1989 Rossby-Kelvin instability : a new type of ageostrophic instability caused by a resonance between Rossby waves and gravity waves. *J. Fluid Mech.* **202**, 149–176.

Satomura, T. 1981 An investigation of shear instability in a shallow water. *J. Met. Soc. Japan* **59**, 148–167.

Scherer, E. 2008 Ajustement géostrophique nonlinéaire en présence de guides d'ondes équatorial, côtier, topographique et frontal. PhD thesis, Université Pierre et Marie Curie.

Scherer, E. & Zeitlin, V. 2008 Instability of coupled geostrophic density fronts and its nonlinear evolution. *J. Fluid Mech.* **613**, 309–327.

Shi, X.B. & Roed, L.P. 1999 Frontal instabilities in a two-layer, primitive equation ocean model. *J. Phys. Oceanogr.* **129**, 948–968.

Skamarock, W.C., Klemp, J.B., Dudhia, J., Gill, D.O., Barker, D.M., Wang, W. & Powers, J. G. 2005 A description of the Advanced Research WRF Version 2. *NCAR Technical Note* .

Smeed, D.A. 1988*a* Baroclinic instability of three-layer flows, part 1., linear stability. *J. Fluid Mech.* **194**, 217–231.

Smeed, D.A. 1988*b* Baroclinic instability of three-layer flows, part 2., experiments with eddies. *J. Fluid Mech.* **194**, 233–259.

Stern, M.E. 1980 Geostrophic fronts, bores, breaking and blocking waves. *J. Fluid Mech.* **99**, 687–703.

Stern, M.E. & Simeonov, J.A. 2008 Frontal waves in a strait. *J. Fluid Mech.* **598**, 321–334.

Stewartson, K. 1957 On almost rigid rotations. *J. Fluid Mech.* **3**, 17–26.

Stewartson, K. 1981 Marginally stable inviscid flows with critical layers. *IMA J. Appl. Maths* **27**, 133–175.

Stone, P.H. 1966 On non-geostrophic baroclinic instability. *J. Atmos. Sci.* **23**, 390–400.

Stone, P.H. 1970 On non-geostrophic baroclinic instability : Part II. *J. Atmos. Sci.* **27**, 721–726.

Sutyrin, G.G. 2007 Ageostrophic instabilities in a horizontally uniform baroclinic flow along a slope. *J. Fluid Mech.* **588**, 463–473.

Takehiro, S.I. & Hayashi, Y.Y. 1992 Over-reflection and shear instability in a shallow-water model. *J. Fluid Mech.* **236**, 259–279.

Taylor, G.I. 1915 Eddy motion in the atmosphere. *Phil. Trans. R. Soc. Lond.* **A215**, 1–26.

Thorpe, S.A. 2005 *The turbulent ocean*. Cambridge University Press.

Tokioka, T. 1970 Non-geostrophic and non-hydrostatic stability of a baroclinic fluid. *J. Meteorol. Soc. Japan* **48**, 503–520.

Trefethen, L.N. 2000 *Spectral Methods in Matlab*. Philadelphia : Society for Industrial and Applied Mathematics.

Vadas, S.L. & Fritts, D.C. 2001 Gravity wave radiation and mean responses to local body forces in the atmosphere. *J. Atmos. Sci.* **58** (16), 2249–2279.

Vallis, G.K. 1992 Mechanisms and parameterization of geostrophic adjustment and a variational approach to balanced flow. *J. Atmos. Sci.* **49**, 1144–1160.

VALLIS, G.K. 1996 Potential vorticity inversion and balanced equations of motion for rotating and stratified flows. *Q.J.R. Meteorol. Soc.* **122**, 291–322.

VANNESTE, J. 1993 The Kelvin-Helmoltz instability in a non-geostrophic baroclinic unstable flow. *Mathl. Comput. Modelling* **17**, 149–154.

VANNESTE, J. 1998 A nonlinear critical layer generated by the interaction of free Rossby waves. *J. Fluid Mech.* **371**, 319–344.

VANNESTE, J. 2004 Inertia-gravity wave generation by balanced motion : revisiting the Lorenz-Krishnamurty model. *J. Atmos. Sci.* **61**, 224–234.

VANNESTE, J. & YAVNEH, I. 2004 Exponentially small inertia-gravity waves and the breakdown of quasi-geostrophic balance. *J. Atmos. Sci.* **61**, 211–223.

VANNESTE, J. & YAVNEH, I. 2007 Unbalanced instabilities of rapidly rotating stratified shear flows. *J. Fluid Mech.* **584**, 373–396.

VIÙDEZ, A. & DRITSCHEL, D.G. 2006 Spontaneous generation of inertia-gravity wave packets by balanced geophysical flows. *J. Fluid Mech.* **553**, 107–117.

WARN, T., BOKHOVE, O., SHEPHERD, T.G. & VALLIS, G.K. 1995 Rossby number expansions, slaving principles, and balance dynamics. *Q.J.R. Meteorol. Soc.* **121**, 723–739.

WARN, T. & MENARD, R. 1986 Nonlinear balance and gravity-inertial wave saturation in a simple atmospheric model. *Tellus* **38A**, 285–294.

WICKER, L.J. & SKAMAROCK, W.C. 2002 Time splitting methods for elastic models using forward time schemes. *Mon. Weath. Rev.* **130**, 2088–2097.

WILLIAMS, P.D. 2003 Nonlinear interactions of fast and slow modes in rotating, stratified fluid flows. PhD thesis, University of Oxford.

WILLIAMS, P.D., HAINE, T.W.N. & READ, P.L. 2005 On the generation mechanisms of short-scale unbalanced modes in rotating two-layer flows with vertical shear. *J. Fluid Mech.* **528**, 1–22.

WILLIAMS, P.D., HAINE, T.W.N. & READ, P.L. 2008 Inertia-gravity waves emitted from balanced flows : Observations, properties, and consequences. *J. Atmos. Sci.* **65**, 3543–3556.

WILLIAMS, P.D., READ, P.L. & HAINE, T.W.N. 2004 A calibrated, non-invasive method for measuring the internal interface height field at high resolution in the rotating, two-layer annulus. *Geophys. Astrophys. Fluid Dyn.* **98**, 453–471.

WIROSOETISNO, D., SHEPHERD, T.G. & TEMAM, R.M. 2002 Free gravity waves and balanced dynamics. *J. Atmos. Sci.* **59**, 3382–3398.

WUNSCH, C. & FERRARI, R. 2004 Vertical mixing energy and the general circulation of the oceans. *Annu. Review Fluid Mech.* **36**, 281–314.

YAVNEH, I. & MCWILLIAMS, J.C. 1994 Breakdown of the slow manifold in the shallow-water equations. *Geophys. Astrophys. Fluid Dyn.* **75**, 131–161.

YOUNG, W.R. & CHEN, L. 1995 Baroclinic instability and thermohaline gradient alignment in the mixed layer. *J. Phys. Oceanogr.* **25**, 3172–3185.

ZEITLIN, V. 2007 *Nonlinear dynamics of rotating shallow water : Methods and advances*. Edited Series on Advances in Nonlinear Science and Complexity, Elsevier.

ZEITLIN, V., REZNIK, G.M. & JELLOUL, M. BEN 2003 Nonlinear theory of geostrophic adjustment. Part 2 : Two-layer and continuously stratified primitive equations. *J. Fluid Mech.* **491** (10.1017/S0022112003005457), 207–228.

ZHANG, F., KOCH, S.E., DAVIS, C.A. & KAPLAN, M.L. 2001 Wavelet analysis and the governing dynamics of a large amplitude mesoscale gravity wave event along the east coast of the united states. *Q.J.R. Meteorol. Soc.* **127**, 2209–2245.